NUCLEAR STRUCTURE AND ORIENTATION EFFECTS IN THE DECAY OF HOT AND ROTATING COMPOUND NUCLEI

A THESIS
Submitted to the
FACULTY OF SCIENCE
PANJAB UNIVERSITY, CHANDIGARH
for the degree of

DOCTOR OF PHILOSOPHY

2016

Arshdeep Kaur

CENTRE OF ADVANCED STUDY IN PHYSICS
DEPARTMENT OF PHYSICS, PANJAB UNIVERSITY
CHANDIGARH-160014
(INDIA)

Acknowledgments

After the completion of thesis, as I look back, all those people come to my mind who stood by me during these years and offered their helping hand and guidance throughout this research work. A big "thank you" to all.

First and foremost , I would express my sincere gratitude and heartiest appreciation to my Ph.D. Thesis supervisor, Emeritus Professor Dr. Raj K. Gupta. I feel very fortunate for being associated to a supervisor who, with his vast research experience, is a constant oasis of ideas and his passion for scientific research is always an inspiration for me to grow as a researcher and as a person too. Thank you Sir for the guidance and patience. I cannot forget to Thank Madam Mrs. Shashi Prabha Gupta for her motherly affection, care and the delicious cakes occasionally.

Also, I express my gratitude to Professor Dr. Bivash R. Behera, the Thesis co-supervisor, for his support and guidance.

My big thanks and gratitude goes to Dr. Vishwamittar for being unfailingly patient and supportive throughout. I am also grateful to Dr. Neelam Malhotra for her motherly affection, love and care. This thesis would not have been possible without your support and guidance. Thank you Vishwamittar Sir and Neelam Ma'm.

I am also thankful to the Chairperson, Dept. of Physics, Panjab University, Chandigarh for providing all the departmental facilities for research.

My parents, S. Sarabjit Singh Gill and Smt. Jagjeet Kaur Gill have been the most indispensable source of strength for me. Thank you both for your blessings and encouraging me and providing me strong and unfailing support. Gratitude and regard is recorded for the affection, inspiration and cheerful encouragement offered by my father-in-law, S. Sukhdev Singh Sidhu and mother-in-law Smt. Sukhdeep Kaur Sidhu. Thank you both moms and dads, I love you all. I am also thankful to my brother Gagandeep Singh Gill and Bhabhi Navjot Kaur for their love, support and patience.

I am thankful for the fruitful discussions, encouragement and co-operation extended by my colleagues Ms. Sahila, Ms. Hemdeep, Dr. Gudveen and Dr. Niyti during this work.

They say "Good friends are hard to find, harder to leave and impossible to forget". I feel really lucky to have Taniya (Selfie), Raman, GurSimrat, Depinder, Anny, Gurvir, Chery, Veerpal, Khushboo and Galaxy as my friends. You people have helped me in all situations and made me stay normal during my tough times. Thank you all.

A special note of admiration and gratitude for my better half Sukhninder Singh Sidhu. Your co-operation, love and understanding paved the way to achieve this academic goal. I feel really blessed to have you as my life partner.

The chain of gratitude would definitely be incomplete without thanking the Almighty for inspiring and guiding me to complete this task.

Place: Chandigarh (Arshdeep Kaur)

Date: .....

List of Publications

I. International Journals:

1. Relative population of ^{6}Be and ^{8}Be clusters in the decay of excited compound nucleus ^{124}Ce* using the Dynamical Cluster-decay Model,
Arshdeep Kaur, Sahila Chopra, and Raj K. Gupta,
Acta Physica Polonica B **45**, 349 (2014).

2. α-cluster versus non-α-cluster decay of the excited compound nucleus ^{124}Ce* using the dynamical cluster-decay model,
Arshdeep Kaur, Sahila Chopra, and Raj K. Gupta,
Phys. Rev. C **89**, 034602 (2014).

3. Compound nucleus formation probability P_{CN} determined within the dynamical cluster-decay model for various "hot" fusion reactions,
Arshdeep Kaur, Sahila Chopra, and Raj K. Gupta,
Phys. Rev. C **90**, 024619 (2014).

4. Noncompound nucleus decay contribution in ^{12}C+^{93}Nb reaction using various formulations of nuclear proximity potential,
Sahila Chopra, **Arshdeep Kaur**, and Raj K. Gupta,
Phys. Rev. C **91**, 014602 (2015).

5. Determination of the compound nucleus survival probability P_{surv} for various "hot" fusion reactions based on the dynamical cluster-decay model,
Sahila Chopra, **Arshdeep Kaur**, and Raj K. Gupta,
Phys. Rev. C **91**, 034613 (2015).

6. α vs. non-α cluster decays of excited compound nucleus ^{124}Ce* using various formulations of nuclear proximity potential,
Arshdeep Kaur, Sahila Chopra, and Raj K. Gupta,
Phys. Rev. C **91**, 064601 (2015).

7. Non-coplanar compact configurations of nuclei and noncompound-nucleus decay content in the ^{12}C+^{93}Nb reaction,
Sahila Chopra, Hemdeep, **Arshdeep Kaur**, and Raj K. Gupta,
Phys. Rev. C **93**, 024603 (2016).

8. Product $P_{CN}P_{surv}$ or the "reduced" evaporation residue cross section $\sigma_{ER}/\sigma_{fusion}$ for "hot" fusion reactions studied on the dynamical cluster-decay model,
Sahila Chopra, **Arshdeep Kaur**, Hemdeep, and Raj K. Gupta,
Phys. Rev. C **93**, 044604 (2016).

9. Non-compound nucleus effects in measured decay channels of ^{217}At* formed in neutron-rich exotic ^{9}Li+^{208}Pb reaction and its synthesis within the dynamical cluster-decay model,

Arshdeep Kaur, Bivash R. Behera, and Raj K. Gupta,
(Chandigarh Preprints (2016), to be published).

II. In Conferences, Symposiums and Workshops etc. :

1. Alpha-nucleus vs. exotic clusters in the decay of excited compound nucleus $^{124}Ce^*$ formed in $^{32}S+^{92}Mo$ reaction,
Arshdeep Kaur, Sahila Chopra, and Raj K. Gupta,
DAE-BRNS Symp. on Nucl. Phys., **58**, 390 (2013); BARC, Mumbai, India, Dec 2-6, 2013.

2. Importance of Nuclear Structure Effects in Decay of Stable and Excited Nuclei,
Arshdeep Kaur, Sahila Chopra, and Raj K. Gupta,
National Conference on Emerging Horizons in Science and Technology, January 17-18, 2014, Sri Guru Granth Sahib World University, Fatehgarh Sahib.

3. Variation of compound nucleus fusion probability with its excitation energy in the Dynamical cluster-decay model,
Arshdeep Kaur, Sahila Chopra, and Raj K. Gupta,
8^{th} Chandigarh Science Congress, CHASCON-2014, February 26-28, 2014, Panjab University, Chandigarh.

4. Compound nucleus survival probability P_{surv} defined within the dynamical cluster-decay model,
Arshdeep Kaur, Sahila Chopra, and Raj K. Gupta,
75- years of Nuclear Fission: Present status and Future Perspectives. May 8-10, 2014, BARC Mumbai.

5. Non-compound nucleus component in decay of $^{12}C+^{93}Nb\rightarrow^{105}Ag^*$ reaction with non-coplanar degree of freedom included in dynamical cluster-decay model,
Sahila Chopra, **Arshdeep Kaur**, and Raj K. Gupta,
Book of Abstract, Zakopane Conference on Nuclear Physics, Poland, August 31-September 7, 2014, p-154.

6. Decay of $^{124}Ce^*$ using Skyrme Energy Density Formalism within the Dynamical Cluster-decay Model,
Arshdeep Kaur and Raj K. Gupta,
DAE-BRNS Symp. on Nucl. Phys., **59**, 388 (2014); Banaras Hindu University, Varanasi-221005 (UP), India, Dec 8-12, 2014.

7. Compound nucleus formation probability P_{CN} defined within the dynamical cluster-decay model,
Sahila Chopra, **Arsheep Kaur**, and Raj. K. Gupta,
EPJ Web of Conferences **86**, 00006, (2015).

8. Decay of $^{124}Ce^*$ using Skyrme Energy Density Formalism within the dynamical cluster-decay model,
Arshdeep Kaur, Sahila Chopra, and Raj K. Gupta,
9^{th} Chandigarh Science Congress, CHASCON-2015, February 26-28, 2015, Panjab University, Chandigarh.

9. Effect of Non-Coplanar Degree of Freedom on Non-Compound Nucleus Component in Decay of $^{12}C+^{93}Nb\rightarrow^{105}Ag^*$ reaction,
Sahila Chopra, Arshdeep Kaur, and Raj . Gupta,
9^{th} Chandigarh Science Congress, CHASCON-2015, February 26-28, 2015, Panjab University, Chandigarh.

10. Decay of $^{124}Ce^*$ within the Dynamical Cluster-decay Model using various formulations of nuclear proximity potential,
Arshdeep Kaur, Sahila Chopra, and Raj K. Gupta,
(bbok of abstracts) XXXIV Mazurian lakes Conf. on Phys., Frontiers in Nucl. Phys.-Piaski, Poland, September 1-6, 2015.

11. Decay of $^{217}At^*$ formed in $^{9}Li+^{208}Pb$ reaction within the Dynamical Cluster-decay Model,
Arshdeep Kaur, B. R. Behera, and Raj K. Gupta,
DAE-BRNS Symp. on Nucl. Phys., **60**, 480 (2015); SSSIHL, Prasanthi Nilayam-515134, AP, India, Dec 7-11, 2015.

12. The dynamical cluster-decay model (DCM) vs. Wong model for the study of $^{9}Li + ^{208}Pb$ reaction,
Arshdeep Kaur and Raj . Gupta,
10^{th} Chandigarh Science Congress, CHASCON-2016, February 27-29, 2016, Panjab University, Chandigarh.

13. Non-coplanar Nuclei in Heavy-ion Reactions,
Sahila Chopra, Hemdeep, Arshdeep Kaur, and Raj K. Gupta,
Contribution ICNP 2016: 18th International Conference on Nuclear Physics, May 8-9, 2016, Dubai, UAE. Publishd in Int. Journal of Mathematical, Computational, Physical, Electrical and Computer Engineering **10**, 5 (2016).

Contents

List of Tables

List of Figures

Abstract

The aim of the present work is to study the nuclear structure and orientation effects on the decay of the hot and rotating compound system formed in heavy ion reactions, using the dynamical cluster decay model (DCM) which is based on collective clusterization approach. The neck length parameter, ΔR, is the only parameter of the DCM and is related to "barrier lowering". Within the DCM, the deformation and orientation effects of the reaction partners and decay products are explicitly included along with temperature and angular momentum contributions. The advantage of the DCM over the other statistical models is that, the DCM contains the structural information of the decaying nucleus via the relative preformation probability P_0 of the decaying fragments, before penetrating the interaction barrier. The thesis is organized into the following seven chapters.

Chapter 1, presents the general introduction which includes the status of the experimental and theoretical developments to understand the dynamics of fusion-fission and associated nuclear structure effects. Study of formation and decay of compound nucleus (CN) and noncompound nucleus (nCN) processes is discussed and total fusion cross-section σ_{fusion} is given as a sum of σ_{CN} and σ_{nCN}, each calculated as the dynamical fragmentation process. The CN cross section σ_{CN} is the sum of the evaporation residues (ER) and fusion-fission (ff) (including the intermediate mass fragments, IMFs), cross sections. For studying the formation and decay of CN, the precise and systematic understanding of various nucleus-nucleus interaction potentials is necessary, a brief account of such interactions is summarized in this chapter. Beside this, the role of angular momentum, entrance channels, deformations and orientations, fusion hindrance, etc., have been discussed. Concepts of Compound Nucleus fusion/ formation probability P_{CN} and Compound Nucleus survival probability P_{surv} are also introduced and discussed in this chapter.

Chapter 2 gives the details of the methodology used, the dynamical cluster decay model (DCM) which is based on the Quantum Mechanical Fragmentation Theory (QMFT). Within the DCM, the process of binary decay like neutron evaporation, α-decay, cluster decay, etc., is treated in two steps: In the first step, quantum mechanical preformation probability of the cluster in the mother nucleus is calculated and in the second step the penetration of this cluster through the interaction barrier is calculated. In the DCM, the preformation probability P_0 (which contains information about nuclear structure) of all preformed clusters within the mother nucleus is calculated by solving the stationary Schrödinger equation in mass asymmetry (η) coordinate. The role of temperature dependence of the proximity potential, Coulomb interaction potential, rotational energy and binding energies is also briefly discussed here. Discussion on the Compound Nucleus fusion/ formation probability P_{CN} and the Compound Nucleus survival probability P_{surv} is also there in this chapter. For the interaction potential between the two colliding nuclei, the well known proximity pocket formula, and details of the Skyrme energy density formalism (SEDF) are also described. Finally the Wong formula and its extended version are also described in brief.

In **Chapter 3**, the dynamical cluster-decay model (DCM), an extended version of preformed cluster model (PCM) for ground-state (T=0) decays, is applied to study the decay of proton-rich compound nucleus ^{124}Ce* formed in ^{32}S+^{92}Mo reaction at an above barrier beam energy of 150 MeV. Using the DCM, with effects of deformations up to hexadecapole and "compact" orientations included, for the best fitted cross-sections of 2p, 3p evaporation residues (ERs) and of ^{5}Li, ^{6}Be intermediate mass fragments (IMFs), the, α-nuclei clusters are populated strongly relative to non-α clusters, similar to what was predicted by Gupta and collaborators for ground-state decays of such nuclei, and decay of ^{116}Ba* formed in ^{58}Ni+^{58}Ni reaction at various compound nucleus excitation energies. The compound nucleus formation probability and "barrier lowering/ modification" effects are analyzed, and the role of varying the

deformations of ^{6}Be and/ or ^{8}Be nuclei on relative cross-sections is studied, since the measured deformations are not available. Calculations are also presented for another beam energy of 140 MeV, supporting the above result.

In **Chapter 4**, we have extended the study of ^{124}Ce* formed in ^{32}S+^{92}Mo reaction at beam energy of 150 MeV, using the pocket formula of Blocki *et al.* for nuclear proximity potential, to the use of other nuclear interaction potentials derived from Skyrme energy density functional (SEDF) based on semiclassical extended Thomas Fermi (ETF) approach under the frozen density approximation. The Skyrme forces used are the old SII, SIII, SIV, SKa, SkM and SLy4 and new GSkI and KDE0(v1). α-nucleus structure, over non-α nucleus structure, is preferred for *only* two Skyrme forces, the SIII and KDE0(v1). The intermediate mass fragments (IMFs) window, heavy mass fragments (HMFs) and the near-symmetric and symmetric fission fragments of fusion-fission (ff) process are predicted by considering cross sections of orders observed in the experiment under study. The compound nucleus (CN) formation probability P_{CN} and the survival probability P_{surv} of the CN against fission are also calculated. The extended-Wong model of Gupta and collaborators is also applied, and it is noticed that the ℓ_{max} values and total fusion cross sections are of same order as for the DCM.

In **Chapter 5**, in order to check the behavior of neutron-rich exotic nature of ^{9}Li projectile on the total fusion cross section σ_{fus}, we study the decay mechanism of ^{217}At* formed in ^{9}Li+^{208}Pb reaction within the dynamical cluster-decay model (DCM) at various center-of-mass energies. For a fixed ΔR, we are able to fit $\sigma_{fus} = \sum_{x=1}^{6} \sigma_{xn}$ almost exactly for ^{9}Li on ^{208}Pb and other targets, with σ_{fus} depending strongly on the target mass and its (magic) shell structure. But, the unobserved channels (1n, 2n) and σ_{ff} are strongly over-estimated and the observed individual decay channels (3n-6n) are very poorly fitted. So, different ΔR values, meaning thereby different reaction time scales, are required to fit individually both the observed and unobserved evaporation residue channels (1n-6n) and the ff cross

section σ_{ff}. The non-compound nucleus (nCN) decay cross section σ_{nCN} contributes the most towards total σ_{fus} and due to this CN formation probability P_{CN} <<1 and CN survival probability P_{surv} ≈1 (due to small σ_{ff}). Also, optimum choice of the "cold" (target, projectile) combinations, forming the "hot" compact configuration, is analyzed for the synthesis of CN ^{217}At*.

In **Chapter 6**, the compound nucleus (CN) fusion/ formation probability P_{CN} is determined and its detailed variations given with CN excitation energy E^{*}, center-of-mass energy $E_{c.m.}$, fissility parameter χ, CN mass number A_{CN} and the Coulomb interaction parameter Z_1Z_2. The DCM, with effects of deformations and orientations of nuclei included in it, is used to study the P_{CN} for a number of "hot" fusion reactions forming CN of mass number A $\sim$ 100 to super-heavy nuclei, and for various different nuclear interaction potentials. Interesting results are that the P_{CN}=1 for complete fusion, but P_{CN} <1 or <<1 due to the nCN contribution, depending strongly on different parameters of the entrance channel reaction, but found independent of nuclear interaction potentials used.

Finally, in **chapter 7**, conclusions are summarized and an outlook of our work is presented.

Chapter 1

Introduction

1.1 Introduction

In recent times, large number of experimental and theoretical facilities have been made available making it an ideal time for scientific developments. The universe we live in, the nature around us, is due to various ideas, theories and observations being merged together to explain our own existence. To understand the basics of the origin of physical world, it is necessary to understand the properties of nuclei, i.e., Nuclear Physics. Nuclear Physics started with some theoretical modelling and a few experiments, about a century ago. We know that all the matter in the universe is made of atoms and the atoms are composed of protons, neutrons and electrons and these protons and neutrons are enclosed in a small volume, which we call nucleus and the electrons go around that. The question is: How did we come to know about all this?

In 1909, H. Geiger and E. Mardsen did some experiments [1], where α particles were bombarded on different metals and they found that a small fraction of α particles falling on the metal plates reflects back to such an extent that they emerge again at the side of incident α particles. These authors performed the experiments using different metals of varying thickness. It may be reminded here that, at that time there was nothing like atomic number or Z protons or any of these kinds of

things. This was the beginning of nuclear physics. At the time of this experiment, the atomic model, called the "plum pudding" model given by Thomson was in practice, where the positive and negative charges in an atom are distributed over entire volume. This model was discarded as it was not able to explain the discrete wavelengths in the spectra of light from excited atoms. Also, if charges are distributed or discrete, then the associated electric fields are quite weak. In these experiments, the velocities of α particles were noticed that α particles being heavy and the velocity with which they are coming out of radioactive material are quite high, so they carry large momentum and they are going in as a smeared cloud like thing and then coming back. At that time, some surprise was expressed, but no explanation was conceived. Then came the genius of Rutherford who was in same group of Geiger and Mardsen; his genius was that, from the data of that experiment, he could see that this large deflection is possible only if large electric field is encountered, and such a large electric field can not be created by a distributed charge. So, this charge (either positive or negative) must be concentrated in a small volume to produce such a large electric field. So, Rutherford came out with a new model in 1911 [2]. In his theory he assumed (or established) that atom has positive charge at centre and there is compensatory negative charge around it such that the whole atom is neutral. So, the "nucleus" comes for the first time in the scientific world and there starts the Nuclear Physics. In his paper, Rutherford didn't talk about the stability of the nucleus (or atom) but made a hint that electrons must move in such a way that they are stable. Then, there were a series of papers after that because after the nuclear model of atom came into existence, number of researches and publications were made through.

However, many outstanding achievements were also made before Rutherford: like in 1895, Roengten discovered X-rays and in the following year Becquerel identified radioactivity. A year later J. J. Thomson discovered electron. In the next year, in 1898, Marie Curie separated radium and polonium from their ores. After Rutherford's discovery of nucleus in 1911, the concept of atomic number Z came

from Moseley's study of X- ray spectra which became the basis of identification of elements in periodic table. In the same year N. Bohr gave the theory of atomic spectra where he explained the hydrogen spectrum by giving a model of atom. This discovery of nucleus by Rutherford and atomic model of N. Bohr was followed by the advent of quantum mechanics where various atomic phenomenons were explained. A great amount of work was done on quantum theory by numerous Physicists like deBroglie, Schrödinger, Heisenberg, Pauli, Born and Dirac.

With the discovery of nucleus in 1911, Rutherford found that almost the whole of mass and all the positive charge of atom is located in its very small central core within the radius of the order of 10^{-12} cm. Since that time, many methods have been developed to calculate nuclear size and structure. The values of nuclear radius determined are dependent on the methods used like the nuclear radius found by alpha scattering experiment disagrees with that of electron scattering method. This is because the former case gives the interaction radius, whereas the later case determines the density of charge distribution of the nucleus. The shape of the nucleus was first investigated by Schüler and Schmidt [3] where they determined the nuclear quadrupole moment, which is the measure of the deviation of nuclear charge distribution from spherical symmetry and provides the information about the nuclear shape, from the hyperfine structure in atomic spectra.

The phenomenon of nuclear reactions was first demonstrated by Rutherford in 1919 by the disintegration of nitrogen given as $^{14}\mathrm{N}+^{4}\mathrm{He} \rightarrow ^{17}\mathrm{O}+^{1}\mathrm{H}$. The major event in the history of nuclear physics occurred in 1932, with the discovery of neutron by Chadwick, until then the concept of nuclear structure remained unexplained. After this important discovery, the composition of nucleus was proposed and this concept of nucleus is still valid today where nucleus is made up of neutrons and protons which are called nucleons and they have almost same mass and these nucleons are spin half particles obeying Fermi Dirac statistics.

Nuclear reactions were proposed to be a two step process, consisting of formation of Compound Nucleus (CN) in the first step and then its decay in the second step

where all the memory of the entrance channel is lost. This CN model successfully explained nuclear reactions mainly induced by low energy projectile. The projectile loses all its energy to the target nucleus to form a new, excited, rotating and unstable nucleus called CN. After its formation, the CN excitation energy is transferred to intrinsic degrees of freedom of fragments and angular momentum along with their relative motion. In general, CN loses its excitation energy either by emitting few neutrons or multiple light particles (LPs) to go to the ground state.

The information about the nature of forces existing between nucleons in the nucleus is important to ascertain different properties of nuclei, like nuclear structure, binding energies, etc. Many theoretical predictions and experiments have been performed to predict the nuclear properties accurately. The strong nuclear force binding the nucleons together allow us to derive information on nuclear structure. This short ranged force is saturated in nature and with the assumption of charge independence and saturation, each nucleon occupies almost same size within the nucleus. Then, to solve a paradox in the decay of nucleus, Wolfgang Pauli proposed the existence of neutrino which was confirmed decades later by Clyde L. Cowan and Frederick Reines in 1957.

Study of nuclear reactions and CN decays are the sole probes of nuclear structure. Along with this, model building always played a very vital role. Different model approaches explained (or tried to explain) different aspects of nuclear structure systematically and in a simpler way. Historically, the first model to describe nuclear properties was the liquid drop model (a macroscopic approach). The binding energy per nucleon gave the indication about nuclear forces being saturated in nature from where the idea for this model arose as the nuclear binding energy systematics are similar to the energy of a charged liquid drop. Though this liquid drop model, taken as a classical model, could not be extrapolated to a large extent in the atomic nucleus, yet this model successfully explained the general trends in binding energies *w.r.t.* mass number and the nuclear fission and fusion processes. But this model does not account for the different shapes of atomic nuclei and apart from this a

number of indications show the need for the specific shell model corrections to this liquid drop model.

Also, there is a Fermi gas model, where all nucleons are considered to move within the nuclear volume as elements of a Fermi gas. In this approach the energy levels are widely spaced and only the lowest levels are occupied. A simple independent particle approach required by the Fermi gas model does not contain the detailed features of nucleon-nucleon forces acting inside the nucleus. The difference in energy between the liquid drop nuclear mass and the experimental nuclear mass indicates the presence of certain configurations where the nucleus is more strongly bound than the indications by the uniform filling of orbitals in the Fermi gas model. The existence of shell structure came from the analogous picture of electrons moving in an atom. The precise shell structure inside the nucleus and its associated excitation spectra are of great importance for an overall understanding of nuclear systems. Until the nuclear shell model (a microscopic approach), given by Mayor and Jensen, no other model was able to explain that why nucleons with certain number of protons and neutrons are more stable (i.e., no explanation for so-called magic numbers, given as N=2,8,20,28,50,82 and 126 and Z=2,8,20,28,50 and 82). Shell model treats each nucleon as an independent particle explaining the reaction data nicely, and successfully explained various properties like spin, magnetic moment and nuclear spectra. The properties of nuclei which can not be explained by the models mentioned above, can be explained either by the unified approach of these models, known as collective or unified model or by the Strutinsky macro-microscopic approach of combining Liquid drop model and nuclear shell model (i.e., by normalizing the sum of shell model energy states to an appropriate Liquid drop model energies). Different properties and aspects of nuclear structure like electric quadrupole moments, rotational and vibrational spectrums were nicely explained here. Over the years various developments have been made in the area of nuclear models enriching our knowledge of nuclear structure and various advancements in nuclear physics.

With the development of modern accelerator techniques, which impart higher energies to heavier projectiles, the study of new branch of nuclear physics, i.e., "Heavy Ion Physics" became possible. The nuclei having Z$\geq$2 and A$\geq$4 , i.e., α nucleus or heavier than α nucleus are called Heavy ions, which means that α-particle is the lightest heavy ion. Study of Heavy Ion Reactions (HIR) played a vital role in providing ion-ion interaction potential, which is the very important component in the study of nuclear structure, its stability and decay, elastic or inelastic scattering, estimation of cross section for heavy element synthesis, etc. Basic features of HIR are better understood in terms of interaction potential acting between the centre of mass of two colliding nuclei which consists of long range Coulomb repulsions and short range nuclear attractions. Coulomb force, though plays important role, but is not enough to describe the formation of a stable system. The existence of nucleus is due to the presence of strong nuclear attractive force which overpowered the Coulomb repulsive force between protons. The short range of nuclear force ($\sim$2 fm) puts a severe obstacle to its experimental investigation as compared to other fundamental forces.

Nuclear Physics acts as a bridge between most fundamental and applied topics as it has many potential applications, like ones in science, medicine, technology, radiocarbon dating, material engineering and many more. Before 1980, due to limited ability to produce unstable nuclei, the knowledge on nuclear physics was mainly based on about 300 stable nuclei (compared to about 6000 nuclei). The extension of nuclear phenomenon to unstable nuclei has greatly improved in last 2 to 3 decades as about one third of all known isotopes has been discovered during this period. The nuclear chart, known as "nuclear landscape", is given in Fig. 1.1, where it is shown that around 8000 combinations of nucleons lying between neutron and proton "drip lines" are possible and out of which our knowledge is restricted to around 3000 only. Any unstable nucleus will spontaneously transfer into more stable nucleus if the transformation is allowed by the laws of Physics. This process is known as radioactive decay of the nucleus which is accompanied by the release of ionizing

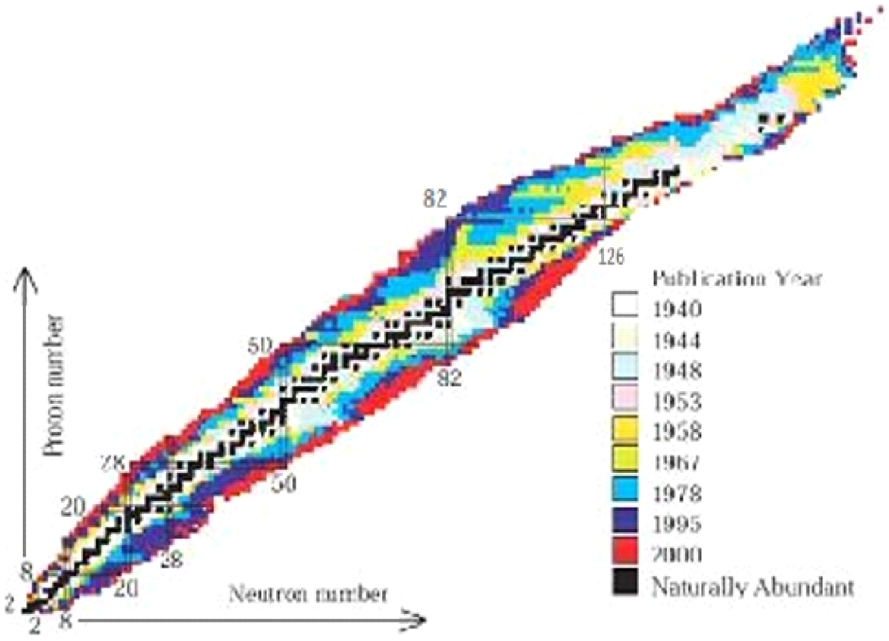

Figure 1.1: An illustrative Nuclear chart.

radiations. Nuclei exhibiting this property are called unstable or radioactive nuclei. This process of nuclear transformation carries important information about nuclear structure and nuclear dynamics. Nuclei can also undergo artificial transformation in nuclear reactions.

The research in nuclear physics related to the study of nuclei having high spin and excitation energy, i.e., nuclei under extreme conditions, may have extreme N:Z (created artificially) or extreme shapes having multi-pole deformations (i.e., β_λ with λ=2,3,4) as shown in Fig. 1.2, where different oscillations of nuclear surface are shown. Generally, elongated (prolate) and flattened (oblate) are the most commonly observed nuclear deformations. λ=2 (lowest multipole) gives the quadrupole oscillations of nuclear surface corresponding to spheroidal shape and quadrupole deformations. Higher multipoles, λ=3,4 represent octopole, hexadecupole oscillations of nuclear surface. These multipole deformations along with the appropriate choice of orientations contributes to the study of enormous exotic shapes which in turn are

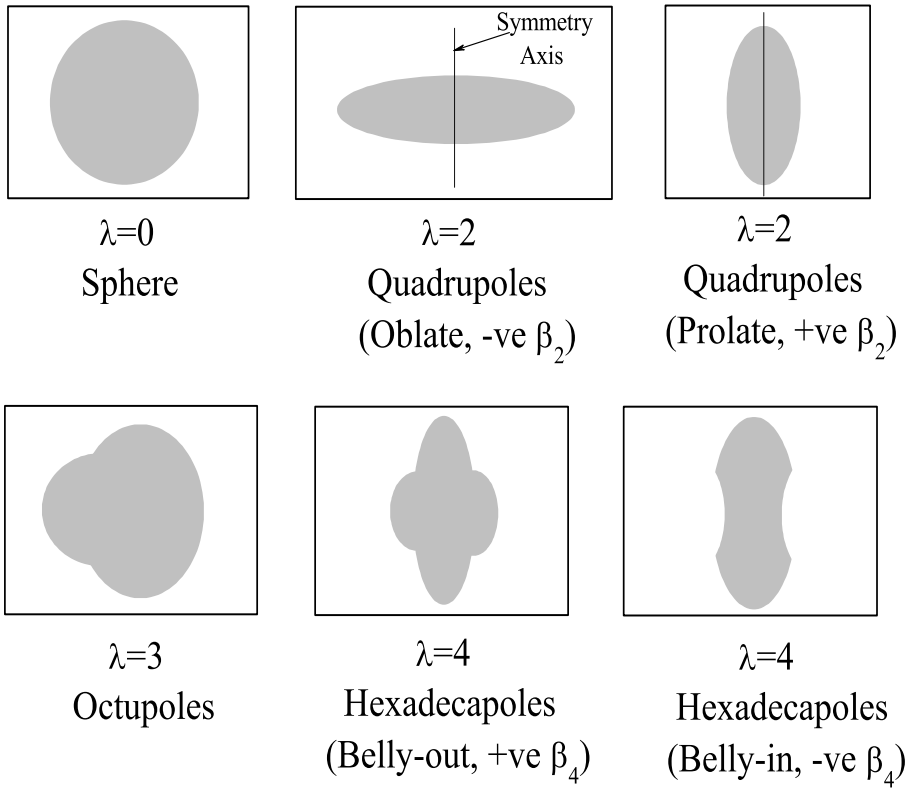

Figure 1.2: Schematic diagrams for various multipole deformations in nuclei. For quadrupole deformations, there are two choices i.e. nuclear matter rotates on short axis (oblate) and on long axis (prolate).

very significant to understand various aspects of nuclear structure and other related nuclear dynamics. Also, whenever deformed configuration is considered for nuclear systems, their orientational behavior can not be ignored.

On the basis of Quantum Mechanical Fragmentation Theory (QMFT) [4–6], Gupta and collaborators showed that nuclear interaction barriers (i.e., barrier position and height) are greatly affected in collisions of deformed and oriented nuclei, making the fusion process more probable at lower energies. On the basis of quadrupole deformations alone, this study provides the "optimum" orientations for the fusion of deformed nuclei and it also investigated the role of hexadecupole deformation in fusion reactions. The optimum orientations are given for "hot-compact" and "cold-elongated" configurations corresponding, respectively, to highest barrier (or smallest interaction radius) and lowest barrier (or largest interaction radius) which are discussed later. A schematic representation for prolate-prolate and oblate-

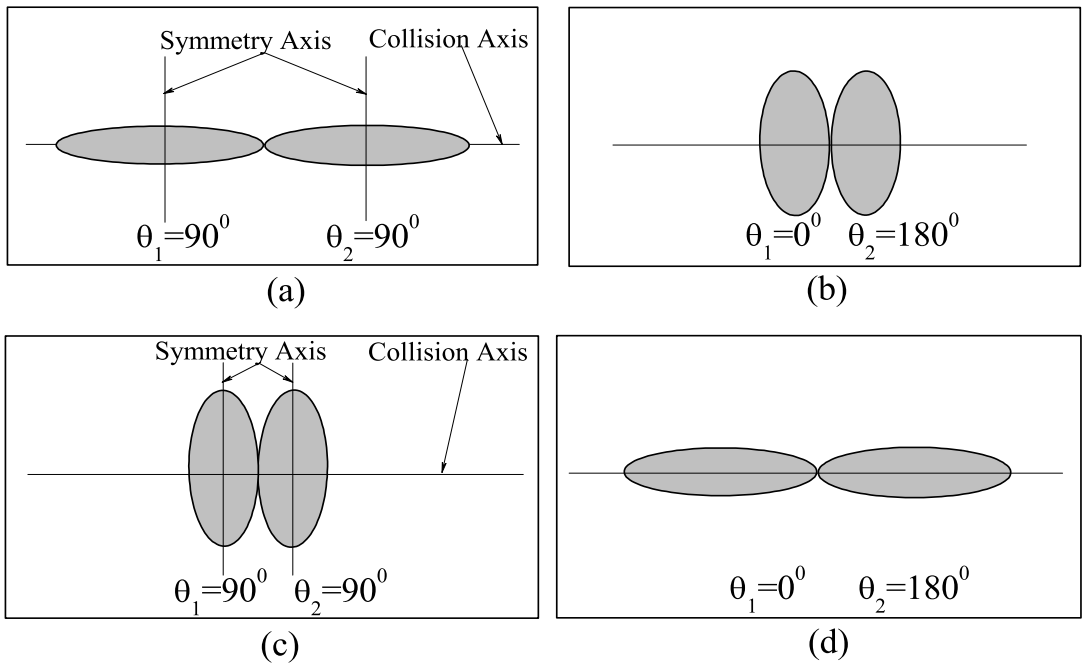

Figure 1.3: Schematic diagrams for deformed nuclei [(a),(b) oblate and (c),(d) prolate only] with corresponding optimum orientations along collision axis for "cold, elongated"[(a), (d)] or "hot, compact"[(b), (c)] configurations, from Table 1 of Ref. [7].

oblate deformed nuclei colliding along collision axis for both "hot compact" and "cold elongated" configurations, is given in Fig 1.3. The orientations θ_i^{opt} are optimized or uniquely fixed, based on the signs of quadrupole deformations β_{2i} alone (i.e., +, - or zero) and it is not affected by signs of hexadecupole deformations [7]. Generally, compact orientations θ_i^c, referring to collisions taking place at smallest interaction radius ("hot" or "cold" fusion depending on their barrier height) may be used [7,8]. The deformations and orientation effects of nuclei are extremely important and needs be incorporated explicitly for the proper study of nuclear dynamics. Along with the temperature and angular momentum effects in the Dynamical Cluster decay model (DCM) [7–12], the deformations and orientation effects of the reaction partners and decay fragments are also taken care of.

Description of nuclear reactions requires identification of projectile with associated incident energy, target nucleus and decay fragments or the reaction products. Broadly, nuclear reactions are categorized into two types: (i) Fusion reactions and

(ii) Fusion-Fission reactions. Both these processes play significant role in the production of new elements and their further studies and applications. In the nuclear fusion process, two nuclei fuse together to form a compound nucleus. In the low energy heavy ion reactions, during the interaction between two stable nuclei at an energy above Coulomb barrier, nuclear fusion takes place where all the angular momentum of initial system is retained. Sufficient amount of kinetic energy in the entrance channel is required to overcome the Coulomb repulsions and to form an excited CN. The energy barrier consisting of Coulomb and nuclear potentials opposes the fusion reaction but the long range repulsive Coulomb force is offset by stronger and attractive, but short range, nuclear force. The fusion process is the quantum mechanical tunnelling through the one dimensional barrier formed by the Coulomb potential, centrifugal potential and the nuclear potential. So the knowledge of potential barrier between two nuclei is utmost important for the systematic study of nuclear reactions. Also, for the successful formation of heavy nuclei, a thorough understanding of fusion-fission process is very essential.

Fusion reactions, which initially included only light nuclei, have now been extended to include heavier targets and projectiles. For example, in hot fusion reactions, actinides are used as targets and, in cold fusion reactions, ^{208}Pb are used as projectiles in the inverse kinematics. In the production of Super Heavy Elements (SHEs), where increase in nuclear charge decreases its stability against fission, the only successful method for such a synthesis is the complete fusion reactions, where the projectile and target merge to form a CN. This CN if de-excite with the emission of 1-2 neutrons and have excitation energy from 10-20 MeV, is called "cold fusion". If the excitation energy of the CN lies in the range of 40-50 MeV and number of neutrons emitted are more than 2, then it is called "hot fusion" reactions. The idea of "cold fusion" was first given by Gupta and Greiner and their collaborators in 1974-75 in terms of Quantum Mechanical Fragmentation Theory QMFT [4–6]. "Cold fusion" reactions have lowest interaction barrier and largest interaction radius having elongated, i.e., "non compact" nuclear shape. These reactions correspond to

minima in fragmentation potential energy surface. The "hot fusion" reactions are characterized by largest interaction barrier and smallest interaction radius, i.e., a "compact" nuclear shape.

Nuclear decay studies play an important, indispensable role in understanding of nuclear phenomenon and properties in general, and about nuclear structure in particular. The phenomenon of cluster decay, which is the spontaneous emission of fragments heavier than α particles, is the Quantum mechanical tunnelling process where the clusters penetrates the potential barrier and come out of the parent nucleus. Based on the QMFT, the successful description of cluster decay was given by Săndulescu *et al.* [13], few years prior to its experimental discovery. Phenomenon of cluster decay is the intermediate step between α radioactivity and fission and is different from fission by the fact that in fission process, nucleus continuously deforms as it passes over the Coulomb barrier breaking itself into the comparable fragments and reaches saddle point configuration whereas, in cluster decay [14], the α particle and clusters heavier than α particle but smaller than the lightest fission fragments are preformed in the parent nucleus with relative preformation probability P_0, which then penetrate the confining interaction barrier. The nuclear shell structure play a very vital role in cluster decay process. Also, in addition to nuclear shell effects, the nuclear deformations and orientations play a very significant role in cluster decay process.

In 1928, Gamow discovered Quantum mechanical tunnelling as a phenomenon associated with α decay, which further could be used to understand various concepts of nuclear reaction dynamics and other related aspects of Nuclear Physics. This was basically the first application of Quantum mechanics to nuclear physics. Based on Gamow's theory of barrier penetration, there are two kinds of models to describe cluster decay process. First one is the Unified Fission Model (UFM), like the Analytic Super-Asymmetric Fission Model (ASAFM) of Săndulescu, Poenaru, and Greiner [13], where, they calculated cluster formation probability as a part of interaction barrier penetration, and the second one is the Preformed Cluster Model

(PCM) based on QMFT of Gupta and Collaborators [14] where the process of binary decay is explained in two steps: In the first step quantum mechanical preformation probability of the cluster in CN is calculated followed by the penetration of the cluster through the barrier in second step. Here, the cluster preformation is calculated by solving the Schrödinger equation for dynamic flow of masses and charges. The square well potential was used for Gamow's theory of α decay whereas, UFM and PCM use the more realistic nuclear interaction potentials. It is to be noted that, in terms of potential barrier, cluster decay is in fact a fission process where the structure effects of the CN are included via the preformation of fragments but with no level density calculations, i.e., without any phase space arguments.

With the inclusion of orientation and deformation effects, the barrier height gets lowered which means that the nuclear structure effects of projectile and target and their relative orientations influence the interaction potential and hence fusion cross-sections to a large extent. To establish the effect of orientations and deformations on fusion reactions, various theoretical and experimental studies have been made for the collision between deformed as well as oriented nuclei [7,15–22], where it is shown that during the collision of deformed and oriented nuclei, the fusion barrier height changes leading to barrier height distribution around spherical Coulomb barrier.

The main research tool of nuclear reaction's physics is the high energy beam of particles like neutrons, protons, α-particles or other heavy ions projected on different nuclear targets. On the basis of energy of incident projectile, the nuclear reaction dynamics is usually classified into three groups namely low energy (E $\leq$15 MeV/nucleon), intermediate energy (15<E<500 MeV/nucleon)and high energy nuclear reactions (E$\geq$500 MeV/nucleon). In high energy reactions direct nucleon-nucleon interactions take place whereas in low energy reactions the average nuclear force field between the two nucleons dominates which ensures the possibility of more than one decay channel. The average nuclear force field mentioned here is highly influenced by entrance channel, temperature and angular momentum considerations along with the inclusion of deformations and orientation effects. In intermediate

energy nuclear reactions, both the above mentioned aspects are included. Here, in this thesis, we have confined ourselves to low energy nuclear reactions, where the decay process of different nuclei are explored via a collective clusterization process. In low energy reactions, a comprehensive study of different types of emissions from the excited state of CN as well as ground state of parent nuclei is highly desirable, as it provides information about nuclear structure and nuclear forces. The concept of preformation probability P_0 is used in the collective clusterization approach, which implies that structure effects are included via P_0 and it depends not only on the decay products but on all possible fragmentation of decaying nucleus.

In a complete fusion reaction, the kinetic energy, mass and angular momentum are completely transferred between target and projectile and the so formed composite system completes a number of rotations during which it equilibrates in all degrees of freedom. The kinetic energy of projectile in centre of mass frame is converted into excitation energy of CN and the hot and rotating CN so formed in low energy heavy-ion reactions (HIR), having high excitation energy and carrying large angular momentum, disintegrates or loses its excitation energy and decays by emitting various evaporation residue ER consisting of multiple light particles LPs (n, p, α) and (or) γ rays; Intermediate Mass fragments (IMFs) having $5 \leq A \leq 20$ and $2 \leq Z \leq 10$; symmetric and near symmetric fission fragments (SF and nSF) depending on its mass. The contribution of IMFs to cross section is only 5-10% of LPs. Different mass regions of CN give different combinations of these above mentioned processes. In heavy systems $A_{CN} \sim 200$, fission mode dominates but in case of light compound systems, there is a competition between fission and fusion ER decay modes. For example, in ^{64}Ni+^{100}Mo $\rightarrow^{164}$Yb* [24] and ^{9}Li+^{208}Pb $\rightarrow^{217}$At* [25, 26], only ERs are observed, whereas in ^{12}C+^{93}Nb $\rightarrow^{105}$Ag* [27, 28] and ^{32}S+^{92}Mo $\rightarrow^{124}$Ce* [29], some IMFs along with ERs are also observed. In ^{64}Ni+^{112,118,124,132}Sn $\rightarrow^{176,182,188,196}$Pt* [30] and ^{48}Ca+^{154}Sm $\rightarrow^{202}$Pb* [31] both ERs and ff are observed. So, we can say that for different CN, different combinations of the above mentioned processes are possible.

Dynamical cluster-decay model (DCM) of Gupta and collaborators [7–12] which is a reformulation of PCM [14,32] and is based on well known QMFT [4–6], is used to study the decay of hot (Temperature T $\neq$0) and rotating (angular momentum $\ell \neq$0) compound system formed in HIR. QMFT is the unified description of two body channels in both fission and fusion of nuclei. It is the only theory, given prior to the experiments, that brings out clearly the applicability of the quantum concept of probability and the role of shell effects for the fusion reactions and also for the other two related processes of fission and the cluster radioactivity. Like PCM, the DCM also gives the relative probability of all different channels through which the CN decays. Within the DCM, the decay is studied as a collective clusterisation process for the emission of ERs and IMFs, where each decay path is treated on equal footing as dynamical collective mass motion of preformed clusters or fragments through the barrier, contrary to statistical models where each type of emission is treated as a different process. Also, within the DCM there is an advantage over other statistical fission models, that the structure effects of CN are included through the preformation of fragments with associated preformation probabilities before penetrating the barrier. It is to be noted that the nucleus-nucleus potential used in DCM is either through the proximity potential pocket formula with temperature effects included via the nuclear radii and surface width [33, 34] or with semiclassical ETF approach of SEDF where the temperature dependence is taken from Ref. [35]. Also, Wong formula [36] is used for calculation of fusion cross section, which is a special case of the DCM with preformation probability P_0=1. The difference between two models (Wong and DCM) is that the penetrability P in Wong formula is calculated in Hill-Wheeler [37] approximation of inverted harmonic oscillator for the the incoming channel interaction potential V_ℓ(R), whereas in DCM the same is based on Wentzel-Kramers-Brillouin (WKB) approximation.

In addition to compound nucleus decay (the ER and ff), various non-Compound nucleus decay (nCN) processes, like quasi fission (qf), Deep Inelastic Collision (DIC),

Incomplete Fusion (ICF), etc., are also observed, depending on the beam energy and mass asymmetry. When the entrance channel nuclei do not loose their identity and the non-equilibrated CN is formed which decays into projectile- and target-like fragments, with only a few nucleon exchange between them, then as the surfaces of two colliding nuclei overlap for a very short time corresponding to a partial rotation of a nuclear molecule, this process is called qf. It is known from literature that when the interaction between two nuclei is via their lateral surfaces (near-side collision), formation of spherical CN is more probable, whereas, in the elongated configuration, when interaction between two nuclei is via their poles (i.e., near-tip collision), a high qf probability is expected [38, 39]. In case of DIC, the target and projectile stick together for a longer time dissipating ample amount of energy, and significant number of nucleons are exchanged between target and projectile during this long interaction time. Mass asymmetry of entrance channel is mostly preserved in DIC. For the symmetric target projectile combinations, i.e., nuclear systems having large Coulomb repulsion in the entrance channel, DIC is the major contributor to nCN channel. DIC has reaction time scale less than qf which is further less than CN process.

ICF is the another contributing mechanism towards the nCN process, where the projectile nucleus break up into two fragments near the surface of target nucleus. Out of the two fragments one retreats with unchanged velocity, whereas the other fragment fuses with the target nucleus to form intermediate complex system in the excited state which de-excites by particle evaporation [40, 41]. It differs from complete fusion (CF) by the fact that in CF, entire projectile fuses with the target nucleus forming fully equilibrated CN. In case of CF, linear momentum is totally transferred to the target nucleus, whereas, in ICF, there is only partial transfer of projectile angular momentum. For the systems having entrance channel mass asymmetry, ICF is the dominant nCN process. So, the total fusion cross section is the sum total of CN cross section and nCN decay cross section (which could be any one of the qf, DIC or ICF processes).

Thus, the properties of entrance channel nuclei, like mass asymmetry plays a vital role in nuclear reaction dynamics of nCN process. These processes mentioned here generally depend on excitation energy, angular momentum, impact parameter, atomic charges and masses of participating nuclei, etc. It is equally important to investigate nCN process along with CN process as it also provides important information regarding nuclear structure and other implications in nuclear dynamics and related phenomenons. Fig. 1.4 illustrates schematically the various components of compound nucleus (CN) decay/ fusion cross section, also called the CN production cross section, or simply the (total) fusion cross section σ_{fusion}, given as sum of σ_{CN} and σ_{nCN}.

In nuclear reactions, the concept of compound nucleus fusion/ formation probability P_{CN} [42] arises from the compound nucleus (CN) model of N. Bohr [43] wherein for the complete fusion in entrance channel he assumed P_{CN}=1, and treated the CN decay statistically. However, in the decay channel, non-compound nucleus (nCN) decays, as mentioned above, also contribute to the overall (fusion) cross section, which means P_{CN} <1 for the CN content, and hence Bohr's CN-model needs an extention/ re-examination. The P_{CN} is the least understood quantity, but quite important for the study of heavy ion reactions. Another quantity of interest in heavy ion reactions, not fully understood, is the CN survival probability P_{surv}, [44] introduced to account for the emission of light particles (LPs) or neutrons with respect to the fusion-fission process. In other words, P_{surv} is the probability that the fused system will de-excite by emission of neutrons or LPs (equivalently, the evaporation residue ER) rather than fission. For a fissionless decay, P_{surv}=1, i.e., the CN decays via neutrons or LPs emission alone. On the other hand, if only fission takes place, then P_{surv}=0, implying that no neutrons (or LPs) emission occur and there is a complete instability against fission. It is evident from above that P_{CN} takes care of the nCN effects, and P_{surv} looks after the ff process. Within DCM we have successfully studied P_{CN} [42] and P_{surv} [44] for various "hot" fusion reactions.

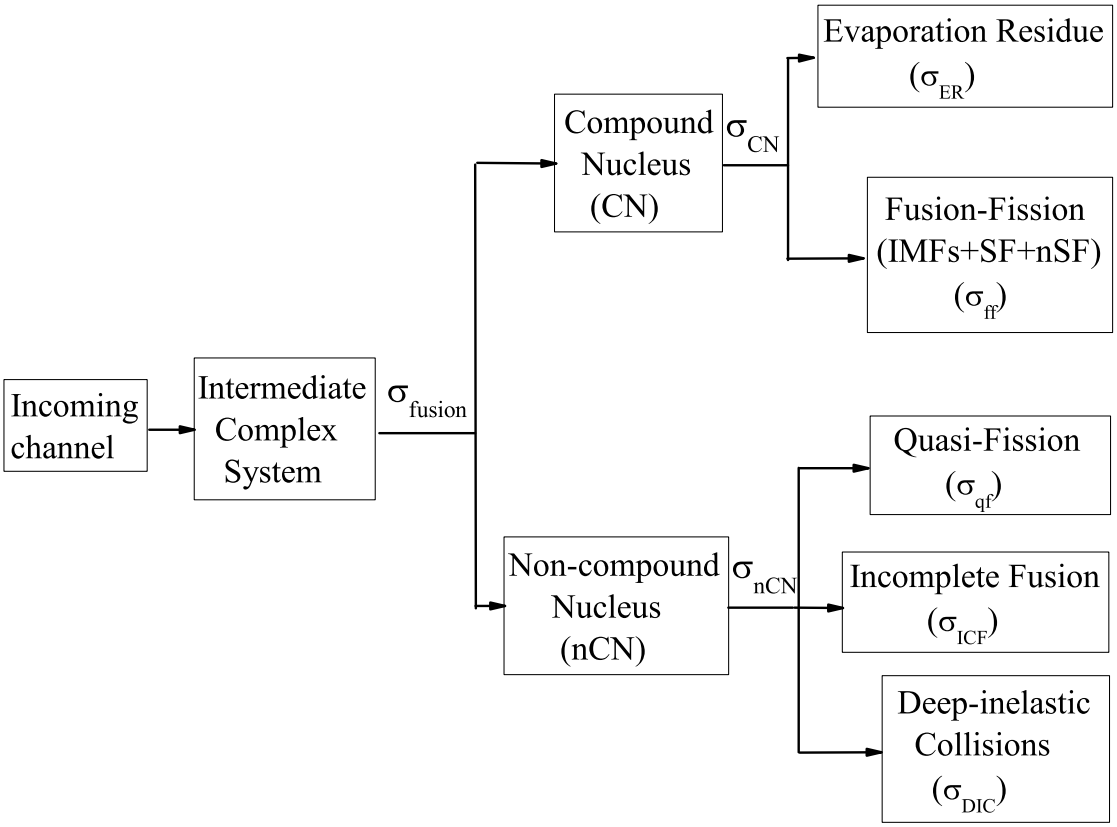

Figure 1.4: Schematic diagram of the formation/ decay path used to calculate the compound nucleus and non-compound nucleus decay cross sections, taken from Ref. [42].

For the proper understanding of nuclear phenomena, the nucleon-nucleon interaction plays the major role. The (total) interaction potential, which is the function of relative separation distance, comprises of the sum of the long range Coulomb repulsive interaction, centrifugal interaction and the nuclear potential terms. The Coulomb and centrifugal part of the interaction potential are very well known, however the nuclear interaction part is not that much understood. Also, the Coulomb potential alone cannot define the barrier, so a proper choice of nuclear potential is necessary to understand heavy ion reaction dynamics. The direct information about fusion barriers can not be imparted by experiments alone as all experiments measure the fusion cross-sections and then using theoretical models, one can extract the fusion barriers. Theoretical models are useful in the study of the nuclear in-

teractions at a microscopic/ macroscopic level. So, there is a need of an accurate and microscopic methods to calculate the ion-ion interaction between the colliding nuclei. Out of the several nuclear potentials used in literature, the two commonly used approaches for calculating the ion-ion potentials are:

(a) Phenomenological models: A simple analytical expression for calculating nucleus-nucleus interaction potential is used in these models, known as proximity potential. These proximity potentials, which are based on the proximity force theorem, implying that the nuclear part of the interaction potential is the product of factors depending on the mean curvature of the interaction surface and a universal function (which depends on the separation distance) and is independent of colliding nuclei masses, play very significant role for majority of microscopic/ macroscopic fusion models. This process plays important role for understanding nuclear reaction dynamics at low energies. At first, Bass [45, 46] introduced an expression for calculating the interaction potential and following that Blocki [47] gave a formula (which is a function of separation between the surfaces of the two colliding nuclei), known as the pocket formula of proximity potential. With time, a number of modifications were made in the proximity potential through the surface energy coefficient or universal function and/ or through nuclear radius to explain experimental data.

(b) Energy density formalism (EDF): In EDF, the nucleus-nucleus interaction potential is calculated as a function of separation distance and is defined as the energy expectation value difference of the colliding nuclei that are overlapping (i.e., at a finite separation R) and when they are completely separated (i.e., at R= ∞) [48, 49]. The microscopic background to construct the EDF model is considered to be the Hartree-Fock (HF) method. HF was first adopted by Vautherin and Brink [50] to study the ground state properties of some spherical nuclei by using Skyrme interaction [51]. The complete HF calculations were not possible in EDF because of the non-availability of expressing kinetic energy density (τ) of the compound nucleus at HF level. To do away with this problem, semiclassical approaches to

this quantity based on Thomas-Fermi (TF) method or its extensions, the Extended Thomas Fermi method (ETF) have been used to obtain τ.

ETF approach of Grammaticos and Voros [52] is the semiclassical expansions based on the Wigner transformation and was applied to fermions governed by a one-body Hamiltonian. To provide an accurate description of the nuclear surface expansions upto fourth order in $\hbar$ of density matrix for different spin-independent potentials were taken. Using the semiclassical expression the total energy of the system becomes a function of the nucleon density alone. At first no spin dependent term is considered in the calculations but in the later Grammaticos and Voros [53], the spin orbit part is included by extending the semiclassical expansions to a case where the effective one-body Hamiltonian for the nucleons containing spin-dependent terms. Thereupon, Gupta and collaborators [54–57], studied the role of spin-orbit density of interaction potential in microscopic shell model formulation of the Skyrme energy density formalism (SEDF) which has a significant contribution to fusion cross sections and also in the α-nucleus structure of colliding N=Z nuclei, α-nuclei and its suppression for the colliding non-α-nuclei. In Ref. [58], it was shown that both approaches (semiclassical Formulation and microscopic shell model) can reproduce exact shell effects if results of the semiclassical SEDF calculations are normalized with respect to the (one or both) spin saturated nuclei.

In this thesis we have used EDF given by Vautherin and Brink which make use of density dependent Skyrme interactions consisting of spin dependent and spin independent part with in semiclassical ETF approach [52, 59, 60]. The Skyrme force depends on limited number of parameters and is an effective interaction providing a zero-range potential. In literature there are some 240 Skyrme interaction parameter out of which only 16 satisfy the present understanding of physics of nuclear matter over a wide range of applications [61]. These 16 forces are obtained by using the Generalized Skyrme effective force (GSEF) [62,63] hamiltonian and satisfy a number of properties like rms radii, binding energy, charge, etc., mostly for spherical and or

neutron rich nuclei. For nuclei which are neutron deficient, other forces having single spin-orbit term may play important role in the calculation of fusion cross-sections.

There are two main assumptions for calculating interaction potential by EDF; the first approximation is where the collision is very slow and at each stage of collision, the nucleons of the colliding systems reach the equilibrium configuration, called the 'adiabatic approximation'; and the second approximation is that the time of collision is so small that the internal structure of two ions is unchanged and nuclear density overlap without changing their shapes, known as 'sudden density approximation' which includes the effect of exchange terms due to anti-symmetrization. The sudden density approximation minus the effect of exchange terms is called as frozen density approximation [64]. The exchange effects occur for a composite system as kinetic energy density $\tau(\rho)$ and spin orbit density J(ρ) are expressed as the functions of ρ_i (i=1,2 for two nuclei), which in turn, is the sum of their nucleon densities (ρ_i=ρ_{in}+ρ_{ip}) with ρ=ρ_1+ρ_2, whereas, in frozen density, the combined nucleon densities are simply expressed as the sum of the densities of two incoming nuclei. It is shown in literature [65] that the barriers obtained by the frozen densities approximation are more realistic than that obtained from the sudden approximation. Following this systematic study, we follow frozen density approximation in our work. Since, in semiclassical ETF approach, the kinetic energy density $\tau(\vec{r})$ and spin-orbit density J($\vec{r}$) are expressed as functions of nucleon density $\rho(\vec{r})$ and its derivatives, used in self-consistent variational approach taking nucleon densities as the variational quantities, the SEDF becomes a functional of nucleon densities alone, and so eliminates completely the use of single particle wave functions. The (variational) nucleon densities are taken as modified two-parameter Fermi density with an additional parameter [59, 60, 66, 67]. Though the higher order contributions [53, 59, 60] to both kinetic energy density $\tau(\vec{r})$ and spin-orbit density J($\vec{r}$) are available in semiclassical approach at ETF level, yet second order terms are enough for numerical convergence [60] as $\tau(\vec{r})$ and J($\vec{r}$) are taken up to second order only.

1.2 Organization of the Thesis

The thesis is organized as follows:

Chapter 2 gives the details of the dynamical cluster-decay model (DCM) for the decay of hot and rotating compound nucleus. DCM is a reformulation of the preformed cluster model (PCM) for ground state decay, based on the Quantum Mechanical Fragmentation Theory (QMFT) for binary fragmentation, using a collective mass transfer process. The orientation and deformation effects are duly incorporated in DCM as well as in PCM, along with the use of "optimum" or "compact" orientations, for incoming as well as for decaying fragments. The DCM is a two step process: The first step is the formation of the cluster in CN, and in the second step the preformed cluster penetrates the barrier. In this model the preformation probability P_0 of all possible clusters within the mother nucleus is calculated. The temperature dependence of proximity potential, Coulomb interaction potential, binding energies and rotational energy are also discussed. Different types of the nuclear potentials, one using proximity theorem and other using Skyrme energy density formalism of Vautherin and Brink are also discussed. Wong model for calculation of fusion reaction cross sections, which is a special case of the DCM with preformation probability P_0=1, is also given in this chapter.

In **Chapter** 3, the dynamical cluster-decay model (DCM), an extended version of preformed cluster model (PCM) for ground-state (T=0) decays, is applied to study the decay of proton-rich compound nucleus ^{124}Ce* formed in ^{32}S+^{92}Mo reaction at an above barrier beam energy of 150 MeV. Application of the statistical code PACE4 to experimental data shows large deviations in all cases of proton cluster's (2p, 3p and 4p) evaporation residue (ER) and the non-α nucleus ^{6}Be intermediate mass fragment (IMF). Furthermore, the α-nucleus ^{8}Be decay is not observed in this experiment (not even the upper limit is given). Using the DCM, with effects of deformations up to hexadecapole and "compact" orientations included, for the best fitted cross-sections of 2p, 3p ERs and of ^{5}Li, ^{6}Be IMFs, the relative cross-section of ^{8}Be is

found to be more than that of ^{6}Be, possibly due to the α-nucleus structure of ^{8}Be. The same is shown to be true for ^{12}C *vs.* ^{10}C, i.e., α-nuclei clusters are populated strongly relative to non-α clusters, similar to what was predicted by Gupta *et al.* [70] for ground-state decays of such nuclei, and decay of ^{116}Ba* formed in ^{58}Ni+^{58}Ni reaction at various compound nucleus excitation energies [71]. The only parameter of the DCM is the neck-length ΔR, related to "barrier lowering" parameter. The compound nucleus formation probability and "barrier lowering/ modification" effects are analyzed, and the role of varying the deformations of ^{6}Be and/ or ^{8}Be nuclei on relative cross-sections is studied, since the measured deformations are not available. The ones used here are from relativistic mean-field calculations [$\beta_2(^{6}\text{Be})$=-0.087 and $\beta_2(^{8}\text{Be})$=-0.094]. Calculations are also presented for a beam energy of 140 MeV, supporting the above result.

Chapter 4 extends the above noted study of ^{124}Ce* formed in ^{32}S+^{92}Mo reaction at an above barrier beam energy of 150 MeV, using the pocket formula of Blocki *et al.* for nuclear proximity potential in the dynamical cluster-decay model (DCM) (Chapter 3), to the use of other nuclear interaction potentials derived from Skyrme energy density functional (SEDF) based on semiclassical extended Thomas Fermi (ETF) approach under the frozen density approximation. The Skyrme forces used are the old SII, SIII, SIV, SKa, SkM and SLy4 and new GSkI and KDE0(v1), given for both normal and isospin-rich nuclei. It is found that the α-nucleus structure, over non-α nucleus structure, is preferred for *only* two Skyrme forces, the SIII and KDE0(v1). An extended intermediate mass fragments (IMFs) window, along with the new decay region of heavy mass fragments (HMFs) and the near-symmetric and symmetric fission fragments, which on adding the complementary heavy fragments, refers to $(A/2)\pm12$ mass region of fusion-fission (ff) process are predicted by considering cross sections of orders observed in the experiment under study. For the predicted (total) fusion cross-section, the survival probability P_{surv} of the compound nucleus (CN) against fission is shown to be very small because of the very large pre-

dicted ff component. On the other hand, the CN formation probability P_{CN} is found to be nearly equal to one, and hence the decay under study is a pure CN decay for all the nuclear potentials considered, since the estimated non-compound nucleus (nCN) content is almost negligible. We have also applied the extended-Wong model of Gupta and collaborators, and find that the ℓ_{max} values and total fusion cross sections are of same order as for the DCM. Thus, the extended-Wong model, which describes only the total fusion cross section in terms of the barrier characteristics of the entrance channel nuclei, could be useful for an initial estimate for experiments, to be fully treated on the DCM for all the observed decay products.

In contrast to the decay of a proton-rich CN ^{124}Ce* (Chapter 3 and 4), in **Chapter** 5 we study the decay mechanism of ^{217}At* formed by neutron-rich projectile ^{9}Li in ^{9}Li+^{208}Pb reaction within the dynamical cluster-decay model (DCM) at various center-of-mass energies. The idea is to check the behavior of the neutron-rich exotic nature of ^{9}Li projectile on the (total) fusion cross section σ_{fus}. Experimentally, only the isotopic yield of heavy mass residues $^{211-214}$At* [equivalently, the light-particles (LPs) evaporation residue cross sections σ_{xn}, x=3-6 neutrons emission] are measured, with the fusion-fission (ff) component σ_{ff} taken zero. For a fixed neck-length parameter ΔR, the only parameter in the DCM, we are able to fit $\sigma_{fus} = \sum_{x=1}^{6} \sigma_{xn}$ almost exactly for ^{9}Li on ^{208}Pb and other targets, with σ_{fus} depending strongly on the target mass and its (magic) shell structure. However, the observed individual decay channels (3n-6n) are very poorly fitted, with unobserved channels (1n, 2n) and σ_{ff} strongly over-estimated. Different ΔR values, meaning thereby different reaction time scales, are required to fit individually both the observed and unobserved evaporation residue channels (1n-6n) and σ_{ff}, but then the compound nucleus (CN) contribution σ_{CN} is very small ($< 1\%$), and the non-compound nucleus (nCN) decay cross section σ_{nCN} contributes the most towards total σ_{fus} ($=\sigma_{CN}+\sigma_{nCN}$). Thus, ^{9}Li induced reaction is more of a quasi-fission-like nCN decay. Then, the CN formation probability $P_{CN} << 1$ and CN survival probability $P_{surv} \approx 1$. Also, optimum choice

of a "cold" (target, projectile) combination, forming "hot" compact configuration, is analyzed for the synthesis of CN ^{217}At*.

In **Chapter** 6, the compound nucleus (CN) fusion/ formation probability P_{CN} is defined and its detailed variations with CN excitation energy E^{*}, center-of-mass energy $E_{c.m.}$, fissility parameter χ, CN mass number A_{CN} and the Coulomb interaction parameter Z_1Z_2 are studied for the first time within the dynamical cluster-decay model (DCM). The model is a non-statistical description for the decay of CN to all possible processes. The (total) fusion cross section σ_{fusion} is sum of the CN and non-compound nucleus (nCN) decay cross sections, each calculated as the dynamical fragmentation process. The CN cross section σ_{CN} is constituted of the evaporation residues (ER) and fusion-fission (ff), including the intermediate mass fragments (IMFs), each calculated for all contributing decay fragments (A_1, A_2) in terms of their formation and barrier penetration probabilities P_0 and P. The nCN cross section σ_{nCN} is determined as the quasi-fission (qf) process where P_0=1 and P is calculated for the entrance channel nuclei. The DCM, with effects of deformations and orientations of nuclei included in it, is used to study the P_{CN} for about a dozen "hot" fusion reactions forming CN of mass number A $\sim$ 100 to super-heavy nuclei, and for various different nuclear interaction potentials. Interesting result is that the P_{CN}=1 for complete fusion, but P_{CN} <1 or <<1 due to the nCN contribution, depending strongly on different parameters of the entrance channel reaction, but found independent of nuclear interaction potentials used.

Finally, in **Chapter** 7, we summarize the results of this work.

Bibliography

[1] H. Geiger and E. Mardsen Proc. Roy. Soc. A **82** p. 495-500 (1909).

[2] E. Rutherford, Philosophical Magazine Series 6, Vol. **21**, p. 669-688 (1911).

[3] H. Schüler and T. Schmidt, Z. Physik **98**, 430 (1935).

[4] J. Maruhn and W. Greiner, Phys. Rev. Lett. **32**, 548 (1974).

[5] R. K. Gupta, W. Scheid, and W. Greiner, Phys. Rev. Lett. **35**, 353 (1975).

[6] R. K. Gupta and W. Greiner, in *Heavy Elements and Related New Phenomenon*, edited by W. Greiner and R. K. Gupta (World Scientific, Singapore, 1999), Vol. I, p. 397; *ibid* Vol. I, p. 536.

[7] R. K. Gupta, M. Balasubramaniam, R. Kumar, N. Singh, M. Manhas, and W. Greiner, J. Phys. G: Nucl. Part. Phys. C **31**, 631 (2005).

[8] R. K. Gupta, M. Manhas, and W. Greiner, Phys. Rev. C **73**, 054307 (2006).

[9] M. Balasubramaniam, R. Kumar, R. K. Gupta, C. Beck, and W. Scheid, J. Phys. G: Nucl. Part. Phys. **29**, 2703 (2003); R. K. Gupta, R. Kumar, N. K. Dhiman, M. Balasubramaniam, W. Scheid, and C. Beck, Phys. Rev. C **68**, 014610 (2003).

[10] B. B. Singh, M. K. Sharma, and R. K. Gupta, Phys. Rev. C **77**, 054613 (2008).

[11] M. K. Sharma, S. Kanwar, G. Sawhney, R. K. Gupta, and W. Greiner, J. Phys. G: Nucl. Part. Phys. **38**, 055104 (2011); D. Jain, R. Kumar, M. K. Sharma, and R. K. Gupta, Phys. Rev. C **85**, 024615 (2012).

[12] M. Kaur, R. Kumar, and M. K. Sharma, Phys. Rev. C **85**, 014609 (2012); M. Kaur and M. K. Sharma *ibid.* **85**, 054605 (2012).

[13] A. Săndulescu, D. N. Poenaru, and W. Greiner, Sov. J. Part. Nucl. **11**, 528 (1980).

[14] S. S. Malik and R. K. Gupta, Phys. Rev. C **39**, 1992 (1989).

[15] N. Malhotra and R. K. Gupta, Phys. Rev. C **31**, 1179 (1985).

[16] A. Iwamoto, P. Möller, J. R. Nix, and H. Sagawa, Nucl. Phys. A **596**, 329 (1996).

[17] M. Manhas and R.K. Gupta, Phys. Rev. C **72**, 024606 (2005).

[18] R. K. Gupta, M. Manhas, G. Münzenberg, and W.Greiner, Phys. Rev. C **72**, 014607 (2005).

[19] K. Nishio, H. Ikezoe, S. Mitsuoka, K. Satou, and S.C. Jeong, Phys. Rev. C **63**, 044610 (2001).

[20] D.J. Hinde, M. Dasgupta, J.R. Leigh, J.P. Lestone, J.C. Mein, C.R. Morton, J.O. Newton, and H. Timmers, Phys. Rev. Lett. **74**, 1295 (1995).

[21] M. Dasgupta, D.J. Hinde, J.R. Leigh, and K. Hagino, Nucl. Phys. **A630**, 78C (1998).

[22] Yu. Ts. Oganessian, in *Heavy Elements and Related New Phenomena*, edited by W. Greiner and R.K. Gupta, World Scientfic, Singapore, p. 43, (1999).

[23] K. Mahata, S. Kailas, A. Shrivastava, A. Chatterjee, P. Singh, S. Santra, and B. S. Tomar, Phys. Rev. C **65**, 034613 (2002).

[24] M. Bansal, S. Chopra, and R. K. Gupta, Phys. Rev. C **86**,034604 (2012).

[25] Arshdeep Kaur, Bivash R. Behera, and Raj K. Gupta, Proceedings of the DAE-BRNS Symp. on Nucl. Phys. **60**, p.480 (2015).

[26] Decay analysis of compound nucleus ^{217}At* formed via neutron-rich exotic ^{9}Li on ^{208}Pb and its synthesis within the dynamical cluster-decay model., Arshdeep Kaur, Bivash R. Behera, and Raj K. Gupta (submitted, Phys. Rev. C)

[27] S. Chopra, M. Bansal, M. K. Sharma, and R. K. Gupta, Phys. Rev. C **88**, 014615 (2013).

[28] Sahila Chopra, Hemdeep, Arshdeep Kaur, and Raj K. Gupta Phys. Rev. C **93**,024603 (2016).

[29] A. Kaur, S. Chopra, and R. K. Gupta, Phys. Rev. C **89**, 034602 (2014).

[30] M. K. Sharma, S. Kanwar, G. Sawhney, R. K. Gupta, and W. Greiner, J. Phys. G: Nucl. Part. Phys. **38**, 055104 (2011).

[31] S. Kanwar, M. K. Sharma, B. B. Singh, R. K. Gupta, and W. Greiner Int. J. Mod. Phys. E **18**, 1453 (2009).

[32] S. Kumar and R. K. Gupta, Phys. Rev. C **55**, 218 (1997).

[33] N. J. Davidson, S. S. Hsiao, J. Markram, H. G. Miller, and Y. Tzeng, Nucl. Phys. A **570**, 61c (1994).

[34] G. Royer and J. Mignen, J. Phys. G: Nucl. Part. Phys. **18**, 1781 (1992), and earlier references therein.

[35] S. Shlomo and J.B. Natowiz, Phys. Rev. **C44**, 2878 (1991).

[36] C. Y. Wong, Phys. Rev. Lett. **31**, 766 (1973).

[37] D. L. Hill and J. A. Wheeler, Phys. Rev. **89**, 1102 (1953); T D Thomas, Phys. Rev. **116**, 703 (1959).

[38] D. J. Hinde, M. Dasgupta, J. R. Leigh, J. C. Mein, C. R.Morton, J. O. Newton, and H. Timmers, Phys. Rev. C **53**, 1290 (1996).

[39] J. C. Mein, D. J. Hinde, M. Dasgupta, J. R. Leigh, J. O. Newton, and H. Timmers, Phys. Rev. C **55**, R995 (1997).

[40] H. C. Britt and A. R. Quinton, Phys. Rev. **124**, 877 (1961).

[41] T. Inamura, A. C. Kahler, D. R. Zolnowski, U. Garg, T. T. Sugihara, and M. Wakai, Phys. Rev. C **32**, 1539 (1985).

[42] A. Kaur, S. Chopra and R. K. Gupta, Phys. Rev. C **90**, 024619 (2014).

[43] N. Bohr, Nature (London) **137**, 344 (1936).

[44] S. Chopra , A. Kaur, and R. K. Gupta, Phys. Rev. C **91**, 034613 (2015).

[45] R. Bass, Nucl. Phys. A **231**, 45 (1974).

[46] R. Bass, *Nuclear Reactions with Heavy Ions* (Springer-Verleg, Berlin, 1980).

[47] J. Blocki, J. Randrup, W.J. Swiatecki, and C.F. Tsang, Ann. Phys. (N.Y.) **105**, 427 (1977).

[48] K. A. Brueckner, J. R. Buchler, and M. Kelley, Phys. Rev. **173**, 944 (1968).

[49] D. M. Brink and Fl. Stancu, Nucl. Phys. A **270**, 236 (1976).

[50] D. Vautherin and D. M. Brink, Phys. Rev. C **5**, 626 (1972).

[51] T. H. R. Skyrme, Phil. Mag. **1**, 1043 (1956); Nucl. Phys. **9**, 615 (1959).

[52] B. Grammoticos and A. Voros, Ann. Phys. **123**, 359 (1979).

[53] B. Grammoticos and A. Voros, Ann. Phys. **129**, 153 (1980).

[54] R. K. Puri and R. K. Gupta, Phys. Rev. C **51**, 1568 (1995).

[55] M. K. Sharma, H. Kumar, R. K. Puri, and R. K. Gupta, Phys. Rev. C **56**, 1175 (1997).

[56] M. K. Sharma, R. K. Puri, and R. K. Gupta, Eur. Phys. J. A **2**, 69 (1998).

[57] R. Arora, R. K. Puri, and R. K. Gupta, Eur. Phys. J. A **8**, 103 (2000).

[58] R. K. Gupta, D. Singh, and W. Greiner, Phys. Rev. C **75**, 024603 (2007).

[59] M. Brack, C. Guet, and H. -B. Hakansson, Phys. Rep. **123**, 275 (1985).

[60] J. Bartel and K. Bencheikh, Eur. Phys. J. A **14**, 179 (2002).

[61] M. Dutra *et al.*, Phys. Rev. C **85**, 035201 (2012).

[62] B. K. Agrawal, S. Shlomo, and V. K. Au, Phys. Rev. C **72**, 014310 (2005).

[63] B. K. Agrawal, S. K. Dhiman, and R. Kumar, Phys. Rev. C **73**, 034319 (2006).

[64] G.-Q. Li, J. Phys. G: Nucl. Part. Phys. **17**, 1 (1991).

[65] R. Kumar, M. K. Sharma, and R. K. Gupta, Nucl. Phys. A **870**, 42 (2011).

[66] V. Yu. Denisov and W. Nörenberg, Eur. Phys. J. A **15**, 375 (2002).

[67] A. Dobrowolski, K. Pomorski, and J. Bartel, Nucl. Phys. A **729**, 713 (2003).

[68] K. Hagino *et al.*, Phys. Rev. C **55**, 276 (1997).

[69] K. Hagino, A. Vitturi, C. H. Dasso and S. M. Lenzi, Phys. Rev. C **61**, 037602 (2002).

[70] S. Kumar, D. Bir, and R. K. Gupta, Phys. Rev. C **51**, 1762 (1995).

[71] Raj K. Gupta, *et al.*, J. Phys. G: Nucl. Part. Phys. **32**,345 (2006)

Chapter 2

Methodology

2.1 Introduction

In this work, we study the nuclear structure and orientation effects in the decay of hot and rotating compound system. There are a number of emission processes from the ground states of parent nuclei and also from the excited compound nuclei (CN) formed in low energy heavy ion nuclear reactions. The aim here is to study the nuclear reaction dynamics, especially the dis-integration of the excited CN using the dynamical cluster-decay model (DCM) [1] - [16]. In DCM, the deformation and orientation effects of reaction partners and the decay products are explicitly included along with the temperature and angular momentum contributions. The ground state cluster/ spontaneous decay of radioactive nuclei have also been studied within the preformed cluster model (PCM) [17] - [22], including deformation and orientation effects of the clusters as well as of daughter nuclei. For the decay of excited CN, the DCM [1] - [16], a reformulation of the PCM for the ground state decay, has an advantage that it gives the relative probability of all the channels through which an excited CN can decay.

Both PCM and DCM originate from the Quantum Mechanical Fragmentation Theory, (QMFT) [23] - [36] (Section 2.2), which is based on collective co-ordinate picture. QMFT is the only theory, given prior to experiments, which brings out the

applicability of quantum concept of probability and the role of shell effects for fusion reactants and also for the other related processes of fission and cluster radioactivity. In QMFT the potential is calculated using the macro-microscopic method of Strutinsky [37]. This average two body potential is successful in explaining the cold and hot fusion reaction dynamics. QMFT is based on the fact that the fragments are pre-born prior to the decay of the CN. The quantum mechanical preformation probability P_0 of the decaying fragments or clusters formed in the mother nucleus can be calculated by solving a stationary Schrödinger equation in mass fragmentation coordinate. This preformation probability allows us to make significant remarks on the nuclear structure of CN and its decaying fragments. Once the clusters are formed, their penetration probability P across the interaction barrier can be calculated by using the WKB approximation.

To understand the formation and decay of nuclear systems, the precise and systematic understanding of ion-ion interaction between the colliding nuclei is required. In this thesis, we present the calculations using two kinds of nuclear potentials; one using proximity theorem and other using energy density formalism. With in energy density formalism, two different functional forms of Hamiltonian density are available, one due to Bruckner et al. [38–41] and other due to Vautherin and Brink [42] which uses the density dependent Skyrme interactions [43]. Here, the later one is used due to an advantage that it is capable of explaining and reproducing the ground state properties of a large number of nuclei. The energy density formalism is used with Skyrme interaction with in an extended Thomas-Fermi (ETF) approximations for the kinetic energies and spin-orbit terms, upto second order in the spatial derivatives with nucleon density, calculated from two parameter Fermi density. The details of ETF method of SEDF are given in Section 2.5. The preformed cluster model (PCM) for ground-state decay, and its extension to the dynamical cluster-decay model for decay of excited CN are described in Sections 2.3 and 2.4, respectively. Finally, the Wong formula for ℓ=0 and its extention to include all contributing ℓ-values are described in Section 2.5 for estimating fusion cross-section.

2.2 Quantum Mechanical Fragmentation Theory

QMFT [23] - [36] is a unified description of two body channels in both fusion and fission processes. The quantities essential for the description of nuclear reaction dynamics are the potential energy surfaces along with the mass parameters defining the kinetic energy of the system. The potential energy alone can determine the static properties of nuclear system. In QMFT, the quantum mechanical concept of probability is used to investigate the role of shell effects in fusion, fission and cluster radioactivity. QMFT is worked out in terms of the following collective variables:

(i) Relative separation coordinate R between the two nuclei or, in general, two fragments (or, equivalently, length parameter $\lambda = L/2R_0$, with L as length of the nucleus and R_0 as the radius of an equivalent spherical nucleus).

(ii) The deformations co-ordinates $\beta_{\lambda i}$ (λ=2,3.4... and i=1,2) of the colliding nuclei.

(iii) The orientation degrees of freedom θ_i, i=1,2 of deformed nuclei (see Fig. 2.1).

(iv) Azimuthal angle Φ between the principal planes of two colliding nuclei.

(v) Neck parameter ε, defined by the ratio $\varepsilon = E_0/E'$ for interaction region ($R < (R_1 + R_2)$, R_i i=1,2, the radii of two nuclei). Here E_0 is the actual height of the barrier and E' is the fixed barrier of two center oscillator. $\epsilon = 0$ represents a broad neck formation, whereas $\epsilon = 1$ gives that the neck is fully squeezed in, corresponding to the asymptotic region ($R > R_1 + R_2$).

(vi) Mass and charge fragmentation co-ordinates [23, 24, 35], which for two body channels, i.e., for separated nuclei/ fragments are defined by the mass and charge-asymmetry coordinates as

$$\eta = \frac{A_1 - A_2}{A}; \qquad \eta_Z = \frac{Z_1 - Z_2}{Z} \tag{2.1}$$

Similarly,

$$\eta_N = \frac{N_1 - N_2}{N}, \tag{2.2}$$

the neutron asymmetry coordinate [24], can also be used, but it is sufficient to treat only two of them as dynamical co-ordinates since they are related as

$$\eta = \frac{Z}{A}\eta_Z + \frac{N}{A}\eta_N. \tag{2.3}$$

Here $A = A_1 + A_2$, $Z = Z_1 + Z_2$ and $N = N_1 + N_2$. A_i, Z_i and N_i $(i = 1, 2)$ are, respectively, the mass number, charge number and neutron number of two fragments. A, Z and N are, respectively, the mass number, charge number and neutron number of CN. The limiting values of η are $0 \leq |\eta| \leq 1$ which allows a unified description of a few-nucleon, multi-nucleon (a cluster) transfer, large-mass transfer, the complete fusion ($|\eta| = 1$) of nuclei and the symmetric ($\eta = 0$), asymmetric and super-asymmetric fission of a compound nucleus. The η_Z coordinate gives the associated charge distribution effects.

In terms of these collective coordinates and their velocities, the collective Hamiltonian can be written as:

$$H = K(\mathbf{R}, \beta, \varepsilon, \eta, \eta_Z; \dot{\mathbf{R}}, \dot{\beta}, \dot{\varepsilon}, \dot{\eta}, \dot{\eta}_Z) + V(\mathbf{R}, \beta, \varepsilon, \eta, \eta_Z). \tag{2.4}$$

Here, β stands for $\beta_{\lambda 1}$ and $\beta_{\lambda 2}$; λ=2,3,4 and so on, K refers to the Kinetic energy and V gives the collective potential energy.

For the compound nucleus formation, the neck parameter ϵ is assumed to be zero, since once the neck formation starts between two colliding nuclei, then fission phenomenon can never be stopped, i.e., excited CN will proceed towards the disintegration process. For the fixed ϵ and β, and for the potential $V(\eta, \eta_Z, R)$ minimized in η_Z co-ordinate, Schrödinger wave equation in terms of mass asymmetry parameter η and relative separation R co-ordinates can be written as:

$$H(\eta, R)\psi(\eta, R) = E(\eta, R)\psi(\eta, R) \tag{2.5}$$

with the Hamiltonian,

$$H(\eta, R) = K(\eta) + K(R) + K(\eta, R) + V(\eta) + V(R) + V(\eta, R) \tag{2.6}$$

The mass parameters B_{ij}, defining K in the above Eqs. (2.4) and (2.6) are either the consistently calculated cranking masses using the Asymmetric Two-Center Shell Model ($ATCSM$) or classical hydrodynamical masses, which are shown to have good agreement with the microscopic cranking calculations. The coupling term of the kinetic energy $K(\eta, R)$, proportional to $\frac{\partial^2}{\partial\eta\partial R}$, is neglected here, because the coupled cranking masses are very small [23, 24], ($\mathrm{B}_{R\eta} \ll (B_{RR}B_{\eta\eta})^{1/2}$ and $\mathrm{B}_{R\eta_Z} \ll (B_{RR}B_{\eta_Z\eta_Z})^{1/2}$). Same is true for the coupling term of potential energy $V(\eta, R)$.

Therefore, in a decoupled approximation [36], the Schrödinger equation (2.5) can be solved using the Hamiltonian given the form:

$$H = -\frac{\hbar^2}{2\sqrt{B_{\eta\eta}}}\frac{\partial}{\partial\eta}\frac{1}{\sqrt{B_{\eta\eta}}}\frac{\partial}{\partial\eta} - \frac{\hbar^2}{2\sqrt{B_{RR}}}\frac{\partial}{\partial R}\frac{1}{\sqrt{B_{RR}}}\frac{\partial}{\partial R} + V(\eta) + V(R). \tag{2.7}$$

For decoupled Hamiltonian (2.7), Schrödinger wave equation (2.5) can be separated for two co-ordinates η and R given as,

$$\left[-\frac{\hbar^2}{2\sqrt{B_{\eta\eta}}}\frac{\partial}{\partial\eta}\frac{1}{\sqrt{B_{\eta\eta}}}\frac{\partial}{\partial\eta} + V(\eta)\right]\psi^{\nu}(\eta) = E^{\nu}_{\eta}\psi^{\nu}(\eta) \tag{2.8}$$

and

$$\left[-\frac{\hbar^2}{2\sqrt{B_{RR}}}\frac{\partial}{\partial R}\frac{1}{\sqrt{B_{RR}}}\frac{\partial}{\partial R} + V(R)\right]\psi^{\nu}(R) = E^{\nu}_{R}\psi^{\nu}(R) \tag{2.9}$$

with

$$\psi(\eta, R) = \psi(\eta)\psi(R) \tag{2.10}$$

and

$$E = E_\eta + E_R \tag{2.11}$$

The states $\psi^\nu(\eta)$ are the vibrational states in potential $V(\eta)$ and are labelled by quantum numbers $\nu = 0, 1, 2$, etc. In following subsections, we first discuss various terms of Schrödinger wave equations (2.8) and (2.9) and then give the solution of Eq. (2.8) for the determination of preformation probability $P_0 \propto |\psi^0(\eta)|^2$.

2.2.1 The Scattering Potential $V(R)$

For a fixed η, i.e., for a given target projectile (A_1, A_2) combination, the scattering potential $V(R)$ in Eq. (2.9) is defined as the sum of temperature-, deformations- and orientations-dependent Coulomb, proximity and angular momentum-dependent potentials, i.e.,

$$\begin{aligned} V(R,\ell,T) &= V_c(R, Z_i, \beta_{\lambda i}, \theta_i, \Phi, T) + V_p(R, A_i, \beta_{\lambda i}, \theta_i, \Phi, T) \\ &+ V_\ell(R, A_i, \beta_{\lambda i}, \theta_i, \Phi, T) \end{aligned} \tag{2.12}$$

For co-planar nuclei, i.e., nuclei lying in same plane, (Fig. 2.1) Φ=0^0, and for spherical-plus-deformed nuclear collisions, only one orientation angle θ is enough, referring to the rotationally-symmetric deformed nucleus.

2.2.2 The Fragmentation potential $V(\eta)$

The temperature dependent collective potential energy, or the fragmentation potential $V(\eta, R, T)$, is calculated as,

$$\begin{aligned} V(\eta,R,\ell,T) &= -\sum_{i=1}^{2} B_i(A_i, Z_i, \beta_{\lambda i}, T) + V_c(R, Z_i, \beta_{\lambda i}, \theta_i, \Phi, T) \\ &+ V_p(R, A_i, \beta_{\lambda i}, \theta_i, \Phi, T) + V_\ell(R, A_i, \beta_{\lambda i}, \theta_i, \Phi, T) \end{aligned} \tag{2.13}$$

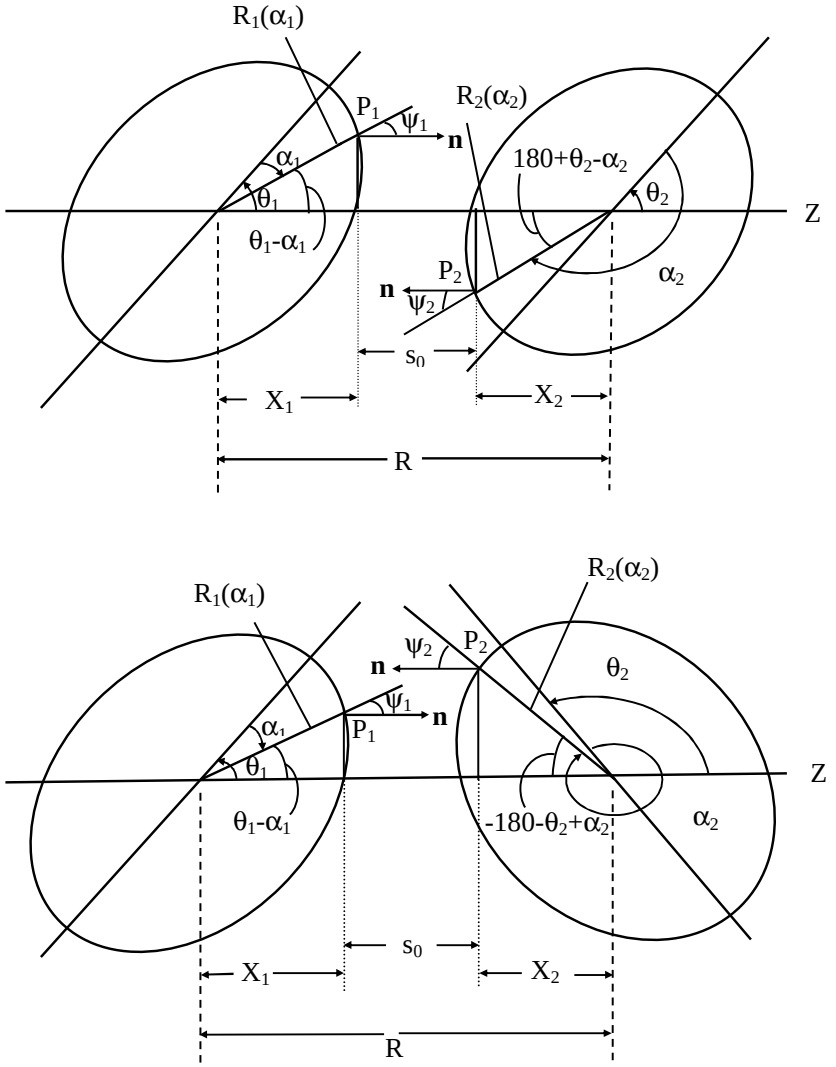

Figure 2.1: Schematic configurations of two (equal/ unequal) axially symmetric deformed, oriented nuclei, lying in the same plane (co-planar nuclei) and for various θ_1 and θ_2 values in the range 0^0 to 180^0.

$V(\eta)$, appearing in Eq. (2.8), is calculated at a fixed distance $R = R_1 + R_2 + \Delta R$ for consideration of deformed and oriented reaction products, with

$$R_i(\alpha_i, T) = R_{0i}(T)[1 + \sum_{\lambda} \beta_{\lambda i} Y_{\lambda}^{(0)}(\alpha_i)], \tag{2.14}$$

and

$$R_{0i}(T) = [1.28A_i^{1/3} - 0.76 + 0.8A_i^{-1/3}] \times (1 + 0.0007T^2). \tag{2.15}$$

Here λ=2,3,4... and α_i is the angle that the radius vector R_i of colliding nuclei makes with the symmetry axis (see Fig. 2.1), measured clockwise.

B_i (i=1,2) appearing in Eq. (2.13), are the binding energies of two nuclei, available from experimental data of Audi-Wapstra [44]. Wherever the experimental B's are not available, theoretical binding energies of Möller *et al.* [45] are used. Note that within the Strutinsky renormalization procedure [37], the binding energies contain both the macroscopic (liquid drop part) and the microscopic (shell correction) part, which allows us to define binding energy B of a nucleus at temperature T as the sum of liquid drop energy $V_{LDM}(T)$ and shell correction $\delta U(T)$, i.e.,

$$B(A_i, Z_i, \beta_{\lambda i}, T) = \sum_{i=1}^{2} V_{LDM}(A_i, Z_i, T) + \sum_{i=1}^{2} \delta U exp\Big(- \frac{T^2}{{T_0}^2}\Big). \tag{2.16}$$

The calculations of fragmentation potential comprises of all the possible decay channels and a number of all such possible decay channels increases with the increasing mass of the parent nucleus. The nuclear temperature T (in MeV) is related to excitation energy E^*_{CN} of CN, through a semi-empirical statistical relation as:

$$E^*_{CN} = E_{c.m.} + Q_{in} = \frac{1}{a} A T^2 - T \qquad (MeV). \tag{2.17}$$

where a = 9-11 depending on the mass of CN. Q_{in} is the entrance channel Q-value given by $Q_{in} = B_1 + B_2 - B_{CN}$ where B's are the binding energies.

2.2.3 Liquid drop energies and their temperature dependence

Temperature dependent liquid drop part of binding energy $V_{LDM}(T)$ is taken from Davidson *et al.* [46], based on semi-empirical mass formula of Seeger [47], as

$$\begin{aligned} V_{LDM}(A,Z,T) &= \alpha(T)A + \beta(T)A^{\frac{2}{3}} + \left(\gamma(T) - \frac{\eta(T)}{A^{\frac{1}{3}}}\right)\left(\frac{I^2 + 2 \mid I \mid}{A}\right) \\ &\quad + \frac{Z^2}{R_0(T)A^{\frac{1}{3}}}\left(1 - \frac{0.7636}{Z^{\frac{2}{3}}} - \frac{2.29}{[R_0(T)A^{\frac{1}{3}}]^2}\right) + \delta(T)\frac{f(Z,A)}{A^{\frac{3}{4}}}, \end{aligned} \tag{2.18}$$

where

$$I = a_a(Z - N), \quad a_a = 1.0,$$

and, respectively, for even-even, even-odd, and odd-odd nuclei,

$$f(Z,A) = (-1, 0, 1).$$

For $T = 0$, Seeger [47] obtained the values of constants, by fitting all even-even nuclei and 488 odd-A nuclei available at that time, as

$$\alpha(0) = -16.11\text{MeV}, \quad \beta(0) = 20.21\text{MeV},$$

$$\gamma(0) = 20.65\text{MeV}, \quad \eta(0) = 48.00\text{MeV},$$

with the pairing energy term from Ref. [48],

$$\delta(0) = 33.0\text{MeV}.$$

As large amount of data are now available on ground-state binding energies, these constants of $V_{LDM}(T = 0)$ needed re-fitting, which was done [1,2,6] to get the exper-

imental binding energies with shell corrections calculated from Myers and Swiatecki [49]. This was first done in [1,2] for the 1995 Audi Wapstra Tables [50] of binding energies, and more recently in [6] for 2003 Tables [44].

For neutron and proton clusters of $x(\geq 1)$ nucleons, we define [51,52] the binding energy of the cluster with x-neutrons as x times the binding energy of one-neutron (equivalently, the mass excess Δm_n=8.0713 MeV),

$$B(A_2 = xn) = x\Delta m_n, \tag{2.19}$$

and the same for proton-clusters, as

$$B(A_2 = xp) = x\Delta m_p - a_c A_2^{5/3} \tag{2.20}$$

with Δm_p=7.2880 MeV, the one-proton mass excess or equivalently the binding energy of single proton. The additional term due to a_c (=0.7053 MeV [49]) is disruptive Coulomb energy ($=-a_c(\frac{Z_2^2}{A_2^{1/3}})$) between x-protons (here $xp = Z_2 = A_2$).

2.2.4 Shell corrections and their temperature dependence

The shell corrections according to the "empirical" formula of Myers and Swiatecki [49], for spherical shapes, are

$$\delta U = C\left[\frac{F(N) + F(Z)}{(A/2)^{\frac{2}{3}}} - cA^{\frac{1}{3}}\right] \tag{2.21}$$

where

$$F(X) = \frac{3}{5}\left(\frac{M_i^{\frac{5}{3}} - M_{i-1}^{\frac{5}{3}}}{M_i - M_{i-1}}\right)(X - M_{i-1}) - \frac{3}{5}\left(X^{\frac{5}{3}} - M_{i-1}^{\frac{5}{3}}\right) \tag{2.22}$$

with $X = N$ or Z, $M_{i-1} < X < M_i$ and M_i as the magic numbers 2, 8, 14 (or 20), 28, 50, 82, 126 and 184 for both neutrons and protons. The value of constant $C = 5.8\ MeV$ and $c = 0.26$. Temperature dependence of shell corrections δU is obtained as given in Eq. (2.16), which decreases exponentially with T_0=1.5 MeV.

At higher excitation energies, shell corrections vanish completely and only liquid drop part of energy is present. The shell corrections play an important role in determining or empirical fitting of nuclear masses, because nuclear masses given by the smooth liquid drop formula show large deviations with respect to the experimental masses. This means that in experimental masses there exists a deep minima at specific neutron and/or proton numbers pointing the presence of shell structure, the so-called magic numbers. This characteristic behavior cannot be reproduced by liquid drop part alone, meaning that the introduction of microscopic shell correction in the mass formula is required. Thus, shell corrections accounts for removal of deviation from liquid drop calculations (uniform distribution of nucleons), and are defined, within Strutinsky [37] method as

$$\delta U = U - \tilde{U} \tag{2.23}$$

where, $U = \sum_\nu E_\nu 2n_\nu$ is the sum over all occupied single particle states and

$$\tilde{U} = 2 \int_{-\infty}^{\tilde{\lambda}} E\tilde{g}(E)dE. \tag{2.24}$$

is the average energy for uniform distribution. Generally, the microscopic shell correction, along with the liquid drop part, give a proper description of binding energy of the nucleus. However, this method does not give proper description for light mass nuclei. The difficulty is the inadequacy of shell model for very light nuclei. Due to this fact, the macro-microscopic calculations of Möller *et al.* [45] are tabulated for $Z \geq 8$ only. Alternatively, one can also use the empirical shell

correction method of Myers-Swiatecki [49] which again is not satisfactory for light nuclei ($Z \leq 16$). Gupta and collaborators have modified this empirical method and obtained a better description of shell corrections for light as well as heavy mass region, i.e, $1 \leq Z \leq 118$ [2].

2.2.5 Proximity Potential for deformed, oriented, co-planar nuclei

When two surfaces approach each other within a small distance of less than $\sim 2fm$, comparable with the surface thickness of interacting nuclei, or when a nucleus is at the verge of dividing into two fragments, then two surfaces actually face each other across a small gap or crevice. In both cases, the surface energy term alone could not give rise to the strong attraction that is observed when two surfaces are brought in close proximity. Such additional attractive forces are called proximity forces and the additional potential due to these forces is called the proximity potential. Blocki *et al.* [53] have reanalyzed and extended a theorem, originally due to Deryagin [54], according to which the force between two gently curved surfaces in close proximity is proportional to the interaction potential per unit area between the two flat surfaces. The original expression of Blocki based on pocket formula was for spherical nuclei, and is given by

$$\begin{aligned} V_P(s_0) &= f(sh., geo.)\phi(s_0) \\ &= 4\pi\bar{R}\gamma b\phi(s_0). \end{aligned} \tag{2.25}$$

$\phi(s_0)$ is the universal function, independent of shapes of nuclei or the geometry of nuclear system, but depends on the minimum separation distance s_0, as

$$\phi(s_0) = \begin{cases} -\frac{1}{2}(s_0 - 2.54)^2 - 0.0852(s_0 - 2.54)^3 \\ -3.437exp(-\frac{s_0}{0.75}) \end{cases} \tag{2.26}$$

respectively, for $s_0 \leq 1.2511$ and $s_0 \geq 1.2511$. Here, s_0 is defined in units of b, i.e. s_0 is s_0/b. This function is defined for negative (the overlap region), zero (touching configuration) and positive values of s_0. For a fixed R, the minimum distance s_0 is defined as

$$s_0 = R - R_1 - R_2 \tag{2.27}$$

where R_i is defined in Eq. (2.14). b is the diffuseness of the nuclear surface given by

$$b = \left[\pi/2\sqrt{3}\ln 9\right]_{t_{10-90}} \tag{2.28}$$

where t_{10-90} is the thickness of the surface in which the density profile changes from 90% to 10%. The value of b$\sim$1 fm. γ is the specific nuclear surface tension given by

$$\gamma = 0.9517\left[1 - 1.7826\left(\frac{N-Z}{A}\right)^2\right] MeVfm^{-2} \tag{2.29}$$

and $\overline{R}$ is the mean curvature radius of reaction partners, characterizing the gap, which for spherical nuclei is given by

$$\overline{R} = \frac{R_1 R_2}{R_1 + R_2} \tag{2.30}$$

The proximity potential for hot deformed nuclei [55] is given as

$$V_p(A_i, \beta_{\lambda i}, \theta_i, T) = 4\pi\bar{R}(T)\gamma b(T)\phi(s_0(T)). \tag{2.31}$$

and surface thickness parameter,

$$b(T) = 0.99(1 + 0.009T^2) \tag{2.32}$$

Fig. 2.1 shows a schematic configuration of two axially symmetric deformed, oriented nuclei, lying in same plane ($\Phi = 0^0$), for various θ_1 and θ_2 values in the range 0^0 to 180^0. θ_i is the angle of orientation, defined as an angle between the symmetry axis and the axis of collision, with it's rotation measured in anti-clockwise direction from the axis of collision. α_i is an angle between the symmetric axis and radius vector $R_i(\alpha_i)$ of colliding nuclei, measured in clockwise direction from symmetry axis of the nucleus.

For axially symmetric shapes, the nuclear radius parameter (to all higher multipole orders λ=2,3,4,....) is given by Eqs. (2.14) and (2.15). In terms of radii of curvature R_{i1} and R_{i2} in the principal planes of curvature of each of the two nuclei (i=1,2) at the points of closest approach (defining s_0 in Fig. 2.1), mean curvature radius $\bar{R}$ for deformed, oriented nuclei is given by

$$\begin{aligned} \frac{1}{\bar{R}^2} &= \frac{1}{R_{11}R_{12}} + \frac{1}{R_{21}R_{22}} + \left[\frac{1}{R_{11}R_{21}} + \frac{1}{R_{12}R_{22}}\right] sin^2\Phi \\ &+ \left[\frac{1}{R_{11}R_{22}} + \frac{1}{R_{21}R_{12}}\right] cos^2\phi. \end{aligned} \tag{2.33}$$

Here, Φ is the azimuthal angle between the principal planes of curvature of two nuclei (for co-planar nuclei Φ=0^0). The four principal radii of curvature are

$$\begin{aligned} R_{i1}(\alpha_i) &= \frac{\left[R_i^2(\alpha_i) + R_i'^2(\alpha_i)\right]^{3/2}}{R_i^2(\alpha_i) + 2R_i'^2(\alpha_i) - R_i(\alpha_i)R_i''(\alpha_i)} \\ R_{i2}(\alpha_i) &= \frac{R_i(\alpha_i)sin\alpha_i}{cos(\pi/2 - \alpha_i - \delta_i)}. \end{aligned} \tag{2.34}$$

where, $R_i'(\alpha_i)$ and $R_i''(\alpha_i)$ are the first and second order derivatives of $R_i(\alpha_i)$ with respect to α_i, respectively. For the derivation of the radius of curvature R_{i1}, see [56]. It follows from Fig. 2.2, and Ref. [57], that $R_{i2} = h/cos\omega_i$, with $h = R_i(\alpha_i)sin\alpha_i$

and $\omega_i = \pi/2 - \alpha_i - \delta_i$. Also, for $\mathbf{n}$ to be a normal vector

$$tan\delta_i = -\frac{R_i'(\alpha_i)}{R_i(\alpha_i)}. \tag{2.35}$$

Note that $R_{i1}(\alpha_i) = R_{i2}(\alpha_i)$, respectively, for $\alpha_1 = 0^0$ or 180^0 and $\alpha_2 = 180^0$ or 360^0. For deformed and oriented nuclei configuration, the minimum distance s_0 (see Fig. 2.1) in Eq. (2.26) is

$$s_0 = R - X_1 - X_2 \tag{2.36}$$

with the projections X_i along Z-axis givn as

$$\begin{aligned} X_1 &= R_1(\alpha_1)cos(\theta_1 - \alpha_1) \\ X_2 &= R_2(\alpha_2)cos(180 + \theta_2 - \alpha_2) \end{aligned} \tag{2.37}$$

and the minimization conditions on s_0,

$$\frac{\partial s_0}{\partial \alpha_1} = \frac{\partial s_0}{\partial \alpha_2} = 0, \tag{2.38}$$

resulting in

$$\begin{aligned} \tan(\theta_1 - \alpha_1) &= -\frac{R_1'(\alpha_1)}{R_1(\alpha_1)} \\ \tan(180 + \theta_2 - \alpha_2) &= -\frac{R_2'(\alpha_2)}{R_2(\alpha_2)}. \end{aligned} \tag{2.39}$$

Comparing Eqs. (2.35) and (2.39), we get

$$\begin{aligned} \delta_1 &= \theta_1 - \alpha_1 \\ \delta_2 &= 180 + \theta_2 - \alpha_2, \end{aligned} \tag{2.40}$$

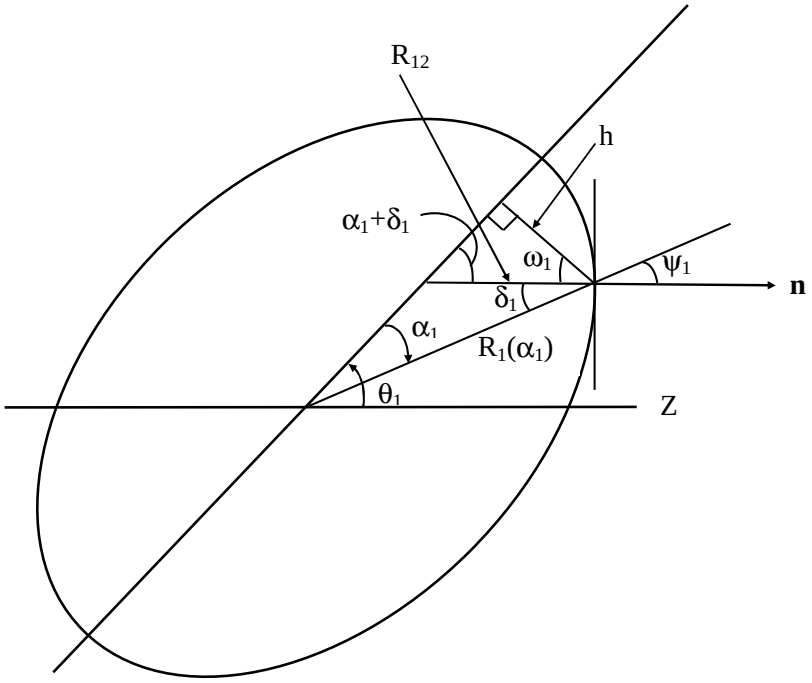

Figure 2.2: An axially symmetric (quadrupole) deformed and oriented nucleus, showing the nuclear radius parameter $R_1(\alpha_1)$ and the geometry associated with the principal radius of curvature $R_{12}(\alpha_1)$.

to be used in Eq. (2.34). Thus, for given θ_1 and θ_2, X_1 and X_2 are obtained for angles α_1 and α_2 satisfying the minimization conditions Eq. (2.39). Note that the conditions Eq. (2.39) refer to perpendiculars (normal vectors) at the points P_1 and P_2. In other words, if the distance s_0 were to be shortest, the perpendicular conditions Eq. (2.39) must be used which would apparently give Eq. (2.37) for X_i.

Eq. (2.31) is valid for zero (touching configuration) and positive values of s_0, but is also used for negative s_0. As two nuclei overlap ($s_0 < 0$), a crevice is formed and, in an adiabatic approximation, the system adjusts its shape parameters such that two colliding nuclei form a single indented body in the form of a single hyperboloid of one sheet with a hyperboloidal crevice [58], as shown in Fig. 2.3(a). For such a necked system, shown in Fig. 2.3(b), following Blocki *et al.* [53], the proximity potential is obtained by Gupta and collaborators [18, 59] as

$$V_P(s_0) = \pi\gamma b^2 \phi_1(s_0 = 0) \frac{(c_1^2 + c_2^2 - 2\epsilon^2)}{(z_1^2 + z_2^2)} \tag{2.41}$$

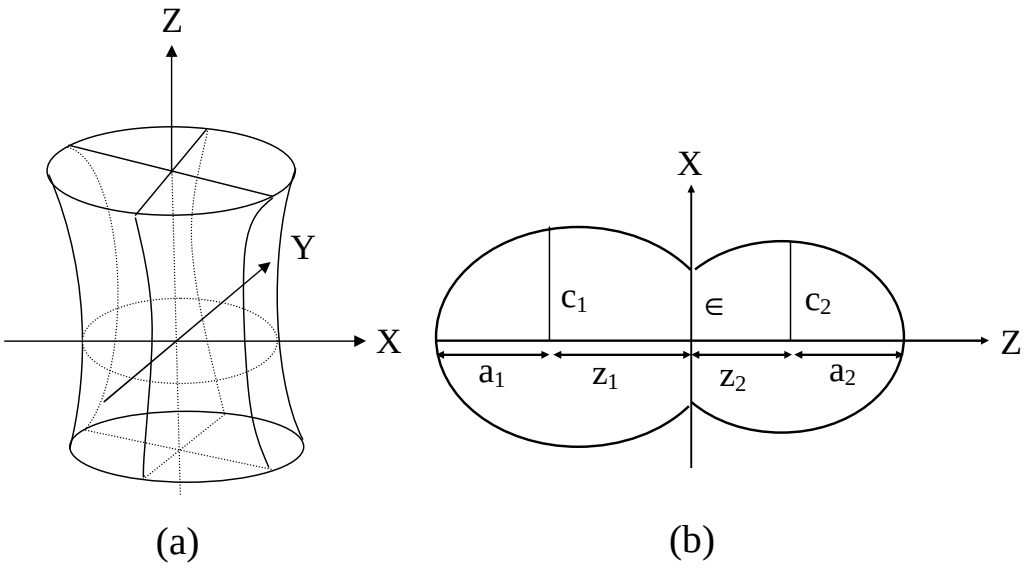

Figure 2.3: (a) Schematic representation of a hyperboloid of revolution in one sheet. (b) Sample nuclear shape formed in two center shell model.

where $\phi_1(s_0 = 0)$=-2.0306 is the first moment of the universal function ϕ at $s_0 = 0$, and c_i, z_i and ϵ are the shape parameters in Fig. 2.3(b). Apparently, for two equal nuclei, $z_1 = z_2$ and $c_1 = c_2$.

2.2.6 The Coulomb potential

Coulomb potential describes the force of repulsion between two interacting nuclei due to their charges. It acts along the line of collision Z-axis. For deformed and oriented interacting nuclei, different authors [55, 60–62] have given different expressions, and the ne due to Ref. [55] is given as:

$$V_c(Z_i, \beta_{\lambda i}, \theta_i, T) = \frac{Z_1 Z_2 e^2}{R(T)} + 3Z_1 Z_2 e^2 \sum_{\lambda, i=1,2} \frac{R_i^\lambda(\alpha_i, T)}{(2\lambda+1)R(T)^{\lambda+1}} Y_\lambda^{(0)}(\theta_i)$$
$$\Big[\beta_{\lambda i} + \frac{4}{7}\beta_{\lambda i}^2 Y_\lambda^{(0)}(\theta_i)\Big], \qquad (2.42)$$

with R_i defined in Eq. (2.14) and $Y_\lambda^{(0)}(\theta_i)$ are the spherical harmonics function.

2.2.7 Rotational Energy due to angular momentum

Rotational motion gives an additional energy due to the angular momentum ℓ, defined as

$$V_\ell(R, A_i, \beta_{\lambda i}, \theta_i, T) = \frac{\hbar^2 \ell(\ell+1)}{2I(T)} \tag{2.43}$$

where I is the moment of inertia. $\mu = \frac{A_1 A_2}{A_1+A_2} m$ is the reduced mass and m is the nucleon mass. $I(T)$=I_{NS}=μR^2, is non-sticking limit of moment of inertia. In the complete sticking limit, the moment of inertia I is given as,

$$I_s(T) = \mu R^2 + \frac{2}{5} A_1 m R_1^2(\alpha_1, T) + \frac{2}{5} A_2 m R_2^2(\alpha_2, T). \tag{2.44}$$

with R_i from Eq. (2.14). For relative separation of interest here, we use the sticking limit. It is relevant to mention here that value of angular momentum extracted experimentally, is based on moment of inertia in non-sticking limit (i.e. $I_{NS} = \mu R^2$) [63]. It means that fragment emission is punctual. In our recent study [10] we find that non-sticking limit is more appropriate for the anisotropy calculations whereas the sticking limit is more appropriate for obtaining the fission cross-sections which consequently results in to a large limiting value of angular momentum.

2.2.8 Classical Hydrodynamical Mass Parameters

The kinetic energy part of the Hamiltonian in Eq. (2.8) enters through the mass parameters. We use here the classical mass parameters of Kröger and Scheid [64]. The model of Kröger and Scheid is based on hydrodynamical flow, as shown in Fig. 2.4. This model gives a simple analytical expression, whose predictions are shown to compare nicely with the microscopic cranking model calculations. For the $B_{\eta\eta}$

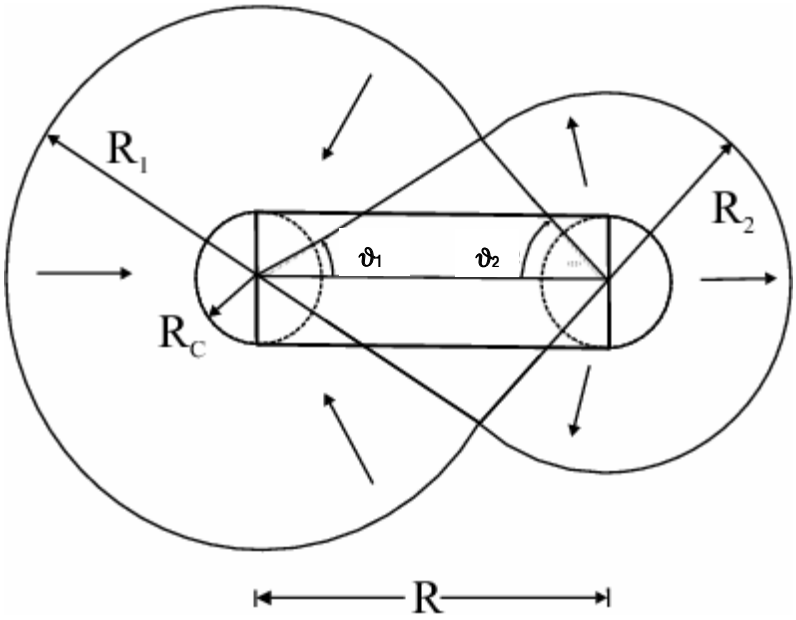

Figure 2.4: The geometry of the classical hydrodynamical model of Kröger and Scheid for calculating the mass parameter $B_{\eta\eta}$.

mass we get,

$$B_{\eta\eta} = \frac{AmR^2}{4}\left[\frac{v_t(1+\gamma)}{v_c(1+\delta^2)} - 1\right] \tag{2.45}$$

with

$$\gamma = \frac{R_c}{2R}\left[\frac{1}{1+\cos\vartheta_1}\left(1-\frac{R_c}{R_1}\right) + \frac{1}{1+\cos\vartheta_2}\left(1-\frac{R_c}{R_2}\right)\right] \tag{2.46}$$

$$\delta = \frac{1}{2R}\left[(1-\cos\vartheta_1)(R_1-R_c) + (1-\cos\vartheta_2)(R_2-R_c)\right] \tag{2.47}$$

$$v_c = \pi R_c^2 R \tag{2.48}$$

ϑ_1 and ϑ_2 and geometry of the model are shown in Fig. 2.4. For $\vartheta_1 = \vartheta_2 = 0$, $\delta = 0$ which corresponds to two touching spheres. $R_c(\neq 0)$ is the radius of a cylinder of length R, having a homogeneous flow in it; whose existence is assumed for the mass transfer between two spherical fragments. We have generalized this expression for

deformed nuclei by using radii R_1 and R_2 for hot deformed nuclei, given by Eq. (2.14).

2.2.9 Solution of the stationary Schrödinger equation and the fragment's preformation probability P_0

Once the Hamiltonian (2.7) is established, Schrödinger equation in mass fragmentation co-ordinate η can be solved. On solving Eq. (2.8) numerically, $|\psi^{\nu}(\eta)|^2$ gives the probability P_0 of finding the mass fragmentation η at a fixed R on the decay path.

$$P_0(A_2) \propto |\psi^{\nu}(A_2)|^2 \tag{2.49}$$

For fission studies like the spontaneous fission and fission through the barrier, the motion in R at saddle point is adiabatically slow as compared to the η motion. Therefore, the potential is minimized in neck ε and deformation coordinates β_1 and β_2 at each R and η values. Starting from the nuclear ground state in spontaneous fission or cluster decay, and to have complete adiabatically, only the lowest vibrational state $\nu = 0$ is occupied. Then, the mass (or charge) distribution yield, proportional to the probability $|\psi^{(0)}(\eta)|^2$ (or $|\psi^{(0)}(\eta_Z)|^2$) of finding a certain mass (or charge) fragmentation η (or η_Z) at a position R on the decay path, when scaled to, say, mass A_2 of one of the fragments ($d\eta = \frac{2}{A}$) is given by:

$$P_0 = |\psi_R^{(0)}(A_2)|^2 \frac{2}{A} \sqrt{B_{\eta\eta}(A_2)}). \tag{2.50}$$

However, if the system is excited or we allow interaction between various degrees of freedom, higher values of ν would also contribute. These enter via the excitation of higher vibrational states, and through the temperature dependent potential V and masses B_{ij}.

The effect of adding temperature on potential V and masses B_{ij} is to reduce the

shell effects in them, resulting finally in the liquid drop potential V_{LDM} and smoothed (averaged) masses $\bar{B}_{ij}$ for the systems to be very hot. Apparently, cold fission means taking both the potential V and masses B_{ij} with full shell effects included in them and hot fission means using the V_{LDM} and smoothed (averaged) masses $\bar{B}_{ij}$. The possible consequence of such excitations are included here by assuming a Boltzmann like occupation of excited states

$$|\psi(\eta)|^2 = \sum_{\nu=0}^{\infty} |\psi^{\nu}(\eta)|^2 \exp\left(-\frac{E_{\eta}^{\nu}}{T}\right) \tag{2.51}$$

Note that we are dealing here with a directly measurable quantity, the mass (or charge) asymmetry, which works dynamically as mass (or charge) transfer coordinate. Thus, the calculated yields $P_0(A_i)$ (or $P_0(Z_i)$) are directly comparable with experiments. The nuclear shape, once minimized in the neck ε and deformation coordinates β_1 and β_2 at a given R ($\approx R_{saddle}$), remains fixed for both the mass and charge distributions of fission fragments.

For the competing, noncompound, quasi-fission (qf) decay channel, the incoming nuclei keep their identity, and hence the preformation factor P_0=1 for η_i in case of qf.

2.2.10 Penetration Probability P

For R-motion, instead of solving the Schrödinger Eq. (2.9), we use the WKB approximation to calculate the penetration probability, P. For each η-value, the potential $V(R)$ for $R \geq R_t$ is calculated by using Eq. (2.12) and for $R < R_t$ it is parameterized simply as a polynomial of degree two in R, so that

$$V(R) = \begin{cases} a_1 R + a_2 R^2 & for \quad R_0 \leq R \leq R_t \\ V_c + V_p + V_\ell & for \quad R \geq R_t \end{cases} \tag{2.52}$$

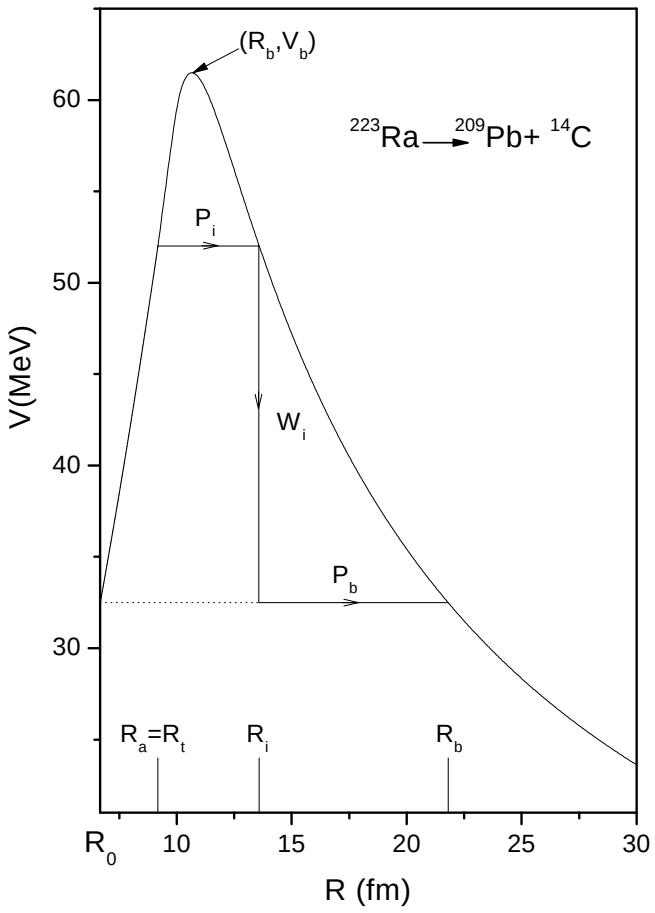

Figure 2.5: The scattering potential for ^{14}C cluster decay of parent nucleus ^{226}Ra, with multipole deformations included up to hexadecapole, and orientation angles θ_i^c of "compact" cold configurations [21].

A typical scattering potential, for ^{223}Ra$\rightarrow^{209}$Pb+^{14}C is shown in Fig. 2.5, calculated by using Eq. (2.12) for the case of ℓ=0. The path of the penetration and the related quantities are also shown. The deformation parameters $\beta_{\lambda i}$ are taken from the tables of Möller *et al.* [45] with "compact" orientations θ_i^c for "cold elongated" configurations. A compact configuration is one occurring with the minimum interaction radius, and is "cold" or "hot" depending on if the barrier is the lowest or highest [55, 65].

The constants a_i $(i = 1, 2)$ occurring in the polynomial, are determined by using the following boundary conditions:

1. At $R = R_0$, $V(R) = Q$

2. At $R = R_t$, $V(R) = V(R_t)$

The first (inner) turning point R_a is chosen at $R_a = R_t + \Delta R$, and the outer turning point is taken at R_b to give the Q-value of the reaction, i.e., $V(R_b) = Q$. This means that the transmission probability P consists of three contributions

1. The penetrability P_i from R_a to R_i,

2. the (inner) de-excitation probability W_i at R_i and

3. the penetrability P_b from R_i to R_b

giving the penetration probability as

$$P = P_i W_i P_b. \tag{2.53}$$

The shifting of first turning point from R_t to R_0 gives the penetrability calculations similar to Shi and Swiatecki [66] for spherical nuclei, which is known not to fit the experimental data without the adjustment of assault frequency.

Following the excitation model of M. Greiner and W. Scheid [67], de-excitation probability W_i is given as

$$W_i = \exp(-bE_i) \tag{2.54}$$

This means that the de-excitation process is restricted to only a single transition. If the parameter b were allowed to depend on R_i, it should then become a process of multiple de-excitation and proceed as step-like process. For a heavy cluster decay into the excited states of daughter nucleus, $b = 0$ is assumed [67], which means

$$W_i = 1, \tag{2.55}$$

so that,

$$P = P_i P_b, \tag{2.56}$$

where P_i and P_b are calculated by using WKB approximation, as

$$P_i = \exp\left[-\frac{2}{\hbar}\int_{R_a}^{R_i}\{2\mu[V(R)-V(R_i)]\}^{1/2}dR\right] \tag{2.57}$$

and

$$P_b = \exp\left[-\frac{2}{\hbar}\int_{R_i}^{R_b}\{2\mu[V(R)-Q]\}^{1/2}dR\right]. \tag{2.58}$$

Here R_a and R_b are, respectively, the first and second turning points. This means that the tunneling begins at $R = R_a$ and terminates at $R = R_b$, with $V(R_b) = Q$-value for ground state decay. The integrals of the Eqs. (2.57) and (2.58) are solved analytically by parameterizing the above calculated potential $V(R)$, as follows:

$$V(R) = \begin{cases} a_1R + a_2R^2, & R_0 \le R \le R_t, \\ V(R_t) + m(R-R_t), & R_t \le R \le R_m, \\ V_B - \frac{1}{2}k(R-R_B)^2, & R_m \le R \le R_h, \\ V(R_h) - c_1\frac{R-R_h}{R}, & R_h \le R \le R_i, \\ V(R_i) - c_2\frac{R-R_i}{R}, & R_i \le R \le R_b, \end{cases} \tag{2.59}$$

For a polynomial of degree higher than two, analytical solutions of WKB integrals could not be obtained. The above equation is true for any inner turning point and hence R_t could be chosen empirically at any point on the polynomial part, as was shown in [18]. Eq. (2.59) means that, the first part of the potential from R_0 to R_t (or R_{emp}) is a polynomial of degree two in R, the second part from R_t to R_m is a straight line of slope 'm', the top part between R_m and R_h being an inverted harmonic oscillator and the rest from R_h to R_i and R_i to R_b are the Coulomb potentials of the type $1/R$. Finally, V_B and R_B give the height and position of the

barrier. The analytical solution for the integrals are obtained as

$$\int_{R_b}^{R_t} V(R)dR = \int_{R_m}^{R_t} V(R)dR + \int_{R_h}^{R_m} V(R)dR + \int_{R_i}^{R_h} V(R)dR + \int_{R_b}^{R_i} V(R)dR \quad (2.60)$$

For different components of Eq.(2.56), we have

$$\begin{aligned} P_i &= exp[-\frac{2}{\hbar}\sqrt{2\mu}\{\frac{\sqrt{a_2}}{2}[t_1(t_1^2 - L^2)^{\frac{1}{2}} - t_2(t_2^2 - L^2)^{\frac{1}{2}} \\ &\quad -L^2(cosh^{-1}(\frac{t_1}{L}) - cosh^{-1}(\frac{t_2}{L})] \\ &\quad +\frac{2}{3}(\frac{R_m - R_t}{V(R_m) - V(R_t)})[(V(R_m) - V(R_i))^{\frac{3}{2}} - (V(R_t) - V(R_i))^{\frac{3}{2}}] \\ &\quad -\frac{1}{\sqrt{2k}}[V_B - V(R_i)][\Theta_2 - \frac{1}{2}sin2\Theta_2 - \Theta_1 + \frac{1}{2}sin2\Theta_1] \\ &\quad +\sqrt{C_1 R_h R_i}[\Theta_3 - \frac{1}{2}sin2\Theta_3]\}] \end{aligned} \quad (2.61)$$

with

$$a_1 = \frac{R_0(Q - V(R_t))}{R_t(R_t - R_0)}, a_2 = -\frac{a_1}{R_0}, t_1 = R_t - \frac{1}{2}R_0, t_2 = R_{emp} - \frac{1}{2}R_0$$

$$L^2 = \frac{1}{4}R_0^2 + R_t(R_t - R_0)\left[\frac{Q - V(R_i)}{Q - V(R_t)}\right]$$

$$\Theta_1 = \cos^{-1}\frac{R_m - R_B}{\sqrt{\alpha}_2}, \Theta_2 = \cos^{-1}\frac{R_h - R_B}{\sqrt{\alpha}_2}, \Theta_3 = \tan^{-1}\left(\frac{R_i - R_h}{R_h}\right)^{1/2}$$

$$\alpha_2 = \frac{2}{k}[V_B - V(R_i)]$$

$$k = \frac{2\{[(V_B - V(R_m)]^{1/2} + [V_B - V(R_h)]^{1/2}\}^2}{(R_m - R_h)^2}, C_1 = R_i\frac{(V(R_h) - V(R_i))}{R_i - R_h}$$

and

$$P_b = \exp\left[-\frac{2}{h}\sqrt{2\mu}\sqrt{C_2 R_i R_b}\left\{\Theta_4 - \frac{1}{2}\sin 2\Theta_4\right\}\right] \tag{2.62}$$

with

$$\Theta_4 = tan^{-1}\left[\frac{R_b - R_i}{R_i}\right]^{1/2},$$

$$C_2 = \frac{R_b[V(R_i) - V(R_b)]}{R_b - R_i}.$$

Substituting these values in Eqs. (2.61) and (2.62) we get P_i and P_b. Further substituting P_i and P_b in Eq. (2.56) we get the probability of penetration or the tunneling probability P.

2.2.11 Assault Frequency ν_0

For the cluster decay studies (the following section), another quantity of interest is the assault frequency ν_0, defined as,

$$\nu_0 = \frac{v}{R_0} = \frac{(2E_2/\mu)^{1/2}}{R_0}, \tag{2.63}$$

where R_0 is the radius of parent nucleus and $E_2 = \frac{1}{2}\mu v^2$ is the kinetic energy of the emitted cluster. Since both the emitted cluster and the daughter nucleus are produced in the ground state, the entire positive Q-value is the total kinetic energy ($Q = E_1 + E_2$) available for the decay process, which is shared between two fragments, such that for the emitted cluster,

$$E_2 = \frac{A_1}{A}Q \tag{2.64}$$

and, $E_1 = Q - E_2$ is the recoil energy of the daughter nucleus.

In the following section, we use Eqs. (2.50), (2.56) and (2.63) for P_0, P and ν_0 for calculating the decay constant and the corresponding half-life for the emitted fragments treated as clusters.

2.3 The Preformed Cluster Model for ground state decay of nuclei

Many theoretical models are advanced [17, 66, 68–71] to understand the process of exotic cluster decay in terms of nuclear α-decay or nuclear fission. These models are mainly categorized into two groups: i) Unified fission models (UFM), and ii) Preformed cluster models (PCM). In UFM, the cluster decay is dealt simply as a barrier penetration problem, whereas in PCM, it is considered to happen in two steps as mentioned in the Introduction of this chapter. The Preformed Cluster Model [17] - [22] has been developed by adopting mainly the Gamow's theory of α-decay. Here, instead of a square well potential, a more realistic nuclear potential, the nuclear proximity potential, is used and also a preformation probability P_0 is associated with each of the emitted cluster. In Gamow's theory of α-decay, P_0=1 for α-decay, since only α-cluster is considered to be emitted. In PCM, P_0 is different for every cluster and it decreases with the increase in size of cluster. It is relevant to mention here that in PCM P_0 for all the possible clusters can be obtained, whereas in the other model, like that of Blendowske *et al.* [69, 72], the P_0 are calculated for the cluster mass of up to $A = 28$ only.

The decay constant in the PCM is defined as,

$$\lambda = \nu_0 P P_0. \tag{2.65}$$

with the corresponding half-life given as: $T_{\frac{1}{2}} = \frac{ln2}{\lambda}$.

Here ν_0 is the impinging frequency with which the cluster hits the barrier, P, the penetration probability, gives the probability of penetration of the barrier formed by outgoing deformed and oriented fragments and P_0, the preformation probability of the cluster giving the probability of the formation of the cluster within the mother nucleus, which is also shown to carry the effects of deformations and orientations of outgoing fragments. For a pure Coulomb potential and $P_0 = 1$, the above Eq. (2.65) will give the Gamow factor 'λ_G'. Thus, the clusters in PCM are considered to be preformed with probability P_0, at a relative separation measured in terms of co-ordinate R before the penetration of potential barrier.

More recently, the T-dependence is also included in PCM [73], and the PCM(T) is applied to α-decay chains of recoiling (T$\neq$0, ℓ=0) superheavy nucleus formed after x-neutrons emission from excited CN.

2.4 The Dynamical Cluster-decay Model (DCM) for hot and rotating compound nucleus

The dynamical cluster-decay model (DCM) [1] - [16] for the decay of a hot and rotating compound nucleus (i.e., angular momentum $\ell\neq0$ and temperature $T\neq0$) is a reformulation of the preformed cluster model (PCM) [17] - [22] for ground-state (ℓ=0, T=0) decay of a nucleus in cluster radioactivity (CR) and related phenomena. So, like PCM, the DCM is also based on the dynamical (or quantum mechanical) fragmentation theory of cold phenomenon in heavy ion reactions and fission dynamics. Besides the temperature and angular momentum effects in the decay of excited CN, the deformation and orientation effects of the decay products are also taken care in DCM. The co-ordinates η and R of the fragmentation theory in DCM, characterize, respectively,

(i) the nucleon-division (or -exchange) between outgoing fragments, and

(ii) the transfer of kinetic energy of incident channel ($E_{c.m.}$) to internal excitation

(total excitation or total kinetic energy, TXE or TKE) of the outgoing channel, since the fixed $R = R_a$, at which the process is calculated, depends on temperature T as well as on η, i.e., $R(T, \eta)$. This energy transfer process follows the relation

$$E^*_{CN} + Q_{out}(T) = TKE(T) + TXE(T). \tag{2.66}$$

The CN excitation energy E^*_{CN} is related to temperature T (in MeV) via Eq.(2.17).

Using the decoupled approximation to R- and η-motions, DCM defines the decay cross-section, in terms of partial waves, as [1] - [16]

$$\sigma = \sum_{\ell=0}^{\ell_{max}} \sigma_\ell = \frac{\pi}{k^2} \sum_{\ell=0}^{\ell_{max}} (2\ell+1) P_0 P; \qquad k = \sqrt{\frac{2\mu E_{c.m.}}{\hbar^2}} \tag{2.67}$$

where, P_0, the preformation probability, refers to η-motion and P, the penetrability, to R-motion, discussed in Sec. 2.2.9 and Sec. 2.2.10, respectively. Apparently, for ℓ=0 (s-wave) $\sigma_0 = \frac{\pi}{k^2} P_0 P$, which is an equivalent of decay constant $\lambda = \nu_0 P_0 P$ (or decay half-life $\mathrm{T}_{1/2} = ln2/\lambda$) with ν_0 as the barrier assault frequency. In other words, σ_0 and λ differ through a constant only. Thus, like in PCM, here the complex fragments (both light and heavy fragments) are treated as the dynamical collective mass motion of *preformed clusters or fragments* through the barrier. The structure information of the CN enters the model via the preformation probabilities P_0 (also known as the spectroscopic factors) of the fragments given by the solution of stationary Schrödinger equation in η (see Eq. (2.8)), at a fixed R=R_a, the first turning point of the penetration path shown in Fig. 2.5.

For the decay of a hot CN, we use the postulate for the first turning point

$$R_a(T) = R_t + \Delta R(\eta, T) \tag{2.68}$$

where

$$R_t = R_1(\alpha_1, T) + R_2(\alpha_1, T) \tag{2.69}$$

$\Delta R(T)$ is the neck-length parameter that assimilates the neck formation effects. This method of introducing a neck length parameter is similar to that used in both the scission-point [74] and saddle-point [75,76] statistical fission models. The R_i are radius vectors given by Eqs. (2.14) and (2.15).

The corresponding potential $V(R_a)$ acts like an effective Q-value, Q_{eff}, for the decay of the hot CN at temperature T, to two exit-channel fragments observed in *ground state* (T=0), defined by

$$\begin{aligned} Q_{eff}(T) &= B(T) - [B_L(T=0) + B_H(T=0)] \\ &= TKE(T) = V(R_a(T)) \end{aligned} \tag{2.70}$$

with B's as the respective binding energies.

The above defined decay of a hot CN into two cold (T=0) fragments, via Eq. (2.70), could apparently be achieved only by emitting some light particle(s) (LPs), like n, p, α, or γ-rays of energy

$$\begin{aligned} E_x &= B(T) - B(0) = Q_{eff}(T) - Q_{out}(T=0) \\ &= TKE(T) - TKE(T=0), \end{aligned} \tag{2.71}$$

which is zero for the g.s. decay, like for exotic CR. Note that the second equality in Eq. (2.71) is not defined for a negative $Q_{out}(T=0)$ system since the negative TKE(T=0) has no meaning. Apparently, Eq. (2.71) w.r.t (2.70) suggest that the emission of light-particles starts early in the decay process. The exit channel fragments in Eq. (2.70) are then obtained in the ground-state with TKE(T=0), as can

be seen by calculating $E^*_{CN} - E_x$:

$$E^*_{CN} - E_x = |Q_{out}(T)| + TKE(T=0) + TXE(T). \tag{2.72}$$

The excitation energy TXE(T) (not treated here) is used in, the secondary emission of light particles from the fragments which are otherwise in their ground states with TKE(T=0) in the radial motion. Thus, by defining $Q_{eff}(T)$ as in Eq. (2.70), in this model we treat the LP emission at par with the heavy fragments, called intermediate mass fragments ($IMFs$) emission. Thus, in this model a non-statistical dynamical treatment is attempted for not only the emission of $IMFs$ but also of multiple LPs, understood generally as the statistically evaporated particles in a CN emission. It may be reminded here that the statistical model (CN emission) interpretation of $IMFs$ is not as good as it is for the LP production [74] - [79].

In terms of $Q_{eff}(T)$, the second turning R_b satisfies

$$V(R_a, \ell) = V(R_b, \ell) = Q_{eff}(T, \ell) = TKE(T). \tag{2.73}$$

with the ℓ-dependence of R_a defined by

$$V(R_a, \ell) = Q_{eff}(T, \ell = 0), \tag{2.74}$$

i.e., R_a is the same for all ℓ-values, given by the above equation, and that $V(R_a, \ell)$ acts like an effective Q-value, $Q_{eff}(T, \ell)$, given by the total kinetic energy $TKE(T)$. Then, using Eq. (2.73), $R_b(\ell)$ is given by the ℓ-dependent scattering potentials, at fixed T for coplanar nuclei, as in Eq. (2.12), which is normalized to the exit channel binding energy. This means that all energies are measured $w.r.t\ B_L(T)+B_H(T)$. The scattering potential, illustrated in Fig. 3.6 of Chapter 3, for ^{124}Ce$^* \rightarrow ^{116}$Xe+^{8}Be, at different ℓ-values, shows that as the ℓ-value increases, the $Q_{eff}(T)$-value (=TKE(T)) increases and hence $V(R_a, \ell)$ increases, since the decay path for all the ℓ-values begins

at $R = R_a$.

Finally, the ℓ_{max}-value in Eq. (2.68) is the critical ℓ-value, in terms of the bombarding energy $E_{c.m.}$, the reduced mass μ and the first turning point R_a of the entrance channel η_{in}, given by

$$\ell_c = R_a\sqrt{2\mu[E_{c.m.} - V(R_a, \eta_{in}, \ell = 0)]}/\hbar, \tag{2.75}$$

or, alternatively, it could be fixed for the vanishing of fusion barrier of the incoming channel, called ℓ_{fus}, or else the ℓ-value where the light-particle cross-section $\sigma_{LP}(\ell) \to 0$. This, however, could also be taken as a variable parameter [75, 80].

2.4.1 Concept of "barrier lowering" in DCM

The Fusion hindrance phenomenon in the coupled channel calculations (ccc) at extreme sub-barrier energies for the fusion-evaporation cross-sections in reactions such as ^{58}Ni+^{58}Ni, ^{64}Ni+^{64}Ni and ^{64}Ni+^{100}Mo, and capture (equivalently, quasi-fission) cross-sections for ^{48}Ca+^{238}U, ^{244}Pu and ^{248}Cm reactions are one of the topic of current research in Nuclear Physics. DCM also supports the only acceptable explanation for the above said hindrance phenomenon in ccc, in terms of the 'barrier modification' at sub-barrier energies [81] since the property of 'lowering of barrier' (without modifying the depth of potential pocket) at sub-barrier energies arises in DCM in a simple way via its fitting of the neck-length parameter. The choice of parameter R_a (equivalently, ΔR) for a best fit to data corresponds to the effects of "barrier lowering" in it for each decay channel, defined for each ℓ as the difference between $V_B(\ell)$ and $V(R_a, \ell)$, the barrier height and the actually used barrier, as

$$\Delta V_B(\ell) = V(R_a, \ell) - V_B(\ell). \tag{2.76}$$

Note, ΔV_B for each ℓ is defined as a negative quantity as the actual barrier height is effectively lowered, as is also illustrated in Fig. 3.6 of Chapter 3 for different ℓ values.

2.4.2 Compound Nucleus fusion (or formation) probability P_{CN} and Survival Probability P_{surv}

Recently, using the dynamical cluster-decay model (DCM), we have estimated the compound nucleus (CN) fusion/ formation probability P_{CN} [82], and the CN survival probability P_{surv} [83] against fission, i.e., the probability of fused system to de-excite by emission of neutrons or light particles (LPs) (equivalently, the evaporation residue ER), rather than fission, each defined as

$$P_{CN} = \frac{\sigma_{CN}}{\sigma_{fusion}} = 1 - \frac{\sigma_{nCN}}{\sigma_{fusion}}, \tag{2.77}$$

and

$$P_{surv} = \frac{\sigma_{ER}}{\sigma_{CN}} = 1 - \frac{\sigma_{ff}}{\sigma_{CN}}, \tag{2.78}$$

where the (total) fusion cross section $\sigma_{fusion} = \sigma_{CN} + \sigma_{nCN}$ with σ_{CN} as the CN formation cross section (given as the sum of evaporation residue ER and fusion-fission (ff) cross sections $\sigma_{CN} = \sigma_{ER} + \sigma_{ff}$), and σ_{nCN} as the non-compound nucleus (nCN) cross section such as the quasi-fission (qf), deep-inelastic collisions/ orbiting (DIC), incomplete fusion (ICF) or pre-equilibrium decay.

Note that all the above mentioned components of fusion cross section σ_{fusion} are individually measurable quantities. In case, the nCN component σ_{nCN} were not measured, it can be estimated empirically from the calculated and measured quantities, as

$$\sigma_{nCN} = \sigma_{fusion}^{Expt.} - \sigma_{fusion}^{Cal.}. \tag{2.79}$$

It may be pointed out that different mass regions of compound nuclei constitute different combinations of these processes (ER, IMFs, ff and nCN) or a single one of them as the dominant mode. P_{CN} takes care of the nCN effects, and P_{surv}, the ff process. In other words, P_{CN}=1 if σ_{nCN}=0, and P_{surv}=1 if σ_{ff}=0. Thus, including the effects of both the nCN and ff processes, Eqs. (2.77) and (2.78) allow us to write the evaporation residue cross section σ_{ER}, in terms of the product $P_{CN}P_{surv}$ [84], as

$$\begin{aligned} \sigma_{ER} &= \sigma_{CN}P_{surv} \\ &= \sigma_{fusion}P_{CN}P_{surv}. \end{aligned} \tag{2.80}$$

2.4.3 Skyrme Energy Density Formalism in semiclassical extended Thomas Fermi approach

For Skyrme Hamiltonian density $H(\vec{r})$, defining the energy expectation value $E(R) = \int H(\vec{r})d\vec{r}$, as already stated in the Introduction, the nuclear interaction potential $V_N(R)$ is the difference of the energy expectation values E of colliding nuclei that are overlapping (i.e., at a finite separation R) and those that are completely separated (i.e., at R =∞) [85–88],

$$\begin{aligned} V_N(R) &= E(R) - E(\infty) \\ &= \int H(\vec{r})d\vec{r} - \left[\int H_1(\vec{r})d\vec{r} + \int H_2(\vec{r})d\vec{r}\right] \end{aligned} \tag{2.81}$$

with the Skyrme Hamiltonian density [42, 88]

$$\begin{aligned} H(\rho,\tau,\vec{J}) &= \frac{\hbar^2}{2m}\tau + \frac{1}{2}t_0\left[(1+\frac{1}{2}x_0)\rho^2 - (x_0+\frac{1}{2})(\rho_n^2+\rho_p^2)\right] \\ &\quad + \frac{1}{2}\sum_{i=1}^{3} t_{3i}\rho^{\alpha_i}\left[(1+\frac{1}{2}x_{3i})\rho^2 - (x_{3i}+\frac{1}{2})(\rho_n^2+\rho_p^2)\right] \end{aligned}$$

$$
\begin{aligned}
&+\frac{1}{4}\left[t_1(1+\frac{1}{2}x_1)+t_2(1+\frac{1}{2}x_2)\right]\rho\tau \\
&-\frac{1}{4}\left[t_1(x_1+\frac{1}{2})-t_2(x_2+\frac{1}{2})\right](\rho_n\tau_n+\rho_p\tau_p) \\
&+\frac{1}{16}\left[3t_1(1+\frac{1}{2}x_1)-t_2(1+\frac{1}{2}x_2)\right](\vec{\nabla}\rho)^2 \\
&-\frac{1}{16}\left[3t_1(x_1+\frac{1}{2})+t_2(x_2+\frac{1}{2})\right] \\
&\times\left[(\vec{\nabla}\rho_n)^2+(\vec{\nabla}\rho_p)^2\right] \\
&-\frac{1}{2}W_0\left[\rho\vec{\nabla}\cdot\vec{J}+\rho_n\vec{\nabla}\cdot\vec{J}_n+\rho_p\vec{\nabla}\cdot\vec{J}_p\right] \\
&-A\left[\frac{1}{16}(t_1x_1+t_2x_2)\vec{J}^2-\frac{1}{16}(t_1-t_2)(\vec{J}_p^2+\vec{J}_n^2)\right]. \qquad (2.82)
\end{aligned}
$$

Here, $H_i(\rho_i,\tau_i,\vec{J}_i)$ is given in terms of the nuclear, kinetic energy and spin-orbit densities, respectively, as $\rho=\rho_n+\rho_p$, $\tau=\tau_n+\tau_p$, and $\vec{J}=\vec{J}_n+\vec{J}_p$, and the Skyrme force parameters [x_j, t_j (j=0,1,2), x_{3i}, t_{3i}, α_i (i=1,2,3), W_0 and A] fitted by different authors to ground state properties of various nuclei. For the old forces [89, 90], like SIII, SIV, SKa, etc., some constants [A, x_{3i}, t_{3i} and α_i (i=2,3)] are zero, and t_{31}=$\frac{1}{6}t_3$, x_{31}=x_3, and α_1=α. Then, for new forces of Agrawal *et al.* [91, 92], like GSkI and KDE0(v1), etc., we have A=1 and six additional constants [two each of x_{3i}, t_{3i}, and α_i], determined by a fit to several properties of the normal and isospin-rich nuclei. For the composite system, densities are added as $\rho=\rho_1+\rho_2$ and, as per frozen density approximation [93],

$$
\begin{aligned}
\tau(\rho) &= \tau_1(\rho_1)+\tau_2(\rho_2), \\
\vec{J}(\rho) &= \vec{J}_1(\rho_1)+\vec{J}_2(\rho_2), \qquad (2.83)
\end{aligned}
$$

with $\rho_i = \rho_{in} + \rho_{ip}$, $\tau_i(\rho_i) = \tau_{in}(\rho_{in}) + \tau_{ip}(\rho_{ip})$, and $\vec{J}_i(\rho_i) = \vec{J}_{in}(\rho_{in}) + \vec{J}_{ip}(\rho_{ip})$. For more details, see, e.g., Ref. [88].

Then, the nucleus-nucleus interaction potential V_N is written as the nuclear proximity potential, following Blocki *et al.* [94] and Gupta *et al.* [86,95], we introduce the slab approximation of semi-infinite nuclear matter with surfaces parallel to $x-y$ plane, moving in z-direction, and separated by distance s having minimum value s_0, and define the proximity interaction potential $V_N(R)$ between two nuclei, separated by $R = R_1 + R_2 + s$, as

$$\begin{aligned} V_N(R) &= 2\pi\bar{R}\int_{s_0}^{\infty} e(s)ds \\ &= 2\pi\bar{R}\int \left\{H(\rho,\tau,\vec{J}) - [H_1(\rho_1,\tau_1,\vec{J}_1) + H_2(\rho_2,\tau_2,\vec{J}_2)]\right\} dz \\ &= 4\pi\bar{R}\gamma b\phi(D) = V_P(R) + V_J(R), \end{aligned} \tag{2.84}$$

where, $V_P(R)$ and $V_J(R)$ are the spin-density independent and spin-density dependent parts of the nuclear interaction potential, and $e(s)$ is the interaction energy per unit area between the flat slabs giving the universal function $\phi(D)$ in terms of a dimensionless variable $D = s/b$ with b as the surface width which is T-dependent. $\phi(D)$ in Eq. (2.84) can be calculated "exactly" or parameterized in terms of exponential and/ or polynomial functions. Since the polynomial functions are obtained for some older forces only [86], here we solve Eq. (6.3) "exactly". For more details, refer to Refs. [86, 87].

In the semiclassical ETF theory, based on SEDF, we have seen that Eq. (2.82) can be written as

$$H(\rho,\tau,\vec{J}) = H(\rho) + H(\vec{J}) \tag{2.85}$$

where $H(\rho)$ and $H(\vec{J})$ refer to terms depending on ρ and/ or τ (τ is also a function of ρ) and $\vec{J}$, respectively. Note that, though $\vec{J}$ is also a function of ρ only but the

terms that depend on $\vec{J}$ behave differently from those dependent on ρ and τ.

The kinetic energy density in ETF method, taken up to second order terms for reasons of being enough for numerical convergence [96], is (q=n or p)

$$\begin{aligned}\tau_q(\vec{r}) &= \frac{3}{5}(3\pi^2)^{2/3}\rho_q^{5/3} + \frac{1}{36}\frac{(\vec{\nabla}\rho_q)^2}{\rho_q} + \frac{1}{3}\Delta\rho_q + \frac{1}{6}\frac{\vec{\nabla}\rho_q\cdot\vec{\nabla}f_q + \rho_q\Delta f_q}{f_q} - \frac{1}{12}\rho_q\left(\frac{\vec{\nabla}f_q}{f_q}\right)^2 \\ &+\frac{1}{2}\rho_q\left(\frac{2m}{\hbar^2}\right)^2\left(\frac{W_0}{2}\frac{\vec{\nabla}(\rho+\rho_q)}{f_q}\right)^2, \end{aligned} \tag{2.86}$$

with f_q as the effective mass form factor,

$$\begin{aligned} f_q(\vec{r}) &= 1 + \frac{2m}{\hbar^2}\frac{1}{4}\left\{t_1(1+\frac{x_1}{2}) + t_2(1+\frac{x_2}{2})\right\}\rho(\vec{r}) \\ &-\frac{2m}{\hbar^2}\frac{1}{4}\left\{t_1(x_1+\frac{1}{2}) - t_2(x_2+\frac{1}{2})\right\}\rho_q(\vec{r}). \end{aligned} \tag{2.87}$$

Note that both τ_q and f_q are each functions of ρ_q and/ or ρ only. The spin $\vec{J}$ is a purely quantal property, and hence has no contribution in the lowest (TF) order. However, at the ETF level, the second order contribution gives

$$\vec{J}_q(\vec{r}) = -\frac{2m}{\hbar^2}\frac{1}{2}W_0\frac{1}{f_q}\rho_q\vec{\nabla}(\rho+\rho_q), \tag{2.88}$$

also a function of ρ_q and/ or ρ alone.

The temperature T-dependence is introduced in the formalism, by using for nuclear density ρ_i of each nucleus, the T-dependent, two-parameter Fermi density (FD) distribution, which for the slab approximation is given by

$$\rho_i(z_i) = \rho_{0i}(T)\left[1+\exp\left(\frac{z_i - R_i(T)}{a_i(T)}\right)\right]^{-1} \quad -\infty \le z \le \infty \tag{2.89}$$

with $z_2 = R - z_1 = [R_1(\alpha_1) + R_2(\alpha_2) + s] - z_1$, and central density

$$\rho_{0i}(T) = \frac{3A_i}{4\pi R_i^3(T)}[1 + \frac{\pi^2 a_i^2(T)}{R_i^2(T)}]^{-1}. \tag{2.90}$$

Then, since $\rho_i = \rho_{n_i} + \rho_{p_i}$, following our earlier work, for nucleon density we define

$$\rho_{n_i} = (N_i/A_i)\rho_i \qquad \text{and} \qquad \rho_{p_i} = (Z_i/A_i)\rho_i, \tag{2.91}$$

with half density radii R_{0i} and surface thickness parameters a_i at T=0, obtained by fitting the experimental data to respective polynomials in nuclear mass region A=4-238, as [97, 98]

$$\begin{aligned} R_{0i}(T=0) &= 0.9543 + 0.0994A_i - 9.8851 \times 10^{-4}A_i^2 \\ &\quad +4.8399 \times 10^{-6}A_i^3 - 8.4366 \times 10^{-9}A_i^4 \\ a_i(T=0) &= 0.3719 + 0.0086A_i - 1.1898 \times 10^{-4}A_i^2 \\ &\quad +6.1678 \times 10^{-7}A_i^3 - 1.0721 \times 10^{-9}A_i^4. \end{aligned} \tag{2.92}$$

The T-dependence in the above formulas are then introduced as in Ref. [99],

$$\begin{aligned} R_{0i}(T) &= R_{0i}(T=0)[1 + 0.0005T^2], \\ a_i(T) &= a_i(T=0)[1 + 0.01T^2]. \end{aligned} \tag{2.93}$$

2.5 Wong Formula for fusion cross-section and its extension for explicit ℓ-summation effects

2.5.1 Wong formula

According to Wong [62], the fusion cross-section, in terms of ℓ partial waves, for two deformed and oriented nuclei (with orientation angles θ_i), lying in the same plane and colliding with center-of-mass (c.m.) energy $E_{c.m.}$, is

$$\sigma(E_{c.m.},\theta_i) = \frac{\pi}{k^2}\sum_{\ell=0}^{\ell_{max}}(2\ell+1)P_\ell(E_{c.m.},\theta_i), \tag{2.94}$$

with $k = \sqrt{\frac{2\mu E_{c.m.}}{\hbar^2}}$, and μ as the reduced mass. Here, P_ℓ is the transmission coefficient for each ℓ which describes the penetration of barrier $V_T^\ell(R,E_{c.m.},\theta_i)[= V_N(R,A_i,\beta_{\lambda i},T,\theta_i)+V_C(R,Z_i,\beta_{\lambda i},T,\theta_i)+V_\ell(R,A_i,\beta_{\lambda i},T,\theta_i)]$, and ℓ_{max} is the maximum angular momentum, defined later. Using Hill-Wheeler [100] approximation of assimilating the shape of the interaction barrier $V_\ell(R,E_{c.m.},\theta_i)$ through an inverted harmonic oscillator $[V_T^\ell(R,E_{c.m.},\theta_i) = V_B^\ell(E_{c.m.},\theta_i) - \frac{1}{2}\mu\omega^2(R-R_B^\ell)^2]$, the penetrability P_ℓ, in terms of its barrier height $V_B^\ell(E_{c.m.},\theta_i)$ and curvature $\hbar\omega_\ell(E_{c.m.},\theta_i)$, is

$$P_\ell = \left[1+\exp\left(\frac{2\pi(V_B^\ell(E_{c.m.},\theta_i)-E_{c.m.})}{\hbar\omega_\ell(E_{c.m.},\theta_i)}\right)\right]^{-1}, \tag{2.95}$$

with $\hbar\omega_\ell(E_{c.m.},\theta_i,\Phi)$, evaluated at the barrier position $R = R_B^\ell$ corresponding to the maximum barrier height $V_B^\ell(E_{c.m.},\theta_i,\Phi)$, given as

$$\hbar\omega_\ell(E_{c.m.},\theta_i) = \hbar\left[|d^2V^\ell(R)/dR^2|_{R=R_B^\ell}/\mu\right]^{1/2}, \tag{2.96}$$

and, the R_B^ℓ obtained from the condition

$$|dV_T^\ell(R)/dR|_{R=R_B^\ell} = 0.$$

Instead of solving Eq. (2.94) explicitly, which requires the complete ℓ-dependent potentials $V_T^\ell(R, E_{c.m.}, \theta_i)$, Wong [62] carried out the ℓ-summation in Eq. (2.94) approximately under the conditions:

(i) $\hbar\omega_\ell \approx \hbar\omega_0$, and (ii) $V_B^\ell \approx V_B^0 + \frac{\hbar^2\ell(\ell+1)}{2\mu {R_B^0}^2}$,

which means to assume $R_B^\ell \approx R_B^0$ also. In other words, both V_B^ℓ and $\hbar\omega_\ell$ are obtained in terms of its ℓ=0 values, with V_B^0 given as the sum of nuclear proximity potential V_P and Coulomb potential V_C at $R = R_B^0$,

$$V_B^0 = V_P(R = R_B^0, A_i, \beta_{\lambda i}, E_{c.m.}, \theta_i) + V_C(R = R_B^0, Z_i, \beta_{\lambda i}, E_{c.m.}, \theta_i) \tag{2.97}$$

where $\beta_{\lambda i}$, λ=2,3,4 are the static quadrupole, octupole and hexadecapole deformations.

Using the above two approximations, and replacing the ℓ-summation in Eq. (2.94) by an integral, gives on integration the Wong formula [62]

$$\sigma(E_{c.m.}, \theta_i) = \frac{{R_B^0}^2\hbar\omega_0}{2E_{c.m.}} \ln\left[1 + \exp\left(\frac{2\pi}{\hbar\omega_0}(E_{c.m.} - V_B^0)\right)\right], \tag{2.98}$$

which on integrating over the orientation angles θ_i, gives the fusion cross-section

$$\sigma(E_{c.m.}) = \int_{\theta_i=0}^{\pi/2} \sigma(E_{c.m.}, \theta_i) sin\theta_1 d\theta_1 sin\theta_2 d\theta_2. \tag{2.99}$$

It is important to remind here that the characteristics of only the ℓ=0 barrier play role in Wong formula.

2.5.2 Extended-Wong model including ℓ-summation explicitly

In 2009, Gupta and collaborators [101] calculated the barrier characteristics (the barrier height, position as well as the oscillator frequency) for the illustrative case ^{48}Ca+^{238}U (^{48}Ca being a spherical nucleus, only the deformations of ^{238}U comes into play) at various ℓ values and noticed that angular momentum plays an important role in changing barrier characteristics, as shown in Fig. 2 of Ref. [101]. Hence, the ℓ summation is carried out explicitly, for the ℓ_{max} determined empirically for a best fit to the measured cross-section, as shown in Fig. 1 of Ref. [101]. Here the θ integrated cross section, summed up to ℓ, are plotted as a function of ℓ itself.

This procedure of explicit ℓ summation works very well at above barrier energies whereas it fails to reproduce the data at sub-barrier energies and, as in Misicu and Esbensen [102] for M3Y potential, demands modification of the barrier, which we carry out here in various ways: (i) keeping the curvature $\hbar\omega_\ell$ same and modifying the barrier height V_B^ℓ, by ΔV_B^{emp}, i.e., define

$$V_B^\ell(modified) = V_B^\ell + \Delta V_B^{emp},$$

or (ii) keep the barrier height V_B^ℓ same and modify the curvature $\hbar\omega_\ell$ as

$$\hbar\omega_\ell(modified) = \hbar\omega_\ell + \Delta\hbar\omega^{emp}.$$

or (iii) with the use of different interaction potentials like ones based on different Skyrme forces, or by using different proximity potentials. In this thesis, various versions of nuclear interaction potentials are used to modify the barrier for the best fit of fusion cross-section at below barrier region.

The main point of difference in the two models (DCM and Wong) is that in Wong model, the pre-formation probability P_0=1 and penetrability is calculated by

the Hill-Wheeler approximation [100] and the same in DCM is obtained by WKB integral. On the other hand preformation probability P_0 is used to address the formation probability of decaying fragments of CN state in DCM. DCM is the generalized form of Wong model in which we address individual cross-sections of various decay channels as well as the total fusion cross-sections, whereas Wong formula or extended-Wong model handles only the fusion cross-section.

Bibliography

[1] R. K. Gupta, R. Kumar, N. K. Dhiman, M. Balasubraniam, W. Scheid, and C. Beck, Phys. Rev. C **68**, 014610 (2003).

[2] M. Balasubraniam, R. Kumar, R. K. Gupta, C. Beck, and W. Scheid, J. Phys. G **29**, 2703 (2003).

[3] R. K. Gupta, M. Balasubraniam, R. Kumar, D. Singh, and C. Beck, Nucl. Phys. A **738**, 479c (2004).

[4] R. K. Gupta, M. Balasubramaniam, R. Kumar, D. Singh, C. Beck, and W. Greiner, Phys. Rev. C **71**, 014601 (2005).

[5] B. B. Singh, M. K. Sharma, R. K. Gupta, and W. Greiner, Int. J. Mod. Phys. E **15**, 699 (2006).

[6] B. B. Singh, M. K. Sharma, and R. K. Gupta, Phys. Rev. C **77**, 054613 (2008).

[7] S. Kanwar, M. K. Sharma, B. B. Singh, R. K. Gupta, and W. Greiner, Int. J. Mod. Phys. E **18**, 1453 (2009).

[8] S. K. Arun, R. Kumar, and R. K. Gupta, J. Phys. G: Nucl. Part. Phys. **36**, 085105 (2009).

[9] M. K. Sharma, S. Kanwar, G. Sawhney, R. K. Gupta, and W. Greiner, J. Phys. G: Nucl. Part. Phys. **38**, 055104 (2011); D. Jain, R. Kumar, M. K. Sharma, and R. K. Gupta, Phys. Rev. C **85**, 024615 (2012).

[10] M. K. Sharma, G. Sawhney, R. K. Gupta, and W. Greiner, J. Phys. G: Nucl. Part. Phys. **38**, 105101 (2011).

[11] M. K. Sharma, G. Sawhney, S. Kanwar, and R. K. Gupta, Mod. Phys. Lett. A **25**, 2022 (2010).

[12] G. Sawhney and M. K. Sharma, Eur. Phys. J. A **48**, 57 (2012).

[13] M. K. Sharma, S. Kanwar, G. Sawhney, and R. K. Gupta, Phys. Rev. C **85**, 064602 (2012).

[14] M. Kaur, R. Kumar, and M. K. Sharma, Phys. Rev. C **85**, 014609 (2012).

[15] M. Kaur and M. K. Sharma, Phys. Rev. C **85**, 054605 (2012).

[16] K. Sandhu, M. K. Sharma, and R. K. Gupta, Phys. Rev. C **85**, 024604 (2012).

[17] S. S. Malik and R. K. Gupta, Phys. Rev. C **39**, 1992 (1989).

[18] S. Kumar and R. K. Gupta, Phys. Rev. C **55**, 218 (1997).

[19] S. K. Arun, R. K. Gupta, B. B. Singh, S. Kanwar, and M. K. Sharma, Phys. Rev. C **79**, 064616 (2009).

[20] S. K. Arun, R. K. Gupta, S. Kanwar, B. B. Singh, and M. K. Sharma, Phys. Rev. C **80**, 034317 (2009).

[21] G. Sawhney, M. K. Sharma, and R. K. Gupta, Phys. Rev. C **83**, 064610 (2011).

[22] R. Kumar and M. K. Sharma, Phys. Rev. C **85**, 054612 (2012).

[23] J. Maruhn and W. Greiner, Phys. Rev. Lett. **32**, 548 (1974).

[24] R. K. Gupta, W. Scheid, and W. Greiner, Phys. Rev. Lett. **35**, 353 (1975).

[25] A. Săndulescu, R. K. Gupta, W. Scheid, and W. Greiner, Phys. Lett. B **60**, 225 (1976).

[26] R. K. Gupta, A. Săndulescu, and W. Greiner, Phys. Lett. B **67**, 257 (1977); Rev. Roum. Phys. **23**, 51 (1978).

[27] S. Yamaji, W. Scheid, H. J. Fink, and W. Greiner, Z. Phys. A **278**, 69 (1976).

[28] S. Yamaji, W. Scheid, H. J. Fink, and W. Greiner, J. Phys. G: Nucl. Phys. **2**, L189 (1976).

[29] S. Yamaji, K. H. Ziegenhain, H. J. Fink, W. Greiner, and W. Scheid, J. Phys. G: Nucl. Phys. **3**, 1283 (1977).

[30] R. K. Gupta, A. Săndulescu, and W. Greiner, Z. Naturforsch. **32a**, 704 (1977).

[31] R. K. Gupta, C. Pirvulescu, A. Săndulescu, and W. Greiner, Z. Phys. A **283**, 217 (1977); Sovt. J. Nucl. Phys. **28**, 160 (1978).

[32] R. K. Gupta, Z. Physik. A **281**, 159 (1977).

[33] A. Săndulescu, H. J. Lustig, J. Hahn, and W. Greiner, J. Phys. G: Nucl. Phys. **4**, L279 (1978).

[34] H. J. Lustig, J. A. Maruhn, and W. Greiner, J. Phys. G: Nucl. Phys. **6**, L25 (1980).

[35] H. J. Fink, W. Greiner, R. K. Gupta, S. Liran, J.H. Maruhn, W. Scheid, and O. Zohni, in Proceedings of Int. Conf. on Reaction between Complex Nuclei, Nashville, 1974, 21, (Amsterdam: North Holland), pages 2.

[36] R. K. Gupta, IANCAS Bull. (India), **6**, 2 (1990).

[37] V. M. Strutinsky, Nucl. Phys. A **95**, 420 (1967).

[38] K. A. Brueckner, C. A. Levinson, and H. H. Mohmoud, Phys. Rev. **95**, 217 (1954).

[39] K. A. Brueckner, J. L. Gammel, and H. Weitzner, Phys. Rev. **110**, 431 (1958).

[40] K. A. Brueckner, A. M. Lockett, and M. Rotenberg, Phys. Rev. **121** 255 (1961).

[41] K. A. Brueckner, J. R. Buchler, and M. Kelley, Phys. Rev. **173**, 944 (1968).

[42] D. Vautherin and D. M. Brink, Phys. Rev. C **5**, 626 (1972).

[43] T. H. R. Skyrme, Phil. Mag. **1**, 1043 (1956); Nucl. Phys. **9**, 615 (1959).

[44] G. Audi, A. H. Wapstra and C. Thiboult, Nucl. Phys. A **729**, 337 (2003).

[45] P. Möller, J. R. Nix, W. D. Myers, and W. J. Swiatecki, At. Data Nucl. Data Tables **59**, 185 (1995).

[46] N. J. Davidson, S. S. Hsiao, J. Markram, H. G. Miller, and Y. Tzeng, Nucl. Phys. A **570**, 61c (1994).

[47] P. A. Seeger, Nucl. Phys. **25**, 1 (1961).

[48] S. DeBenedetti, Nuclear Interactions (New York: Wiley) (1964).

[49] W. Myers and W. J. Swiatecki, Nucl. Phys. **81**, 1 (1966).

[50] G. Audi and A. H. Wapstra, Nucl. Phys. A **595**, 4 (1995).

[51] R. K. Gupta, S. Kumar, M. Balasubramaniam, G. Münzenberg, and W. Greiner, J. Phys. G : Nucl. Part. Phys. **28**, 699 (2002).

[52] R. K. Gupta, M. Balasubramaniam, S. Kumar, S. K Patra, G. Münzenberg, and W. Greiner, J. Phys. G : Nucl. Part. Phys. **32**, 565 (2006).

[53] J. Blocki, J. Randrup, W. J. Swiatecki, and C. F. Tsang, Ann. Phys. (NY) **105**, 427 (1977).

[54] Deryagin, Kolloid Z. **69**, 155 (1934).

[55] R. K. Gupta, M. Balasubramaniam, R. Kumar, N. Singh, M. Manhas, and W. Greiner, J. Phys. G: Nucl. Part. Phys. C **31**, 631 (2005).

[56] A. Gray, *Modern Differential Geometry of Curves and Surfaces with Mathematica*, 2nd Edition, CRC Press, Boca Raton, 1997, p.89.

[57] M. Seiwert, W. Greiner, V. Oberacker, and M.J. Rhoades-Brown, Phys. Rev. C **29**, 477 (1984).

[58] R. K. Gupta, N. Singh, and M. Manhas, Phys. Rev. C **70**, 034608 (2004).

[59] N. Malhotra and R. K. Gupta, Phys. Rev. C **31**, 1179 (1985).

[60] M. Münchow, D. Hahn and W. Scheid, Nucl. Phys. A **388**, 381 (1982).

[61] M. J. Rhoades-Brown, V. E. Oberacker, M. Seiwert and W. Greiner, Z. Phys. A **310**, 287 (1983)

[62] C. Y. Wong, Phys. Rev. Lett. **31**, 766 (1973).

[63] S. Kailas (private communication).

[64] H. Kröger and W. Scheid, J. Phys. G **6**, L85 (1980).

[65] R. K. Gupta, M. Manhas, and W. Greiner, Phys. Rev. C **73**, 054307 (2006).

[66] Y. J. Shi and Swiatecki, Phys. Rev. C **54**, 300 (1985).

[67] M. Greiner and W. Scheid, J. Phys. G: Nucl. Phys. **12** L229 (1986).

[68] G. A. Pik-Pichak, Yad. Fiz. **44**, 1421 (1986).

[69] R. Blendowske and H. Walliser, Phys. Rev. Lett. **61**, 1930 (1988).

[70] B. Buck and A. C. Merchant, J. Phys. G: Nucl. Phys. **15**, 615 (1989).

[71] A. Sandulescu, R. K. Gupta, F. Carstoiu, M. Horoi, and W. Greiner, Int. J. Mod. Phys. E **1**, 374 (1992).

[72] R. Blendowske, T. Fliessbach, and H. Walliser, Nucl. Phys. A **464**, 75 (1987).

[73] Niyti, G. Sawhney, M.K. Sharma, and R.K. Gupta, Phys. Rev. C **91**, 054606 (2015).

[74] T. Matsuse, C. Beck, R. Nouicer, and D. Mahboub, Phys. Rev. C **55**, 1380 (1997).

[75] S. J. Sanders, D. G. Kovar, B. B. Back, C. Beck, D. J. Henderson, R. V. F. Janssens, T. F. Wang, and B. D. Wilkins, Phys. Rev. C **40**, 2091 (1989).

[76] S. J. Sanders, Phys. Rev. C **44**, 2676 (1991).

[77] J. Gomez del Campo, R.L. Auble, J.R. Beene, M.L. Halbert, H.J. Kim, A. D'Onofrio, and J.L. Charvet, Phys. Rev. C **43**, 2689 (1991); Phys. Rev. Lett. **61**, 290 (1988).

[78] R. J. Charity, M. A. McMahan, G. J. Wozniak, R. J. McDonald, L. G. Moretto, D. G. Sarantites, L. G. Sobotka, G. Guarino, A. Pantaleo, L. Fiore, A. Gobbi and K. D. Hildenbrand, Nucl. Phys. A **483**, 371 (1988).

[79] C. Beck, R. Nouicer, D. Disdier, G. Duchêne, G. de France, R.M. Freeman, F. Haas, A. Hachem, D. Mahboub, V. Rauch, M. Rousseau, S.J. Sanders, and A. Szanto de Toledo, Phys. Rev. C **63**, 014607 (2001).

[80] S.J. Sanders, D.G. Kovar, B.B. Back, C. Beck, B.K. Dichter, D. Henderson, R.V.F. Janssens, J.G. Keller, S. Kaufman, T.-F. Wang, B. Wilkins, and F. Videbaek, Phys. Rev. Lett. **59**, 2856 (1987).

[81] S. Misicu and H. Esbensen, Phys. Rev. Lett. **96**, 112701 (2006); *ibid* Phys. Rev. C **75**, 034606 (2007).

[82] A. Kaur, S. Chopra, and R. K. Gupta, Phys. Rev. C **90**, 024619 (2014).

[83] S. Chopra, A. Kaur, and R. K. Gupta, Phys. Rev. C **91**, 034613 (2015).

[84] S. Chopra, A. Kaur, Hemdeep and R. K. Gupta, Phys. Rev. C **93**, 044604 (2016).

[85] S. Chopra, A. Kaur, and R. K. Gupta, Phys. Rev. C **91**, 014602 (2015).

[86] R. K. Gupta, D. Singh, R. Kumar, and W. Greiner, J. Phys. G: Nucl. Part. Phys. **36**, 075104 (2009).

[87] R. Kumar, M. K. Sharma, and R. K. Gupta, Nucl. Phys. A **870-871**, 42 (2011).

[88] D. Jain, R. Kumar, M. K. Sharma, and R. K. Gupta, Phys. Rev. C **85**, 024615 (2012).

[89] M. Brack, C. Guet, and H.-B. Hakansson, Phys. Rep. **123**, 275 (1985).

[90] J. Friedrich and P.-G. Reinhardt, Phys. Rev. C **33**, 335 (1986).

[91] B. K. Agrawal, S. K. Dhiman, and R. Kumar, Phys. Rev. C. **73**, 034319 (2006).

[92] B. K. Agrawal, S. Shlomo, and V. K. Au, Phys. Rev. C. **72**, 014310 (2005).

[93] G.-Q. Li, J. Phys. G: Nucl. Part. Phys. **17**, 1 (1991).

[94] J. Blocki, J. Randrup, W. J. Swiatecki, and C. F. Tsang, Ann. Phys. (N.Y.) **105**, 427 (1977).

[95] R. K. Gupta, D. Singh, and W. Greiner, Phys. Rev. C **75**, 024603 (2007).

[96] J. Bartel and K. Bencheikh, Eur. Phys. J. A. **14**, 179 (2002).

[97] L. R. B. Elton, *Nuclear Sizes* (Oxford University Press, London, 1961).

[98] H. de Vries, C. W. de Jager, and C. de Vries, At. Data Nucl. Data Tables **36**, 495 (1987).

[99] S. Shlomo and J. B. Natowitz, Phys. Rev. C **44**, 2878 (1991).

[100] D. L. Hill and J. A. Wheeler, Phys. Rev. **89**, 1102 (1953); T D Thomas, Phys. Rev. **116**, 703 (1959).

[101] R. Kumar, M. Bansal, S. K. Arun, and R. K. Gupta, Phys. Rev. C. **80**, 034618 (2009).

[102] S. Misicu and H. Esbensen, Phys. Rev. Lett. **96**, 112701 (2006).

Chapter 3

α *vs.* non-α cluster decay of excited compound nucleus ^{124}Ce* using the dynamical cluster-decay model

3.1 Introduction:

The Dynamical Cluster-decay Model (DCM) [1–14] is used here for the first time to study the decay of any proton-rich excited (T>0) compound nucleus (CN). Ground-state (T=0) decays of proton-rich $^{116-124}$Ce and other neighboring nuclei $^{108-116}$Xe, $^{112-120}$Ba, $^{120-124}$Nd, $^{124-128}$Sm, and $^{128-132}$Gd have been studied by Gupta *et al.* [15,16] on the basis of preformed cluster model (PCM) of Gupta and Malik [17,18]. The calculated preformation probabilities P_0 and decay half-lives $T_{1/2}$ show a clear preference for A=4n, α-nuclei, like ^{4}He, ^{8}Be, ^{12}C, ^{16}O, etc., emitted from N=Z parents. Stressing the importance of doubly magic ^{100}Sn daughter, ^{8}Be decay of ^{108}Xe, ^{12}C decay of ^{112}Ba, and ^{16}O decay of ^{116}Ce, etc., were predicted to be the most probable (smallest decay half-life) cluster-decay cases, in addition to α-decay in each case. Motivated by these calculations on PCM [15,16], and of other authors [19,20] on unified fission model (UFM), an unsuccessful experimental attempt on ^{12}C-decay

of ^{114}Ba was also made [21]. As the N/Z ratio becomes larger than one, i.e., N/Z>>1 for parent nuclei, the A=4n+2, non-α nuclei clusters, like the one observed in exotic cluster-decays of radioactive nuclei (with doubly magic ^{208}Pb daughter), also become prominent, though still less probable than the A=4n, α-nuclei clusters [15]. Faced with such a situation, the decay of excited (T>0) compound nuclei ^{116,118,122}Ba* were studied both experimentally [22–27] and theoretically [5,8,13], which resulted in the observation and interpretation of a new phenomenon of intermediate mass fragments (IMFs, 5≤A≤20, 3≤Z≤10), in addition to multiple light-particles (LPs, like n, p, α) evaporation residues (ER, A≤4, Z≤2) and near-symmetric and symmetric fission fragments, termed fusion-fission (ff), at a given excitation energy E*. Here, in the following, we present our published work of the decay of ^{124}Ce* [28,29] and study the relative production of A=4n, α-nuclei like ^{8}Be, ^{12}C, ^{16}O, etc., *w.r.t.* A≠4n, non-α nuclei like ^{6}Be, ^{10}C, ^{14}N, etc., for the hot CN decay of ^{124}Ce* at a fixed E*. We choose to use the DCM [1–14], an extended version of PCM for T≠0 systems.

^{124}Ce*, formed in ^{32}S+^{92}Mo reaction at the above Coulomb barrier (∼109 MeV) beam energy of 150 MeV (equivalently, the center-of-mass energy $E_{c.m.}$=111.3 MeV), has been studied experimentally [30] for its decays to various evaporation residues, like ^{121}La, $^{120-122}$Ba, $^{118-121}$Cs, $^{117-120}$Xe, ^{117}I, and ^{114}Te, which refer to complementary light particles A≤4, Z≤2 and intermediate mass fragments 5≤A≤10, 3≤Z≤6. Specifically, ^{124}Ce being a proton-rich, near the proton-drip line nucleus, ^{120}Xe, ^{121}Cs and ^{122}Ba residues are produced, respectively, due to the evaporation of 4p, 3p and 2p, and with enhanced cross-sections. The relative cross-sections of various decay products are obtained by normalizing them with respect to that of ^{120}Cs, which itself could be populated only by the evaporation of 3pn, i.e., ^{4}Li from the compound nucleus. Application of the statistical code PACE4 to this data [30] shows large deviations in all above cases of proton clusters (2p, 3p, 4p) as well as the ^{118}Xe residue which refers to ^{6}Be decay. Interestingly, ^{116}Xe (≡^{8}Be, the α-nucleus)

decay is *not observed* in this experiment (not even the upper limit is given), and the decay mechanism of ^{118}Xe ($\equiv^{6}$Be, a non-α nucleus) is not fully established via the statistical code.

Using the DCM, here we compare the population of ^{6}Be ($\equiv^{118}$Xe residue) and ^{8}Be ($\equiv^{116}$Xe residue) by studying the relative cross-sections of ^{6}Be and ^{8}Be *w.r.t.* ^{4}Li ($\equiv^{120}$Cs). We find that relative populations of ^{8}Be and ^{6}Be are comparable, with the α-nucleus ^{8}Be dominating over the non-α nucleus ^{6}Be because the α-nucleus structure remains intact even at excitation energies where shell effects in binding energies reduce to almost zero [31]. Also, our predictions of relative cross-sections for the next α- *vs.* non-α nucleus clusters, i.e., ^{12}C *vs.* ^{10}C are compared. Note that the DCM calculations include deformation effects up to hexadecapole deformations (β_{2i}, β_{3i}, β_{4i}) with "compact" orientations (θ_{ci}, i=1, 2), for the case of co-planer nuclei (azimuthal angle $\Phi=0^{0}$; see Fig. 2.1), obtained as per prescription in [33] for the hot fusion process.

Thus, this work is at least of three-fold interest, namely: (i) The compound system ^{124}Ce* lies near the proton-drip line, resulting in enhanced emission of multiple proton (2p, 3p, 4p) clusters. Such reactions are not studied very much and is also being studied here for the first time on the DCM. (ii) The experiment shows a predominant emission of ^{6}Be, whereas our earlier theoretical work on ground-state (T=0, ℓ=0) decay of proton-rich systems [15, 16] showed a strong preference for α-nuclei clusters. Since the α-nucleus structure is present even for macroscopic energies [31], it is surprising that, the same for an excited (T>0) compound nucleus shows a complete absence of ^{8}Be in experiments. Note that even the upper limit of ^{8}Be production cross-section is not obtained in the experiment. (iii) The ground-state decay calculations for such nuclei on both the PCM and UFM [15, 16, 19, 20] stress the possibility of doubly-magic ^{100}Sn daughter radioactivity, which means that an absence of ^{8}Be in the decay of ^{124}Ce is not only surprising but alarming. If ^{8}Be is not observed in the decay of proton-rich nucleus, there is no chance for heav-

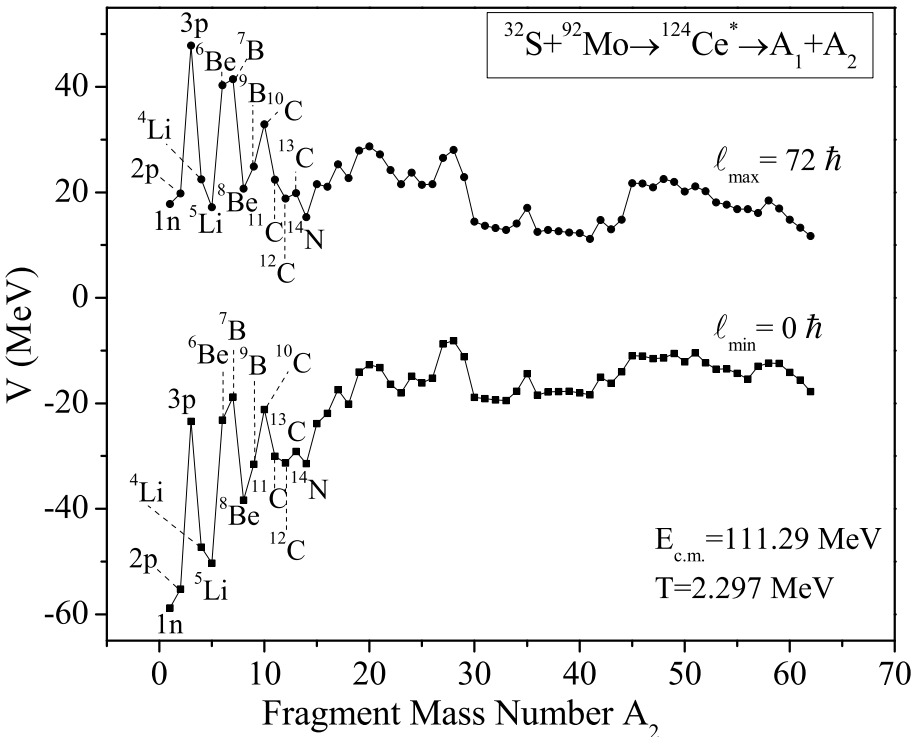

Figure 3.1: Mass fragmentation potential $V(A_2)$, minimized in charge fragmentation coordinate η_Z, for the decay of ^{124}Ce* formed in ^{32}S+^{92}Mo reaction at $E_{c.m.}$=111.29 MeV and at ℓ_{min} and ℓ_{max} values. Some of the most favored fragments are replaced by fragments of topical interest (see text). The best fitted ΔR values are: 1, 0.15, 0.793, 0.575, 0.37 and 1, respectively, for A_2=1, 2, 3, 4, 5, and 6-62.

ier clusters like ^{12}C, ^{16}O, etc., for ^{100}Sn like daughter products. Since the present experiment goes only up to ^{10}C, further measurements are called for.

3.2 Calculations and discussion of the results

As stated above, in this work we attempt to study the relative population of α-nucleus clusters like ^{8}Be, ^{12}C, etc., *w.r.t.* non-α nucleus clusters like ^{6}Be, ^{10}C, etc., in the decay of CN ^{124}Ce*, formed in ^{32}S+^{92}Mo reaction at a beam energy of 150 MeV. For this system, the relative cross-sections of various ERs (A$\leq$4, Z$\leq$2) and IMFs (5$\leq$A$\leq$10, 3$\leq$Z$\leq$6) are observed *w.r.t.* ^{4}Li, and for their use in the DCM, we have fitted the two LPs (2p and 3p) and two IMFs (^{5}Li and ^{6}Be) cross-sections in order to predict the behavior of the relative cross-sections of ^{7}B, ^{8}Be, ^{9}B, ^{10}C,

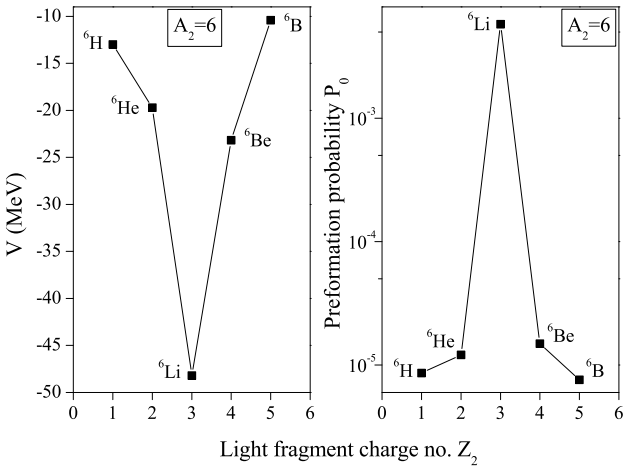

Figure 3.2: Same as for Fig. 3.1, but for (a) charge fragmentation potential $V(Z_2)$ and (b) preformation factor $P_0(Z_2)$, for mass fragment A_2=6 at ℓ_{min} value.

and ^{12}C, etc., clusters at a fixed temperature T=2.297 MeV, referring to 150 MeV beam-energy of the experiment [30]. Specifically, in this reaction, from the observed heavy residues, the light-particle ERs constitute 1n (not observed), 2p, 3p (or ^{3}H and ^{3}He) and ^{4}Li (or 4p and ^{4}He), while the IMFs include ^{5}Li (or ^{5}Be), ^{6}Be (or ^{6}Li), ^{7}B (or ^{7}Be), and ^{10}C. Apparently, the charge distribution effects (various isobars of decay fragment) are observed, but the ^{8}Be, ^{9}B and ^{12}C decays are not observed in this experiment.

Fig. 3.1 shows the calculated fragmentation potential V as a function of light fragment mass A_2 for the decay of CN ^{124}Ce* at $E_{c.m.}$=111.29 MeV (E_{Lab}=150 MeV or T=2.297 MeV), illustrated for ℓ_{min} and ℓ_{max} values, using the best fitted ΔR-values given in its figure caption and Table 3.1. In view of the observed charge distribution effects, in Fig. 3.1, we have replaced the binding energy of the energetically most favored fragment (the minimum binding energy) with that of the fragment of interest, i.e., fragment to be calculated. This is illustrated in Fig. 3.2(a) for A_2=6 where the minimized fragment is ^{6}Li, with largest preformation yield P_0 (Fig. 3.2(b)), but here we are interested in ^{6}Be due to its being of topical interest and/ or observed experimentally. Therefore, in Fig. 3.1, we have first replaced the binding energy of ^{6}Li by the corresponding binding energy of ^{6}Be (and its comple-

Table 3.1: DCM calculated relative cross-sections σ(Channel)/$\sigma(^{120}\text{Cs})$ in the decay of $^{124}\text{Ce}^*$ formed in $^{32}\text{S}+^{92}\text{Mo}$ reaction at E_{Lab}=150 and 140 MeV, compared with the experimental data $\sigma^{Expt.}$ [30] at E_{Lab}=150 MeV ($\equiv E_{c.m.}$=111.29 MeV, T=2.297 MeV). The neck-length parameter ΔR is fitted to data at E_{Lab}=150 MeV, taken same at E_{Lab}=140 MeV ($\equiv E_{c.m.}$=103.87 MeV, T=2.16 MeV). For qf component, $\sigma_{qf}^{Empirical} = \sigma(Channel)^{Expt.} - \sigma(Channel)^{Cal.}$ compared with $\sigma_{qf}^{Cal.}$ using DCM(P_0=1) for entrance channel. We also define $\sigma_{fusion} = \sum\sigma(Channel)$ for both the Expt. and Cal. cases, with $\sigma(Channel)$ here being relative to $\sigma(^{120}\text{Cs})$.

Decay-channel		ΔR	E_{Lab}=150 MeV					E_{Lab}=140 MeV
			σ (Channel)/$\sigma(^{120}\text{Cs})$		$\sigma_{qf}(\equiv \sigma_{nCN})$			σ (Channel)/$\sigma(^{120}\text{Cs})$
Light	Heavy	(fm)	Cal.	Expt.	Empirical	Cal.	ΔR_{qf} (fm)	Cal.
2p	^{122}Ba	0.15	0.44	0.46	0.02	0.02	0.2	0.47
3p	^{121}Cs	0.793	1.19	1.19	0	0.05	0.2	1.19
^{4}Li	^{120}Cs	0.575	1.0	1.0	0	5.6×10^{-4}	0.2	1.0
^{5}Li	^{119}Cs	0.37	0.18	0.18	0	4.1×10^{-4}	0.2	0.198
^{6}Be	^{118}Xe	1.0	1.63	1.63	0	4.4×10^{-4}	0.2	1.69
^{7}B	^{117}I	1.0	0.07	0.41	0.34	0.34	0.7	0.06
^{8}Be	^{116}Xe	1.0	3.28	-	-	1.2×10^{-5}	0.2	3.02
^{9}B	^{115}I	1.0	0.15	-	-	1.4×10^{-5}	0.2	0.14
^{10}C	^{114}Te	1.0	0.004	0.24	0.236	0.236	0.804	0.004
^{11}C	^{113}Te	1.0	0.55	-	-	2.1×10^{-5}	0.2	0.51
^{12}C	^{112}Te	1.0	12.25	-	-	1.3×10^{-4}	0.2	11.61

mentary heavy fragment). Similarly, for A_2=2, 3, 7 and 10, the energetically most favored fragments are, respectively, ^{2}H, ^{3}H, ^{7}Li, and ^{10}B which are replaced by the corresponding binding energies of 2p, 3p, ^{7}B and ^{10}C, and their heavy complementary fragments, being here the fragments of relatively first importance. The same procedure could subsequently be carried out for the other observed isobars, and the properly normalized charge distributions calculated. Interestingly, we notice in Fig. 3.1 that, compared to ^{6}Be and ^{10}C, ^{8}Be and ^{12}C, respectively, occur at the deeper minima in both ℓ_{min} and ℓ_{max} cases, establishing the result that, in the decay of

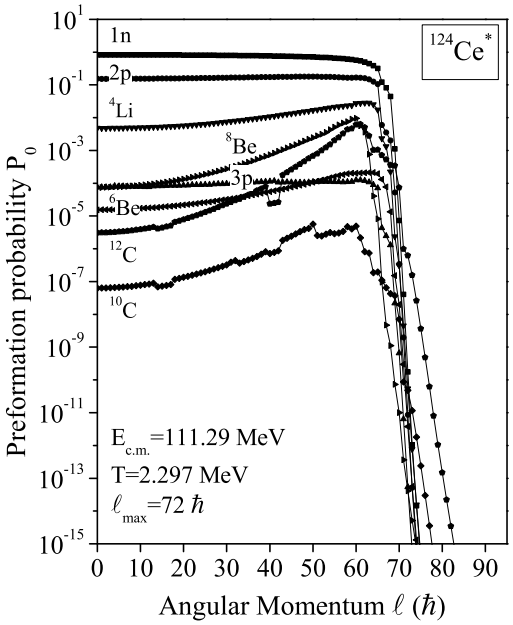

Figure 3.3: Preformation probability P_0 as a function of angular momentum ℓ for LPs and some IMFs decays of ^{124}Ce* formed in ^{32}S+^{92}Mo reaction at $E_{c.m.}$=111.29 MeV. ℓ_{max}=72 $\hbar$, except for ^{10}C and ^{12}C where it goes up to about 80 $\hbar$.

^{124}Ce*, independent of ℓ-value, A= 4n, α-nuclei are preferred over A=4n+2, non-α nuclei. Also, the ΔR values, equivalently the separation distance R_a, for 2p and 3p fragments are smaller (see, Fig. 3.1 Caption), such that the resulting Coulomb repulsion help enhancing their decay cross-sections, compared to the neighboring fragments. This is further shown more clearly in terms of the calculated preformation probability P_0 and channel cross-section σ_ℓ (see Figs. 3.3 and 3.5 below).

The ℓ_{max} and ℓ_{min} values are obtained, respectively, from P_0 and P plotted as functions of ℓ in Fig. 3.3 and Fig. 3.4 for LPs and some IMFs, or equivalently, the channel cross-section σ_ℓ as a function of ℓ, shown in Fig. 3.5. ℓ_{max} and ℓ_{min} are the values of ℓ where the contributions of P_0 and P to cross-section become negligible, i.e., the channel cross-section becomes negligible. We limit ourselves to $P_0 > 10^{-15}$, $P > 10^{-25}$, and $\sigma_\ell > 10^{-11}$, giving ℓ_{min}=0 $\hbar$ and ℓ_{max}=72 $\hbar$. Note that in Figs. 3.4 and 3.5, some channels begin at $\ell_{min} > 0$, which means that the lower ℓ-values do not contribute to the calculated cross-section, discussed below. Similarly, for some channels $\ell_{max} > 72$ $\hbar$, but again the contribution to the calculated cross-section is negligible.

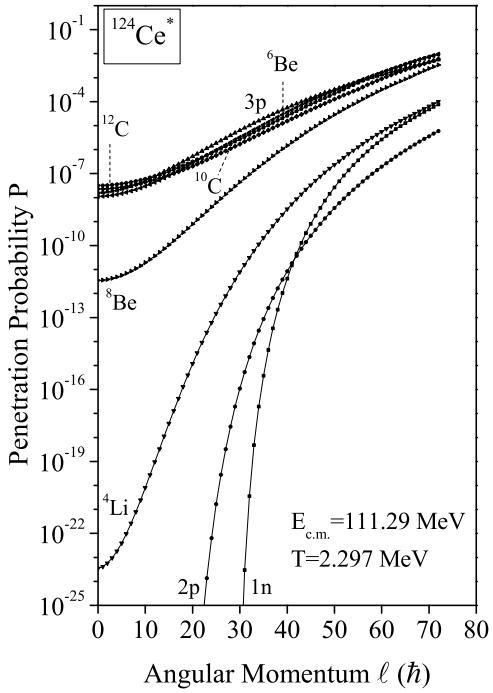

Figure 3.4: Same as for Fig. 5, but for penetration factor P.

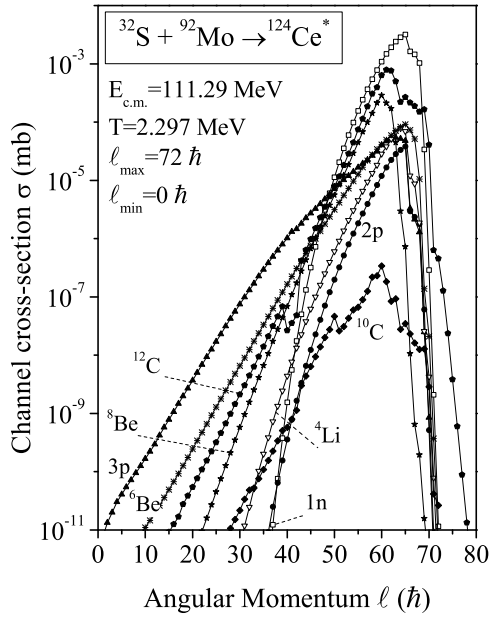

Figure 3.5: Channel cross-section σ as a function of angular momentum ℓ for the decay of ^{124}Ce* formed in ^{32}S+^{92}Mo reaction at $E_{c.m.}$=111.29 MeV.

Next, looking at the individual decay channels, Figs. 3.3 to 3.5 show that for 1n, though not observed in the experiment [30], the P_0 and σ_ℓ are nearly the largest though the P is smallest. It may be reminded that here we have fitted only two LPs and two IMFs. Very recently, Chopra *et al.* [14] have shown that if, instead of σ_{ER} alone, the sum $\sigma_{ER} + \sigma_{IMFs}$ were fitted then the, otherwise large, contribution of σ_{1n} reduces to nearly zero. 2p is also highly preformed though the penetrability is again smaller. On the other hand, 3p is relatively, weekly preformed though its penetrability is large (rather largest), such that the channel cross-sections are large for both 2p and 3p decays (see Fig. 3.5). Also, ^{6}Be and ^{8}Be are though relatively, weakly preformed but their penetrability being large make their cross-sections quite large. Note that ^{8}Be is preformed stronger than ^{6}Be, and so also is ^{12}C compared to ^{10}C, thereby making the ^{8}Be and ^{12}C channel cross-sections largest (see Fig. 3.5). This happens because of the inherent α-nucleus structure effects present in the fragmentation potential (Fig. 3.2) that are independent of ℓ values as well as the excitation energy, i.e., stay intact even at the above barrier energy, a macroscopic energy effect, where shell effects become negligible (e.g., see [31]). The concept of "barrier lowering", as discussed in Chapter 1, is described with the help of Fig. 3.6 where we notice that, as the barrier is effectively lowered, ΔV_B for each ℓ is defined as a negative quantity, as shown in Fig. 3.7. Thus, the fitting parameter ΔR controls the "barrier lowering" ΔV_B.

In Figs. 3.7 and 3.8, we have also plotted the preformation and penetration probabilities as a function of fragment mass number A_i (i=1, 2), for ℓ_{min} to ℓ_{max} values. We notice from Fig. 3.7 that the lower ℓ values contribute to LPs and the IMFs (A_2=5-16), and the higher ℓ values to heavy mass fragments (HMFs, A_2=28-46) and near-symmetric and symmetric fission region (nSF and SF, the ff region of A_2=53-62). On the other hand, P is almost of the same order for all ℓ values, and contribute mainly towards the magnitude of cross-section. The same result is better presented in Fig. 3.9 where the ℓ-summed P_0, P and channel cross-section σ are

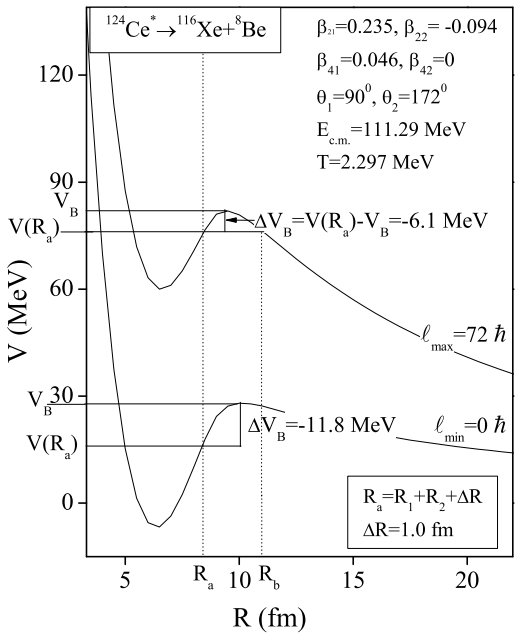

Figure 3.6: The ℓ-dependent scattering potential $V(R)$ for ^{116}Xe+^{8}Be in the decay of ^{124}Ce* formed in ^{32}S+^{92}Mo reaction at $E_{c.m.}$=111.29 MeV. The first and second turning points R_a and R_b are labelled, and the barrier lowering parameter $\Delta V_B = V(R_a) - V_B$ shown for both the ℓ_{max}=72 $\hbar$ and ℓ_{min}=0 $\hbar$ values.

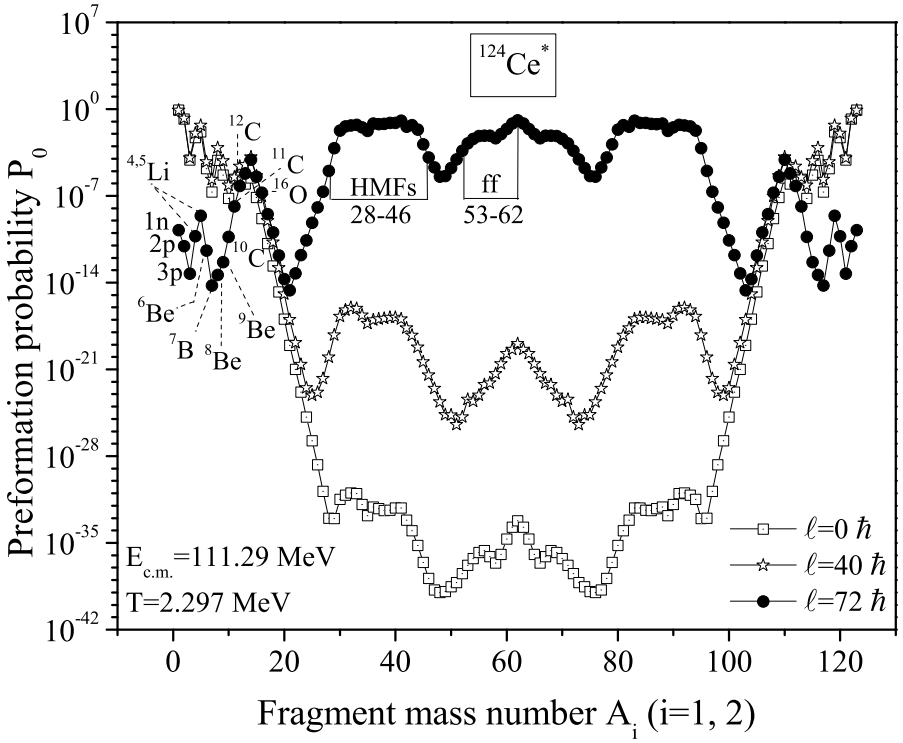

Figure 3.7: Preformation probability P_0 as a function of fragment mass number A_i (i=1, 2) for ^{124}Ce* formed in ^{32}S+^{92}Mo reaction at $E_{c.m.}$=111.29 MeV for ℓ_{min} to ℓ_{max} values.

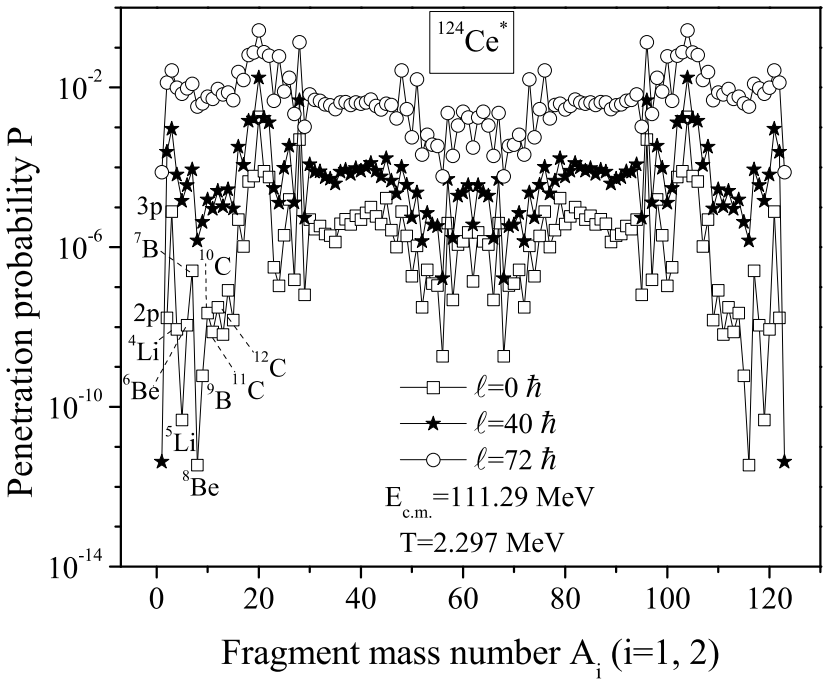

Figure 3.8: Same as for Fig. 5, but for penetrability P.

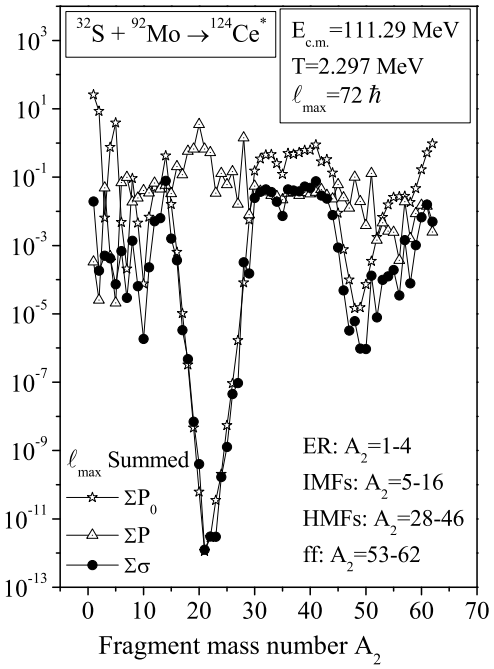

Figure 3.9: The ℓ-summed fragment preformation probability P_0, the penetrability P and the decay cross-section σ as a function of the light fragment mass number A_2 for compound system $^{124}Ce^*$ formed in $^{32}S+^{92}Mo$ reaction at $E_{c.m.}$=111.29 MeV, and ℓ_{max}=72 ħ.

plotted as a function of A_2. Apparently, the ℓ-summed P contributes only to the magnitude, and the ℓ-summed σ follow the behavior of ℓ-summed P_0, containing the structure effects of CN. Thus, in addition to the observed ER, for cross-sections of similar orders, the IMFs window is shown extended up to A_2=16 and a new decay region of heavy mass fragments (HMFs) of A_2=28 to 46, plus near-symmetric and symmetric fission fragments A_2=53-62 are clearly indicated, which on including the complementary heavy fragments result in ff region of $(A/2)\pm9$.

Table 3.1 and Fig. 3.10 show our DCM calculated cross-sections at 150 MeV laboratory energy, compared with the experimental data [30], given relative to ^{120}Cs ($\equiv$3pn or ^{4}Li). First of all we notice that, for the best fitted 2p, 3p, ^{5}Li and ^{6}Be cross-sections, ^{8}Be ($\equiv^{116}$Xe) and ^{12}C ($\equiv^{112}$Te) are shown to be relatively more populated than ^{6}Be ($\equiv^{118}$Xe) and ^{10}C ($\equiv^{114}$Te), respectively, as was found to be the case for the ground-state decay [15,16], and decay of ^{116}Ba* formed in ^{58}Ni+^{58}Ni reaction at various $E_{c.m.}$ [5]. ΔR-values used for various fragments are given in Table 3.1 and figure caption of Fig. 3.1. Secondly, from the point of view of CN formation probability P_{CN}, we notice that the overall comparison between the DCM calculations and data are good, wherever observed. This means that the (relative) non-compound qf-component is very small (the summed $\sigma_{qf}^{empirical}$=0.596, as obtained for only 2p, ^{7}B and ^{10}C for the empirically estimated σ_{qf} by using Eq. (2), given in Table 3.1 . This is to be compared with $\sigma_{fusion}^{Expt.} = \sum \sigma(Channel)^{Expt.}$=5.11). Then, using Eq. (3), $P_{CN} = 1 - \frac{0.596}{5.11} = 0.883 \approx 1$ for both the experiments and the DCM calculations of σ_{qf} for P_0=1 case, as expected for the above barrier bombarding energy, which is the case here. In Table 3.1, the DCM(P_0=1) calculations for entrance channel fit the empirical σ_{qf} almost exactly for a reasonable choice of neck-length parameter ΔR for qf process.

The authors of Ref. [30] state that a similar experiment was made at a below-barrier beam energy of 140 MeV ($E_{c.m.}$=103.87 MeV), but did not publish the data

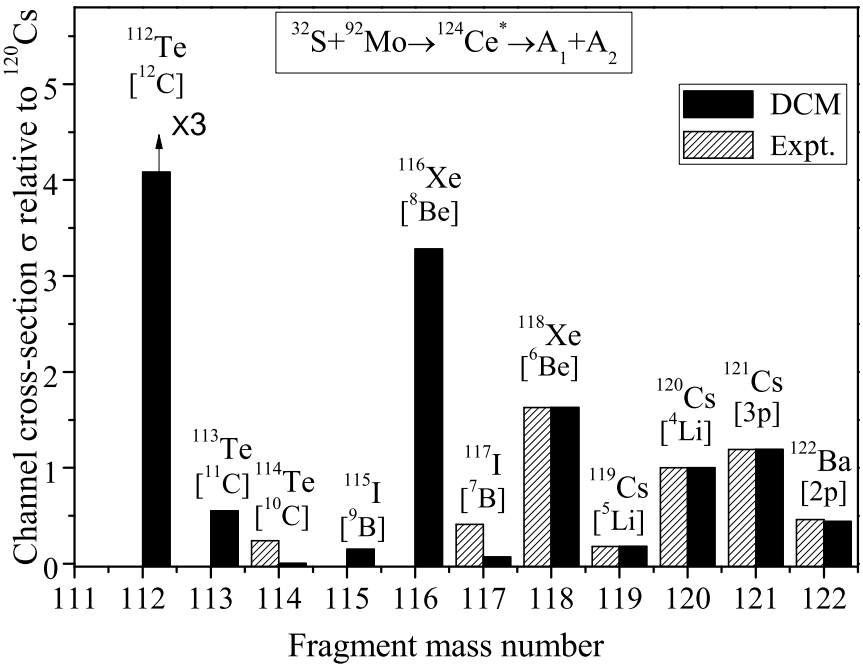

Figure 3.10: Comparison of DCM calculated and measured [30] relative cross-sections of various heavy residues *w.r.t.* ^{120}Cs. The corresponding light product is also shown in the bracket. No error bars are available for the measured data.

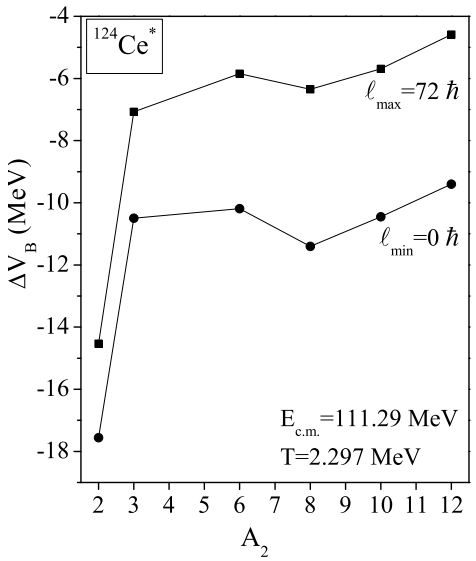

Figure 3.11: Variation of ΔV_B with A_2 for ℓ_{min} and ℓ_{max} values.

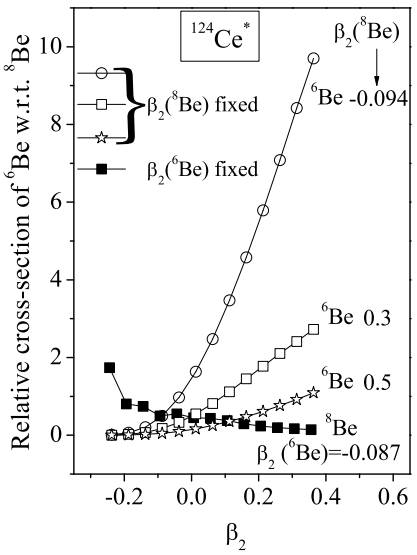

Figure 3.12: Relative cross-section of ^{6}Be *w.r.t.* ^{8}Be by (i) varying deformations of ^{8}Be for fixed $\beta_2(^6\text{Be})$=-0.087 (filled squares) and (ii) varying deformations of ^{6}Be for fixed $\beta_2(^8\text{Be})$=-0.094, 0.3 or 0.5 (un-filled circles, un-filled squares or un-filled stars, respectively), for decay of ^{124}Ce* formed in ^{32}S+^{92}Mo reaction at $E_{c.m.}$=111.29 MeV.

for the same. Table 3.1 includes the results of our calculation at this energy also, using ΔR-values determined for 150 MeV case. Interestingly, at this lower incident energy also, the A=4n, ^{8}Be and ^{12}C decays of ^{124}Ce* dominate over the A=4n+2, ^{6}Be and ^{10}C decays, respectively, as expected [31]. Furthermore, since this is a case of below-barrier incident energy, we expect a significant qf-component, and hence P_{CN} should be much less than unity.

Knowing that ΔR controls the "barrier lowering" parameter ΔV_B, we have plotted ΔV_B in Fig. 3.11 as a function of light fragment mass number A_2 for two limiting ℓ values. ΔV_B is an in-built property of the DCM, considered to be the only possible explanation to account for fusion hindrance phenomenon [7, 34, 35] in heavy ion reactions, particularly, at sub-barrier energies. This further speaks in favor of different nuclear interactions required for different heavy ion reactions [36]. We notice in Fig. 3.11 that ΔV_B is large (-8 to -18 MeV) for LPs (A_2=1-4) and much smaller (-6 to -11 MeV) for IMFs (A_2 >4), and that ΔV_B decreases with an increase in ℓ value for all decay channels. The later result occurs because at higher ℓ's the barrier

shifts towards the lower R value (see Fig. 3.6), and hence the first turning point R_a comes closer to barrier position V_B, which means that $V(R_a)$ increases and hence the difference ΔV_B decreases.

Another quantity of interest in this study is the deformation of, say, ^{6}Be and/ or ^{8}Be which are not known experimentally. The calculated cross-sections could, however, depend on the deformations β_2 used, which for the present calculations are taken from relativistic mean-field calculations [37], namely: β_2=-0.087 for ^{6}Be and -0.094 for ^{8}Be. In Fig. 3.12, we vary the deformation of ^{6}Be or ^{8}Be (only one at a time, keeping the other fixed), and calculate the relative cross-section of ^{6}Be *w.r.t.* ^{8}Be, i.e., $\sigma(^{6}Be)/\sigma(^{8}Be)$. The interesting result is that the relative cross-section of ^{6}Be *w.r.t.* ^{8}Be is nearly independent of the deformation of ^{8}Be (prolate/ oblate), but (depending on the deformation of ^{8}Be) increases many fold for prolate deformation of ^{6}Be, though remaining almost un-affected for its oblate deformations. The increase is large for small oblate deformation of ^{8}Be (un-filled circles), but becomes increasingly small for increasing prolate deformation of ^{8}Be (un-filled squares, and un-filled stars). Thus, it is clear from Fig. 3.12 that our results on relative cross-sections in Fig. 3.10 depend on the values of deformations used for the two nuclei.

3.3 Summary

Experimentally, the ^{32}S+^{92}Mo$\rightarrow^{124}$Ce* reaction has been studied at an incident center-of-mass energy $E_{c.m.}$=111.29 MeV (equivalently, the laboratory energy 150 MeV), and heavy mass decay products observed, whose complementary light decay products are the multiple proton clusters (2p, 3p, 4p) and intermediate mass fragments like ^{5}Li, ^{6}Be, ^{7}B, and ^{10}C, plus their isobars like ^{3,4}He, ^{5}Be, ^{6}Li, ^{7}Be, etc. In this paper, we have extended an application of the dynamical cluster-decay model (DCM) to this system at two different incident energies of $E_{c.m.}$=111.29 MeV ($\equiv$150

MeV beam energy) and 103.87 MeV (≡140 MeV beam energy), though the data are available only at the first above barrier energy. The measured cross-sections are given relative to ^{4}Li decay, and our aim is to compare the measured relative cross-sections of ^{6}Be and ^{10}C with ^{8}Be and ^{12}C, respectively, though both ^{8}Be and ^{12}C decays are not observed in this experiment (even the upper limits are not given). Neck-length is the only parameter of the model, whose value remains within ∼2 fm, the range of validity of proximity potential used here. For the best fitted neck-length parameters of two LPs (2p and 3p) and two IMFs (^{5}Li and ^{6}Be), the relative populations of ^{6}Be and ^{8}Be, and that of ^{10}C and ^{12}C are analyzed, showing thereby that the compound nucleus ^{124}Ce* decays preferentially via A=4n, α-nucleus clusters as compared to A≠4n, non-α nucleus clusters, similar to what was predicted for ground-state (T=0) decays, and shown earlier [5] for decay of ^{116}Ba* formed in ^{58}Ni+^{58}Ni reaction at various $E_{c.m.}$. This confirms the excitation energy independence of α-nucleus structure effects in ^{124}Ce*, similar to what was shown earlier for a lighter system ^{56}Ni* [31]. In the above barrier energy data, the possible non-compound nucleus effects are shown to be small and the CN formation probability calculated to be close to unity. However, the charge distribution due to observed isobars is not yet investigated.

Bibliography

[1] R. K. Gupta, M. Balasubramaniam, C. Mazzocchi, M. La Commara, and W. Scheid, Phys. Rev. C **65**, 024601 (2002).

[2] R. K. Gupta, R. Kumar, N. K. Dhiman, M. Balasubramaniam, W. Scheid and C. Beck, Phys. Rev. C **68**, 014610 (2003).

[3] M. Balasubramaniam, R. Kumar, R. K. Gupta, C. Beck and W. Scheid, J. Phys. G: Nucl. Part. Phys. **29**, 2703 (2003).

[4] R. K. Gupta, M. Balasubramaniam, R. Kumar, D. Singh, C. Beck and W. Greiner, Phys. Rev. C **71**, 014601 (2005).

[5] R. K. Gupta, M. Balasubramaniam, R. Kumar, D. Singh, S. K. Arun, and W. Greiner, J. Phys. G: Nucl. Part. Phys. **32**, 345 (2006).

[6] R. K. Gupta, *et al.*, Int. Rev. Phys. (IREPHY) **2**, 369 (2008).

[7] S. K. Arun, R. Kumar, and R. K. Gupta, J. Phys. G: Nucl. Part. Phys. **36**, 085105 (2009).

[8] R. Kumar and R. K. Gupta, Phys. Rev. C **79**, 034602 (2009).

[9] R. K. Gupta, Lecture Notes in Physics 818 *Clusters in Nuclei*, ed C. Beck, Vol.I, (Springer Verlag), p223 (2010).

[10] M. K. Sharma, G, Sawhney, R. K. Gupta, and W. Greiner, J. Phys. G: Nucl. Part. Phys. **38**, 105101 (2011).

[11] M. K. Sharma, S. Kanwar, G. Sawhney, and R. K. Gupta, Phys. Rev. C **85**, 064602 (2012).

[12] M. Bansal, S. Chopra, R. K. Gupta, R. Kumar, and M. K. Sharma, Phys. Rev. C **85**, 034604 (2012).

[13] M. Kaur, R. Kumar, and M. K. Sharma, Phys. Rev. C **85**, 014609 (2012).

[14] S. Chopra, M. Bansal, M. K. Sharma, and R. K. Gupta, Phys. Rev. C **88**, 014615 (2013).

[15] S. Kumar, D. Bir, and R. K. Gupta, Phys. Rev. C **51**, 1762 (1995).

[16] S. Kumar and R. K. Gupta, Phys. Rev. C **49**, 1922 (1994).

[17] R. K. Gupta, in *Proceedings of the 5th International Conference n Nuclear Reaction Mechanisms*, Varenna, Italy, edited by Gadioli E (Ricerca Scintifica Educazione Permanente, Milano, Italy), (1988), p. 416.

[18] S. S. Malik and R. K. Gupta, Phys. Rev. C **39**, 1992 (1989).

[19] D. N. Poenaru, D. Schnabel, W. Greiner, D. Mazilu, and R. Gherghescu, At. Data Nucl. Data Tables **48**, 231 (1991).

[20] D. N. Poenaru, W. Greiner, and E. Hourani, Phys. Rev. C **51**, 594 (1995).

[21] A. Guglielmetti, R. Bonetti, G. Poli, R. Collatz, Z. Hu, R. Kirchner, E. Roeckl, N. Gunn, P. B. Price, B. A. Weaver, and A. Westphal, Phys. Rev. C **56**, R2912 (1997); and references on earlier experiments there in it.

[22] J. Gomez del Campo, J. L. Charvet, A. D'Onofrio, R. L. Auble, J. R. Beene, M. L. Halbert, and H. J. Kim, Phys. Rev. Lett. **61**, 290 (1988).

[23] J. Gomez del Campo, R. L. Auble, J. R. Beene, M. L. Halbert, H. J. Kim, A. D'Onofrio, and J. L. Charvet, Phys. Rev. C **43**, 2689 (1991).

[24] J. Gomez del Campo, C. Baktash, H.-Q. Jin, D. Rudolph, A. D'Onofrio, F. Terrasi, G. de Angelis, M. De Poli, C. Fahlander, A. Gadea, D.R. Napoli, Q. Pan, P. Spolaore, L. De Acuna, D. Bazzacco, S. Lunardi, P. Pavan, C. Rossi-Alvarez, A. Buscemi, R. Zanon, A. De Rosa, L. Campajola, M. La Commara, G. Inglima, V. Roca, M. Romano, M. Sandoli, M. Romoli, A. Ordine, and D. Pierroutsakou, Phys. Rev. C **57**, R457 (1998).

[25] M. La Commara, J. Gomez del Campo, A. D'Onofrio, A. Gadea, M. Glogowski, P. Jarillo-Herrero, N. Belcari, R. Borcea, G. de Angelis, C. Fahlander, M. Gorska, H. Grawe, M. Hellström, R. Kirchner, M. Rejmund, V. Roca, E. Roeckl, M. Romano, K. Rykaczewski, K. Schmidt, and F. Terrasi, Nucl. Phys. A **669**, 43 (2000).

[26] E. Bonnet *et al.*, Int. J. Mod. Phys. E **17**, 2359 (2008).

[27] G. Ademard *et al.*, Phys. Rev. C **83**, 054619 (2011).

[28] A. Kaur, S. Chopra, and R. K. Gupta, Phys. Rev. C **89**, 034602 (2014).

[29] A. Kaur, S. Chopra, and R. K. Gupta, in *Proceedings of XXXIII Mazurian Lakes Conference on Physics*, Frontiers in Nuclear Physics, Piaski, Poland, Sept. 1-7, 2013; to be published in Acta Physica Polonica B.

[30] J. Ray, *et al.*, in *Proc. Department of Atomic Energy Symp. on Nucl. Phys.* **57**, 368 (2012); available on line at http://www.sympnp.org/proceedings/57/A93.pdf.

[31] M. K. Sharma, R. K. Gupta, and W. Scheid, J. Phys. G: Nucl. Part. Phys. **26**, L45 (2000).

[32] R. K. Gupta, M. Balasubramaniam, R. Kumar, N. Singh, M. Manhas, and W. Greiner, J. Phys. G: Nucl. Part. Phys. **31**, 631 (2005).

[33] R. K. Gupta, M. Manhas, and W. Greiner, Phys. Rev. C **73**, 054307 (2006).

[34] S. Misicu and H. Esbensen, Phys. Rev. Lett. **96**, 112701 (2006).

[35] S. Misicu and H. Esbensen, Phys. Rev. C **75**, 034606 (2007).

[36] R. Kumar, M. K. Sharma, and R. K. Gupta, Nucl. Phys. A **870-871**, 42 (2011).

[37] S. K. Patra, Private cmmunication.

Chapter 4

α *vs.* non-α cluster decays of excited compound nucleus ^{124}Ce* using various formulations of nuclear proximity potential.

4.1 Introduction

Continuing the work of Chapter 3 [1, 2], where it was shown that the α-nucleus structure of the proton-rich ^{124}Ce does not change in going from its ground-state (temperature T=0) decay [3, 4] to the decay of excited (T>0) compound nucleus ^{124}Ce*. As also discussed in Chapter 3, experimentally, ^{124}Ce*, formed in ^{32}S+^{92}Mo reaction at an above Coulomb barrier (barrier$\sim$109 MeV) beam energy of 150 MeV (equivalently, the center-of-mass energy $E_{c.m.}$=111.3 MeV), has been studied [5] for its decays to various evaporation residues, like ^{121}La, $^{120-122}$Ba, $^{118-121}$Cs, $^{117-120}$Xe, ^{117}I, and ^{114}Te, which refer to complementary light particles (LPs) A$\leq$4, Z$\leq$2 and intermediate mass fragments (IMFs) 5$\leq$A$\leq$10, 3$\leq$Z$\leq$6. Note, ^{116}Xe and ^{112}Te ($\equiv^8$Be and ^{12}C, respectively, the α-nuclei clusters) decays are *not observed* in this experiment (not even the upper limit is obtained). The relative cross sections of various

decay products are obtained by normalizing the data with respect to ^{120}Cs ($\equiv^{4}$Li). In our calculation [1, 2] in Chapter 3, based on the dynamical cluster-decay model (DCM) [6, 7] using, for nuclear proximity potential, the pocket formula of Blocki *et al.* [8], we compared the population of ^{6}Be, ^{10}C ($\equiv^{118}$Xe, ^{114}Te residues, respectively) with ^{8}Be, ^{12}C ($\equiv^{116}$Xe, ^{112}Te residues, respectively) by studying their relative cross sections *w.r.t.* ^{4}Li ($\equiv^{120}$Cs). We find that, for the best fitted neck-length parameter ΔR's (the only parameter of the model) up to A_2=6, the relative populations of ^{8}Be, ^{12}C and ^{6}Be, ^{10}C are comparable, with the α-nuclei ^{8}Be and ^{12}C dominating over the non-α nuclei ^{6}Be and ^{10}C. This means that the α-nucleus structure remains intact even at excitation energies where shell effects in binding energies reduce almost to zero [9]. Thus, in our DCM calculations, the excitation-energy independence of α-nucleus structure effects in ^{124}Ce* is confirmed. Note that, in all these studies, the pocket formula of Blocki *et al.* [8] is used for the nuclear proximity potential, and it would certainly be of interest to see if the above result is independent of (or dependent on) the choice of nuclear interaction potential [10]. Therefore, in this chapter, we extend the study of Chapter 3 to the use of various other nuclear proximity potential functions derived from the Skyrme energy density formalism (SEDF) based on the semiclassical extended Thomas Fermi (ETF) method under the frozen density approximation [11–13].

The SEDF in ETF approach (as discussed in Sec. 2.4.3 in Chapter 2) provides a convenient basis for calculating the interaction potential between two colliding nuclei. In SEDF, the nucleus-nucleus interaction potential, as a function of separation distance R, is defined as the difference of the energy expectation value of the Skyrme Hamiltonian density for the two nuclei at finite separation R and when they are completely separated, i.e., $R = \infty$. Knowing that different nuclear interaction potentials give rise to different barrier characteristics (barrier height, position, and curvature), we can consider using different nuclear proximity potentials to introduce "the barrier-modification effects" into the formalism. Skyrme forces provide the flex-

ibility of a better comparison of the data, since large number of forces are available that fit different ground state properties of nuclei from different mass regions. Here, we have used the old Skyrme forces SII, SIII, SIV, SKa, SkM and Sly4 having a mild spin-orbit dependence [14, 15] and the very new GSkI and KDE0(v1) forces of Agrawal *et al.* [16, 17], having strong spin-orbit dependence. It would be of interest to see the performance of the new forces, as compared to the old established forces.

Thus, in this Chapter, we study the role of different SEDF-based nuclear interaction potentials on the decay of ^{124}Ce* formed in ^{32}S+^{92}Mo reaction, for checking the relative population of A=4n, α-nuclei like ^{8}Be, ^{12}C, ^{16}O, etc., *w.r.t.* A$\neq$4n, non-α nuclei like ^{6}Be, ^{10}C, ^{14}N, etc., using the DCM. We find that, similar to Blocki *et al.* proximity potential, for all the Skyrme forces, compared to non-α nucleus clusters, the α-nucleus clusters occur at deeper minima in mass fragmentation potential, minimized in charge fragmentation coordinate η_Z, establishing once again that α-nucleus clusters are energetically more favored over non-α nucleus clusters. However, for the best fitted evaporation residue (ER) and IMFs cross sections up to A_2=6, ^{8}Be is shown to be relatively more populated than ^{6}Be for *only* two Skyrme forces [SIII and KDE0(v1)], and ^{12}C more populated than ^{10}C for all Skyrme forces, just as for the case of Blocki *et al.* pocket formula. Note that the DCM calculations include deformation effects up to hexadecapole deformations (β_{2i}, β_{3i}, β_{4i}) with "compact" orientations (θ_{ci}, i=1, 2), for the case of co-planar nuclei [azimuthal angle Φ=0^0, see Fig. 2.1], obtained as per prescription in Ref. [18] for the "hot" fusion process.

We have also applied the ℓ-summed Wong model [19], also discussed in Sec. 2.5 of Chapter 2, to the above data [5], for the choice of nuclear proximity potential of Blocki *et al.* and the above noted two Skyrme forces SIII and KDE0(v1). It may be noted that, whereas DCM deals with each decay fragment x individually such that it determines the evaporation residue cross section σ_{ER} ($= \sum_{x=1}^{4} \sigma_x$), the fusion-fission cross section σ_{ff} ($= 2\sum_{x=5}^{A/2} \sigma_x$), and the non-compound nucleus (nCN)

Table 4.1: ℓ_{max} values and the neck-length parameters ΔR, best fitted to the observed decay channel cross sections of ^{124}Ce* at $E_{c.m.}$=111.29 MeV (T=2.297 MeV), and the complementary heavier fragments, for all the nuclear interaction potentials under consideration. The last column depicts ΔR-value for ^{6}Be and all fragments up to A/2.

Nuclear	ℓ_{max}	ΔR (fm)				
Potential	($\hbar$)	2p	3p	^{4}Li	^{5}Li	^{6}Be-A/2
SII	65	0.67	1.344	1.271	1.168	1.76
SIII	71	0.0575	0.9125	0.73	1.095	1.9375
SIV	64	0.65	1.286	1.31	1.225	1.774
SKa	65	0.585	1.332	1.269	1.14	1.792
SkM	66	0.437	1.245	1.055	0.937	1.664
SLy4	66	0.57	1.21	1.1	0.96	1.536
GSkI	64	0.272	1.189	0.572	0.633	1.6
KDE0(v1)	64	0.68	1.573	1.27	1.105	1.973
Blocki *et al.*	72	0.15	0.793	0.575	0.37	1.0

cross section σ_{nCN} calculated due to the quasi-fission process (σ_{qf}), and their sum, the total fusion cross section σ_{fusion}, in the Wong model, only the total fusion cross section, σ_{fusion}, is determined in terms of the barrier characteristics of the *entrance channel* nuclei. Thus, in DCM, the barrier modification is an inbuilt property via the neck-length parameter ΔR but in the (ℓ-summed) extended-Wong model it is taken care via the small, but important ℓ-dependence of the barrier and the same could also be introduced empirically. Apparently, the (ℓ-summed) extended-Wong model gives only the total fusion cross section and the DCM gives this as well as the details of processes (ER, ff and nCN) comprising the total fusion cross-section. Note that the extended-Wong model for the entrance channel is the same as the DCM(P_0=1), used for calculating the quasi-fission cross section σ_{qf}. This work is published [20] and is also presented at 59^{th} Department of Atomic Energy (DAE) Symposium on Nuclear Physics held at Varanasi, India [21].

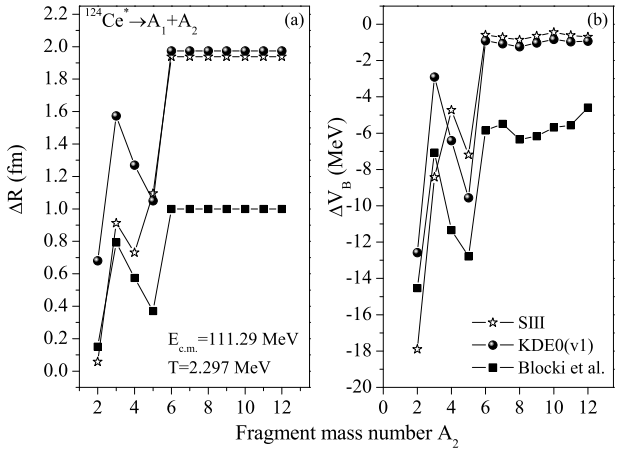

Figure 4.1: Variation of: (a) neck-length parameter ΔR with A_2 for chosen two Skyrme forces and the Blocki *et al.* nuclear potential, and (b) barrier lowering parameter ΔV_B with A_2 for the ℓ_{max} value of each chosen nuclear potential, for the decay of ^{124}Ce* formed in ^{32}S+^{92}Mo reaction at $E_{c.m.}$=111.29 MeV. Note that only a few points were plotted in Fig. 3.11 for Blocki *et al.* nuclear potential [1].

4.2 Calculations and discussion of the results

As already mentioned in the Introduction, we have extended here our study of the decay of CN ^{124}Ce*, formed in ^{32}S+^{92}Mo reaction at an $E_{c.m.}$=111.29 MeV, to the use of various nuclear interaction potentials derived from SEDF based on semiclassical ETF method, and compared with our earlier results [1, 2] of pocket formula of Blocki *et al.* for nuclear proximity potential. Different Skyrme forces give different barrier characteristics, and hence are used to fit the available data on fusion cross-section. For ^{124}Ce*, the relative cross sections of various ERs (A≤4, Z≤2) and IMFs (5≤A≤10, 3≤Z≤6) are observed *w.r.t.* ^{4}Li, and for their use in the DCM, we have fitted for different nuclear interaction potentials, the two LPs (2p and 3p) and two IMFs (^{5}Li and ^{6}Be) cross sections in order to predict the behavior of the relative cross sections of A=4n (^{8}Be and ^{12}C, etc.) and A≠4n (^{6}B and ^{10}C, etc.) clusters at a fixed temperature T=2.297 MeV, referring to experiment of Ref. [5]. Table 4.1 shows the best fitted ℓ_{max} values and the neck-length parameter ΔR for A_2=2-6 on DCM, using all the nuclear interaction potentials under consideration. Note, ℓ_{max} values are close to each other for all the forces, and the ΔR values stay

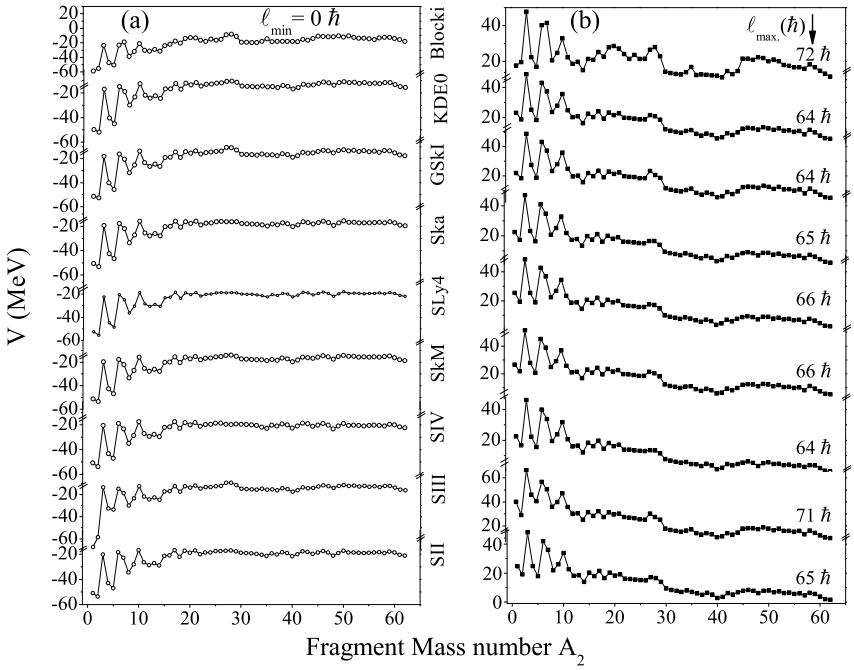

Figure 4.2: Mass fragmentation potential $V(A_2)$, minimized in charge fragmentation coordinate η_Z, for the decay of ^{124}Ce* formed in ^{32}S+^{92}Mo reaction at $E_{c.m.}$=111.29 MeV for various Skyrme forces and proximity potential due to Blocki *et al.*. Fig. 1(a) is for ℓ_{min}=0 and Fig. 1(b) for ℓ_{max} values of Table 4.1. Some energetically favored fragments are replaced by ones of topical interest from the experiment point of view. The various minimized fragments for all the forces are 1n, 2p, 3p, ^{4}Li, ^{5}Li, ^{6}Be, ^{7}Be (^{7}B for Blocki *et al.*), ^{8}Be, ^{9}Be (^{9}B for Blocki *et al.* and for all forces at ℓ_{max} values), ^{10}C, ^{11}C, ^{12}C, at the two ℓ's.

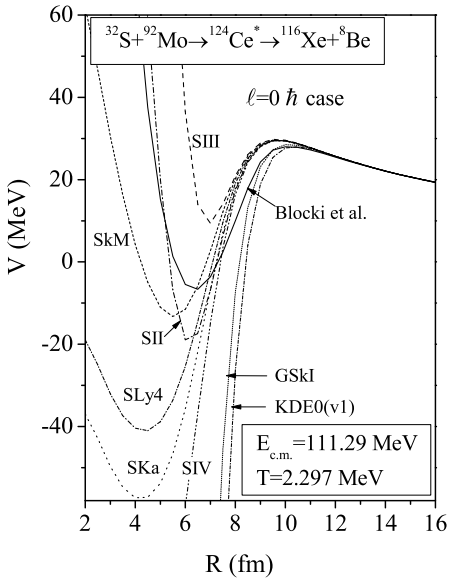

Figure 4.3: Interaction potentials V(R) for ^{116}Xe+^{8}Be decay of ^{124}Ce* formed in ^{32}S+^{92}Mo reaction at $E_{c.m.}$=111.29 MeV, for ℓ=0 case, using various Skyrme forces and Blocki *et al.* pocket formula for nuclear interaction part of potential.

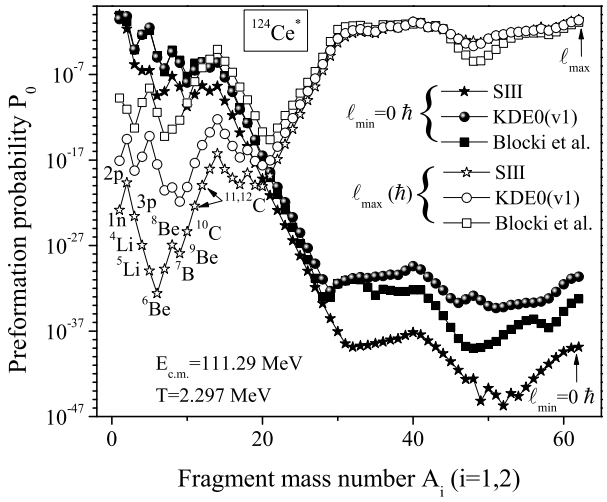

Figure 4.4: Preformation probability P_0 as a function of light fragment mass number A_2 for ^{124}Ce* formed in ^{32}S+^{92}Mo reaction at $E_{c.m.}$=111.29 MeV, using Skyrme forces SIII, KDE0(v1) and proximity potential due to Blocki *et al.*, for ℓ_{min} and ℓ_{max} values.

within the limits of nuclear proximity of < 2 fm.

The neck-length ΔR is the only parameter of the model used to fit the data (Table 4.1), whose variation with light fragment mass number A_2 is illustrated in Fig. 4.1(a) for some selected three nuclear forces. We notice that different nuclear interactions result in a similar functional dependence for $\Delta R(A_2)$. The increase in ΔR means a decrease of reaction time, i.e., the reaction becomes more prompt. Then, by definition, the barrier lowering parameter ΔV_B decreases, which is presented in Fig. 4.1(b). For instance, say, for KDE0(v1) force, the increase in ΔR for 3p (w.r.t. 2p) means that 3p decay is relatively more prompt, and ΔV_B is smaller. The same argument applies to decreased ΔR for mass 4 and 5 fragments. Note, for KDE0(v1), ΔR's are highest, and hence ΔV_B's are about the smallest. It may be reminded that at sub-barrier energies, barrier-modification or barrier-lowering is the only possible explanation to account for the fusion hinderance phenomenon in heavy ion reactions [25–27].

Fig. 4.2 shows the calculated fragmentation potential $V(A_2)$, A_2 being the mass number of light fragment, for the decay of CN ^{124}Ce* at $E_{c.m.}$=111.29 MeV, using the

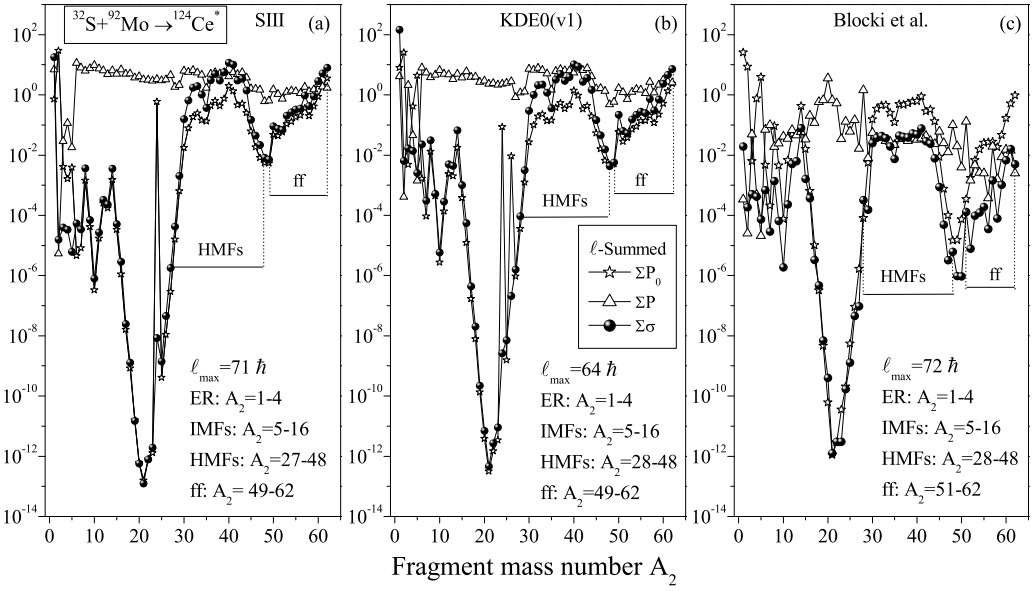

Figure 4.5: The ℓ-summed fragment preformation probability P_0, the penetrability P and the decay channel cross section σ as a function of the light fragment mass number A_2 for compound system ^{124}Ce* formed in ^{32}S+^{92}Mo reaction at $E_{c.m.}$=111.29 MeV, for Skyrme forces SIII and KDE0(v1), compared with the results of Blocki *et al.* potential.

best fitted ΔR-values for eight Skyrme forces, compared with the potential due to Blocki *et al.* used in our earlier work [1], illustrated for ℓ_{min}=0 and ℓ_{max} value from Table 4.1. We notice that all the chosen forces behave alike since, for all of them, the same fragments contribute to the decay processes, namely, the light particles 2p, 3p, ^{4}Li and the IMFs ^{5}Li, ^{6}Be, ^{7}Be, ^{8}Be, ^{9}Be (^{9}B at ℓ_{max} value for all forces), ^{10}C, ^{11}C and ^{12}C, corresponding to the observed heavy residues. Note, for Blocki *et al.* pocket formula ^{7}B and ^{9}B occur, instead of ^{7}Be and ^{8}Be, respectively, at both ℓ_{min} and ℓ_{max} values. The interesting result is that, similar to the case of Blocki *et al.* proximity potential, ^{8}Be and ^{12}C occur at deeper minima, as compared to ^{6}Be and ^{10}C, for all the Skyrme forces, establishing that in the decay of ^{124}Ce*, independent of nuclear interaction potential, the A=4n, α-nucleus structure is preferred over the A≠4n, non-α nucleus structure. Also, the LPs and IMFs are energetically more favorable at lower ℓ values and the ff at higher ℓ values.

Fig. 4.3 shows the comparison of interaction potentials V(R) for CN ^{124}Ce*,

Table 4.2: DCM calculated relative cross sections σ(Channel)/$\sigma(^4\text{Li})$ for LPs, IMFs, HMFs, and ff in the decay of $^{124}\text{Ce}^*$, compared with the experimental data $\sigma^{Expt.}$ at E_{Lab}=150 MeV ($\equiv E_{c.m.}$=111.29 MeV, T=2.297 MeV) for $^{32}\text{S}+^{92}\text{Mo}$ reaction [5]. The (total) fusion cross section $\sigma_{Fusion}/\sigma(^4\text{Li})$, the CN formation probability P_{CN} for the measured data (=ER+IMFs), and CN survival probability P_{surv} based on DCM predicted ff data are also given.

Decay Channel	σ(Channel)/$\sigma(^4\text{Li})$									
	SII	SIII	SIV	SKa	SkM	SLy4	GSkI	KDE0(v1)	Blocki	Expt.
					ERs ($A_2 = 1-4$)					
2p	0.46	0.46	0.46	0.45	0.46	0.46	0.46	0.46	0.44	0.46
3p	1.19	1.19	1.19	1.19	1.19	1.19	1.19	1.19	1.19	1.19
^{4}Li	1	1	1	1	1	1	1	1	1	1
					IMFs ($A_2 = 5-13$)					
^{5}Li	0.18	0.18	0.18	0.18	0.18	0.18	0.18	0.18	0.18	0.18
^{6}Be	1.63	1.63	1.65	1.63	1.63	1.63	1.63	1.63	1.63	1.63
^{7}Be	7×10^{-3}	1.04	5×10^{-3}	9.8×10^{-3}	0.12	8.37×10^{-3}	1.28×10^{-2}	2.19×10^{-2}	0.07	0.36
^{8}Be	0.54	109	0.34	0.82	1.06	0.571	0.94	2.23	3.28	-
^{9}Be	2×10^{-3}	0.18	9×10^{-4}	3.23×10^{-3}	4.8×10^{-3}	1.5×10^{-3}	5.2×10^{-3}	6.4×10^{-3}	0.15	-
^{10}C	1.4×10^{-4}	2.36×10^{-2}	8.9×10^{-5}	2.14×10^{-4}	3.27×10^{-4}	1.67×10^{-4}	3.1×10^{-4}	4.3×10^{-4}	4×10^{-3}	0.24
^{11}C	4×10^{-3}	0.81	1.47×10^{-3}	8.6×10^{-3}	1.5×10^{-2}	6.32×10^{-3}	1.46×10^{-2}	2.05×10^{-2}	0.55	-
^{12}C	0.06	9.91	0.02	0.14	0.25	0.095	0.18	0.36	12.25	-
^{13}C	0.044	6.97	0.019	0.10	0.22	0.066	0.13	0.32	15.1	-
					Summed HMFs					
$\sum_x^y$HMF	363	1.57×10^6	174	690	2110	1140	1420	3580	1270	-
(x-y)	(29-48)	(27-48)	(29-48)	(29-48)	(28-48)	(29-48)	(28-48)	(28-48)	(28-48)	-
					Summed ff					
$2\sum_x^y$ff	106	1.18×10^6	44.3	216	831	365	629	2503	147	-
(x-y)	(49-62)	(49-62)	(49-62)	(49-62)	(49-62)	(49-62)	(49-62)	(49-62)	(51-62)	-
					(Total) Fusion cross section (relative to ^{4}Li)					
$\frac{\sigma_{fusion}}{\sigma_{4_{Li}}}$	475.07	2.75×10^6	223.6	913.51	2951.26	1511.7	2056.86	6095.32	1644.63	-
					P_{CN} for the measured data					
P_{CN}	0.883	1.0	0.886	0.883	0.905	0.883	0.884	0.886	0.882	-
					P_{surv} for DCM predicted fusion-fission					
P_{surv}	0.006	0.96×10^{-6}	0.012	0.003	0.001	0.002	0.001	0.43×10^{-3}	0.002	-

illustrated for the decay ^{116}Xe+^{8}Be at $E_{c.m.}$=111.29 MeV, for various Skyrme forces and the Blocki *et al.* nuclear proximity potential. We notice that, similar to Blocki *et al.*, the short-range potential pocket is formed for all old forces, namely, SII, SIII, SIV, SKa, SkM and SLy4 (for SIV, the pocket is much deeper, rather deepest; not shown here), and the new forces GSkI and KDE0(v1) are the ever-increasingly attractive forces. Also, the barrier characteristics, i.e., barrier height V_B, position R_B and curvature $\hbar\omega$, are strongly force dependent, i.e., are different for different Skyrme forces. On the basis of barrier height V_B, however, in addition to Blocki *et al.* pocket formula, two other groups could be identified: one consisting of all the old Skyrme forces, and the other of two new Agrawal *et al.* forces. The force SIII has the highest and KDE0(v1), the lowest barrier. Furthermore, we shall see later (Table 4.2 and Fig. 4.6) that SIII and KDE0(v1) are the *only* two Skyrme forces that result in a predominant α-nucleus structure. Therefore, we have chosen to present our results for SIII and KDE0(v1) (one Skyrme force from each group), compared with Blocki *et al.* pocket formula.

The results of fragmentation potential $V(A_2)$ in Fig. 4.2 can be better understood in terms of preformation factor P_0 since it gives the dynamical yields of fragments. Fig. 4.4 shows a plot of $P_0(A_2)$ for SIII and KDE0(v1) forces and Blocki *et al.* potential, at ℓ_{min} and ℓ_{max} values. We notice that lower ℓ values contribute to LPs and IMFs (larger yields) and the higher ℓ values to ff region. Interestingly, P_0 for all the three forces give rise to a similar region for the ff process. For the lighter mass region, evidently A=4n, α-nuclei like ^{8}Be and ^{12}C are relatively more strongly preformed as compared to A$\neq$4n, non-α nuclei like ^{6}Be and ^{10}C, indicating preferred preformation for α-nuclei.

Fig. 4.5 presents the ℓ-summed P_0, P and channel cross section σ plotted as a function of A_2 for the three chosen forces (Skyrme forces SIII and KDE0(v1), and Blocki *et al.* potential). Apparently, the ℓ-summed P contributes only to the magnitude, and the ℓ-summed σ follow the behavior of ℓ-summed P_0, containing the

structure effects of CN. Thus, in addition to the observed ER, for cross sections of similar orders, the IMFs window is shown extended up to A_2=16, though the data is observed up to ^{10}C only, and a new decay region of heavy mass fragments (HMFs) of A_2=27-48 or 28-48, plus a near-symmetric and symmetric fission fragments A_2=49-62 or 51-62 are clearly indicated, which on including the complementary heavy fragments result in the ff region of $(A/2)\pm12$. The same result is presented in Table 4.2, where we have shown the ER, IMFs (up to A_2=13), and the summed HMFs and ff cross-sections, relative to ^{4}Li, for all the eight chosen Skyrme forces and the Blocki *et al.* potential, compared with experimental data [5]. Also, the (total) fusion cross-section, relative to ^{4}Li, $\frac{\sigma_{fusion}}{\sigma_{^4Li}}$, and the CN fusion probability P_{CN} [22] for the measured data (ER and IMFs), and CN survival probability P_{surv} [23] against (the DCM estimated) ff process are calculated and given in Table 4.2. Apparently, some of the calculated (relative) fusion cross sections $\frac{\sigma_{fusion}}{\sigma_{^4Li}}$ are very large, and the survival probability P_{surv} very small due to the predicted large ff component. On the other hand, the P_{CN} is close to unity in almost all cases (Skyrme forces and Blocki *et al.* pocket formula) since the empirically determine σ_{nCN} is, in general, very small.

Furthermore, Fig. 4.6 shows the DCM calculated relative cross section for the three chosen forces, compared with the experimental data [5] given relative to ^{120}Cs ($\equiv^4$Li). Note that ^{8}Be, ^{9}B, ^{11}C and ^{12}C decays are not observed in this experiment. Also, it may be reminded that the energetically favored fragments for Blocki *et al.* proximity potential are ^{7}B and ^{9}B, whereas for all the considered Skyrme forces, these are ^{7}Be and ^{9}Be. Evidently, for the best fitted 2p, 3p, ^{5}Li and ^{6}Be cross-sections, the A=4n, α-nuclei like ^{8}Be and ^{12}C are shown to be relatively more populated than the A$\neq$4n, non-α nuclei like ^{6}Be and ^{10}C for all cases, in agreement with the results of the ground-state (T=0) decays [3, 4, 9].

Finally, Fig. 4.7 shows the extended-Wong model based, θ_i-integrated cross

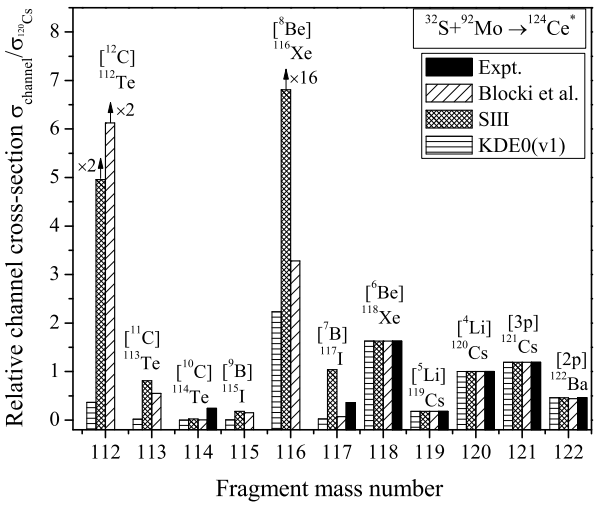

Figure 4.6: Comparison of DCM calculated relative cross sections of various heavy residues *w.r.t.* ^{120}Cs for two Skyrme forces compared with the proximity potential due to Blocki *et al.* and the measured data [5]. The corresponding light product is also shown in the bracket. It is relevant to note that the minimized fragments for the Skyrme forces are ^{7}Be and ^{9}Be whereas the same for Blocki *et al.* proximity potential are ^{7}B and ^{9}B. No error bars are available for the measured data.

section summed up to angular momentum ℓ, plotted as a function of ℓ itself using nuclear proximity potential due to Blocki *et al.* and the SIII and KDE0(v1) Skyrme forces, for ^{32}S+^{92}Mo reaction at $E_{c.m.}$=111.29 MeV. Note, Wong model gives only the total fusion cross-section, and not the cross sections of the contributing processes (ER, IMFs, HMFs and ff), whereas the DCM gives the decay/ fusion cross section of each fragment and hence of various decay processes, and, of course, their sum, the total fusion cross-section. Since the measured cross section for the system under study is given relative to ^{120}Cs ($\equiv^{4}$Li) fragment, and not the absolute cross-sections, the extended-Wong model predictions could not be compared with the measured data. However, interestingly, we notice that the ℓ_{max} values calculated for this system by using DCM and extended-Wong model, lie close to each other (compare ℓ_{max} in Table 4.1 for DCM with ℓ_{max} values given in Fig. 4.7 for extended-Wong model). Also, the order of fusion cross section predicted by extended-Wong model (900-1400 mb, see Fig. 4.7) is similar to that of the relative fusion cross sections in Table 4.2 for many Skyrme forces and the Blocki *et al.* nuclear potential. Thus,

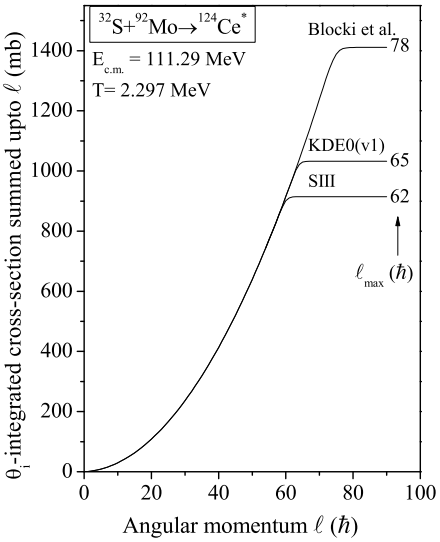

Figure 4.7: Based on the extended-Wong model, the θ_i-integrated (for Φ=0^0 case) cross section summed up to angular momentum ℓ, plotted as a function of ℓ itself for ^{32}S+^{92}Mo reaction at $E_{c.m.}$=111.29 MeV, using nuclear proximity potential due to Blocki *et al.* and the SIII and KDE0(v1) Skyrme forces.

extended-Wong model predictions could be useful for planning new experiments in the mass region of CN under study.

4.3 Summary

In this Chapter, the earlier work of the decay of ^{124}Ce* formed in ^{32}S+^{92}Mo reaction at a beam energy of 150 MeV (T=2.297 MeV), using in DCM the pocket formula of Blocki *et al.* for nuclear proximity potential given in Chapter 3, is extended to the use of various other nuclear interaction potentials derived from the ETF-based semiclassical SEDF method. Both the old and new Skyrme forces are considered. It is interesting to find that the only parameter of the model, neck-length ΔR, remains within $\sim$2 fm, the range of validity of proximity potential used here. For the best fitted ΔR of two LPs (2p and 3p) and two IMFs (^{5}Li and ^{6}Be), similar to what was obtained earlier for use of pocket formula of Blocki *et al.*, the relative populations of ^{6}Be *vs.* ^{8}Be, and that of ^{10}C *vs.* ^{12}C show that the CN ^{124}Ce* decays preferentially via A=4n, α-nucleus clusters, as compared to A$\neq$4n, non-α nucleus clusters, for *only*

SIII and KDE0(v1) Skyrme forces. Considering the cross sections of orders similar to observed ones for ER and IMFs, the IMF-window is shown extended to A_2=16, and a new decay region of HMFs of A_2=27-48 or 28-48 and a near-symmetric and symmetric fission fragments A_2=49-62 or 51-62 are predicted, which on combining with the complementary heavy fragments result in the ff region of $(A/2)\pm12$. Using the predicted (total) fusion cross-section, the CN survival probability P_{surv} comes out to be very small for all the considered nuclear interactions, due to large predicted fusion-fission contribution. However, the CN fusion probability P_{CN} is nearly unity for all nuclear interactions, due to very small empirically estimated non-compound nucleus content, establishing that ^{124}Ce* decay is nearly a pure CN decay.

We have also applied the (ℓ-summed) extended-Wong model of Gupta and collaborators to this reaction, but the calculated total fusion cross sections could not be compared with the measured data since only relative cross sections are given in the experiment. However, the ℓ_{max} values and the order of predicted fusion cross sections for the two models (DCM and extended-Wong model) are similar, and thus could be useful in planning further experiments in this mass region.

Bibliography

[1] A. Kaur, S. Chopra, and R. K. Gupta, Phys. Rev. C **89**, 034602 (2014).

[2] A. Kaur, S. Chopra, and R. K. Gupta, Acta Physica Polonica B **45**, 349 (2014).

[3] S. Kumar, D. Bir, and R. K. Gupta, Phys. Rev. C **51**, 1762 (1995).

[4] S. Kumar and R. K. Gupta, Phys. Rev. C **49**, 1922 (1994).

[5] J. Ray, *et al.*, in *Proc. Department of Atomic Energy Symp. on Nucl. Phys.* **57**, 368 (2012); available on line at http://www.sympnp.org/proceedings/57/A93.pdf.

[6] R. K. Gupta, M. Balasubramaniam, R. Kumar, N. Singh, M. Manhas, and W. Greiner, J. Phys. G: Nucl. Part. Phys. **31**, 631 (2005).

[7] R. K. Gupta, Lecture Notes in Physics 818 *Clusters in Nuclei*, ed C. Beck, Vol.I, (Springer Verlag), p.223 (2010).

[8] J. Blocki, J. Randrup, W. J. Swiatecki, and C. F. Tsang, Ann. Phys. (N.Y.) **105**, 427 (1977).

[9] M. K. Sharma, R. K. Gupta, and W. Scheid, J. Phys. G: Nucl. Part. Phys. **26**, L45 (2000).

[10] S. Chopra, A. Kaur, and R. K. Gupta, Phys. Rev. C **91**, 014602 (2015).

[11] R. K. Gupta, D. Singh, R. Kumar, and W. Greiner, J. Phys. G: Nucl. Part. Phys. **36**, 075104 (2009).

[12] R. Kumar, M. K. Sharma, and R. K. Gupta, Nucl. Phys. A **870-871**, 42 (2011).

[13] D. Jain, R. Kumar, M. K. Sharma, and R. K. Gupta, Phys. Rev. C **85**, 024615 (2012).

[14] M. Brack, C. Guet, and H.-B. Hakansson, Phys. Rep. **123**, 275 (1985).

[15] J. Friedrich and P.-G. Reinhardt, Phys. Rev. C **33**, 335 (1986).

[16] B. K. Agrawal, S. K. Dhiman, and R. Kumar, Phys. Rev. C. **73**, 034319 (2006).

[17] B. K. Agrawal, S. Shlomo, and V. K. Au, Phys. Rev. C. **72**, 014310 (2005).

[18] R. K. Gupta, M. Manhas, and W. Greiner, Phys. Rev. C **73**, 054307 (2006).

[19] R. Kumar, M. Bansal, S. K. Arun, and R. K. Gupta, Phys. Rev. C **80**, 034618 (2009).

[20] A. Kaur, S. Chopra, and R. K. Gupta, Phys. Rev. C. **91**, 064601 (2015).

[21] A. Kaur and R. K. Gupta, in *Proceedings of 59$^\sharp$h Department of Atomic Energy (DAE) Symp. on Nucl. Phys.* **59** (2014) p. 398; available on line at http://www.sympnp.org/proceedings/59/B45.pdf.

[22] A. Kaur, S. Chopra, and R. K. Gupta, Phys. Rev. C **90**, 024619 (2014).

[23] S. Chopra, A. Kaur, and R. K. Gupta, Phys. Rev. C **91**, 034613 (2015).

[24] D. L. Hill and J. A. Wheeler, Phys. Rev. **89** (1959) 1102; T. D. Thomas, Phys. Rev. **116**, 703 (1959).

[25] S. K. Arun, R. Kumar, and R. K. Gupta, J. Phys. G: Nucl. Part. Phys. **36**, 085105 (2009).

[26] S. Misicu and H. Esbensen, Phys. Rev. Lett. **96**, 112701 (2006).

[27] S. Misicu and H. Esbensen, Phys. Rev. C **75**, 034606 (2007).

Chapter 5

Non-compound nucleus effects in measured decay channels of ^{217}At* formed in neutron-rich exotic ^{9}Li+^{208}Pb reaction and its synthesis within the dynamical cluster-decay model

5.1 Introduction

In Chapters 3 and 4, we have studied the decay of proton-rich compound nucleus (CN) ^{124}Ce*. In this chapter, we extend the application of the dynamical cluster-decay model (DCM) [1] to the neutron-rich systems. In a recent work of Gupta and Collaborators [2], it is shown that, within the DCM [1,2], σ_{fus} can be obtained quite accurately as a pure CN process at a fixed value of the neck-length ΔR (the only parameter in the DCM) for various reactions formed with the *same* loosely bound projectile on different targets at a chosen incident laboratory energy, E_{lab}.

The reactions considered in this study [2] are with neutron-rich ^{7}Li and ^{9}Be, and neutron-deficient ^{7}Be projectiles on various targets forming compound nuclei in the mass region $A_{CN} \sim 30 - 200$. It is relevant to remind here that, in DCM, the dynamical collective mass motion of preformed light particles (LPs, $A \leq 4$, referred to as evaporation residues ER) and fusion-fission ff fragments (or clusters), through the modified interaction potential barrier, are treated on the same footing, where the modification of the barrier is introduced via empirical ΔR with corresponding modified barrier heights ΔV_B for such reactions being almost of the same order at, respective, ℓ_{min} or ℓ_{max} value.

^{9}Li projectile, chosen for the present study, is also a very neutron-rich ($N = 2Z$) nucleus, with a significant amount of neutron skin (=0.48 fm in a neutron radius of 2.59 fm [3]), whose fusion excitation function at near- and sub-barrier energies are recently measured for only two neutron-rich ^{70}Zn [4] and ^{208}Pb [5] target nuclei. Earlier experimental studies of the use of ^{9}Li projectile were made at intermediate energies (80 MeV/ nucleon), namely of the elastic scattering of ^{9}Li [6] and total interaction cross section of ^{9}Li on intermediate mass targets, such as C, Al, Cu, Sn and Pb [7]. Also, the fusion of ^{9}Li with Si at 11.2A - 15.2A MeV, and at a projectile energy of 36 MeV with ^{209}Bi were studied at RIKEN [8,9], measuring the evaporation residues and any associated neutrons, but no fusion cross sections were measured. In the following, we analyze some of these ^{9}Li based reactions at near- and above-barrier energies, where the reaction dynamics of ^{9}Li+^{208}Pb$\rightarrow ^{217}$At* is studied in some detail. Note that in most of the above noted reactions at intermediate energies, the isotopic mass of the target is not known, and that studying the reaction with ^{9}Li as a projectile will help us understand the interactions with other neutron-rich nuclei like ^{11}Li since ^{9}Li is known to be the core of 2n-halo nucleus ^{11}Li. Apparently, breakup effects could play a significant role on the fusion of halo-nucleus ^{11}Li, as is explicitly shown, for example, by Takigawa *et al.* [10] by incorporating the effect of breakup in ^{11}Li-induced reactions via a local dynamic polarization potential. Note,

however, that such effects do not come in to play in beams of neutron-rich exotic nucleus like ^{9}Li used here.

For the ^{9}Li+^{208}Pb reaction [5], the fusion excitation function is measured for near-barrier projectile center-of-mass energies $E_{c.m.}$=23.9 to 43.0 MeV. At some nine of these $E_{c.m.}$'s, the evaporation residue cross sections σ_{xn} are measured for x=3-6 neutrons emission from the CN ^{217}At*, i.e., the isotopic yields for heavy mass residues $^{211-214}$At are measured, which are found to be in good agreement with the predictions of a statistical model code HIVAP [11]. The only other theoretical calculation available for this reaction is that of Takigawa *et al.* [10] who simply assumed the validity of the Wong formula [12]. The measured fusion excitation function shows evidence for substantial sub-barrier fusion enhancement and a suppression (hindrance) of the above-barrier cross sections relative to Takigawa *et al.* [10] and the coupled channels (CCFULL code) [5] calculations. Another interesting result of this work is that fusion-fission cross section σ_{ff} is considered to be small, taken zero [5], since σ_{ff} $\sim$1% of total fusion cross section $\sigma_{fus}^{Expt.}$ ($\sigma_{fus}^{Expt.} = \sigma_{ER} + \sigma_{ff}$), with σ_{ER} ($= \sum_{x=3}^{4} \sigma_{xn}$) as the measured yield of the corresponding heavy evaporation residues (^{212,213}Rn) formed in a similar reaction ^{7}Li+^{209}Bi at 34.95 MeV, which further compare nicely with the earlier measurements of Dasgupta *et al.* [13] for the same reaction.

In this paper, using the DCM, we first focus our attention on the ^{9}Li+^{208}Pb reaction with a view to extend our earlier work of the loosely bound projectile on different targets at the same beam energy [2], i.e., calculate the total fusion cross sections σ_{fus} for a given E_{lab} energy at a fixed value of the neck-length ΔR, using ^{9}Li as a projectile on ^{208}Pb target and various isotopes of other targets (Al, Cu, Zn and Sn) from the intermediate energy regime of earlier experiments. In the ^{9}Li+^{208}Pb experiment [5], however, the decay channels cross sections σ_{xn}, for x-neutrons xn, x=3-6, are measured which allow us to fit each channel individually, keeping in mind that σ_{ff} is negligibly small. This calls for the possibility of hindrance/ en-

hancement phenomenon due to the presence of other processes like quasi-fission (qf), incomplete fusion (ICF), deep inelastic collisions (DIC), etc., which we refer to as non-compound nucleus (nCN) effects, estimated empirically from the calculated and measured fusion cross sections:

$$\sigma_{nCN} = \sigma_{fus}^{Expt.} - \sigma_{fus}^{Cal.}.$$

Then, the total fusion cross-section is given as the sum of σ_{CN} and σ_{nCN}, as

$$\sigma_{fus} = \sigma_{ER} + \sigma_{ff} + \sigma_{nCN} = \sigma_{CN} + \sigma_{nCN}$$

where $\sigma_{fus}^{Cal.} \equiv \sigma_{CN}$.

Furthermore, the calculated fragmentation potential $V(\eta)$, with $\eta = (A_1 - A_2)/(A_1 + A_2)$, for the CN ^{217}At* formed in ^{9}Li+^{208}Pb reaction, i.e., the fragmentation process ^{9}Li+^{208}Pb$\rightarrow^{217}$At$^* \rightarrow A_1 + A_2$ at a fixed ΔR, or relative separation $R = R_1 + R_2 + \Delta R$, can also be used to identify the various "cold" target + projectile (t,p) combinations referring to potential energy minima for the synthesis of ^{217}At* on the basis of the DCM or its founding theory QMFT, the quantum mechanical fragmentation theory [14]. Then, the chosen "cold" (t,p) combinations are optimised for largest cross section in terms of their calculated interaction barriers and interaction radii. The role of binding energy of ^{9}Li enters here via $V(\eta)$, defined as a sum of the binding energies of two fragments and the relevant Coulomb, nuclear and centrifugal potentials. A brief report of this work was presented at the 2015 DAE-BRNS Nucl. Phys. Symposium [15].

5.2 Calculations and discussion of the results

As already mentioned in the Introduction, for the ^{9}Li+^{208}Pb$\rightarrow^{217}$At* reaction, fusion excitation function is measured for x-neutrons (xn, x=3-6) emission at some nine

$E_{c.m.}$'s, in the energy range 23.9 to 43.0 MeV. Specifically, emission of 1n and 2n are not observed, and that, depending on the $E_{c.m.}$ value, σ_{xn} for some other x-values are also zero. In other words, σ_{xn} for only some of the x=3-6 neutrons are observed, and the light-particles evaporation residue cross section $\sigma_{ER} = \sum_{x=3}^{6} \sigma_{xn}$, the sum of measured σ_{xn}, and that, in the absence of nCN effects, $\sigma_{fus}^{Expt.} \equiv \sigma_{ER}$ since here the fusion-fission cross section σ_{ff} is also taken to be zero [5].

5.2.1 σ_{fus} for neutron-rich ^{9}Li projectile on ^{208}Pb and other targets using fixed neck-length ΔR

In this sub-section, using the DCM, we first calculate (total) fusion cross section σ_{fus} for ^{9}Li+^{208}Pb reaction at six of the nine incident $E_{c.m.}$ (=23.9, 28.5, 33.4, 38.1, 40.6 and 43.0 MeV), for a fixed neck-length parameter ΔR at each $E_{c.m.}$, given as the sum of all decay channels (here, 1-6 neutrons) and compare our results with measured $\sigma_{fus}^{Expt.}$ ($\equiv \sigma_{ER}$, refer to Table 5.1 and 5.2, Cal.1). As a next step, we extend this study of neutron-rich ^{9}Li induced reaction to other target nuclei at a fixed E_{lab} energy, and the same fixed value of the neck-length parameter ΔR (refer to Table 5.3).

Figure 5.1 illustrates the mass fragmentation potential $V(A_2)$, minimized in charge fragmentation coordinate η_Z, for the decay of CN ^{217}At* formed in ^{9}Li+^{208}Pb reaction at $E_{c.m.}$=28.5 MeV (T=1.145 MeV), and at ℓ_{min} and ℓ_{max} values, for the fixed ΔR=1.556 fm. Some of the minimized fragments in mass region A_2=1-6 are replaced by fragments of interest from the point of view of measured decay channels (here 1n-6n). For example, the minimized fragments at ℓ_{min} and ℓ_{max} values corresponding to A_2= 4, 5 and 6 are ^{4}H, ^{5}He and ^{6}Li, respectively, which are replaced by the binding energies of observed 4n, 5n and 6n fragments. Using this potential of Fig. 5.1 and the scattering potential of like in Fig. 5.13, the preformation probability P_0 and penetrability P are calculated whose plots as a function of ℓ,

Table 5.1: The DCM calculated (total) fusion cross section σ_{fus} at a fixed neck-length parameter ΔR (Cal.1) and for each decay channel fitted as CN and nCN contributions with different ΔR's (Cal.2) at various center-of-mass energies $E_{c.m.}$'s. Since here σ_{ff} is negligibly small, σ_{ER} $(=\sum_{x=1}^{6}\sigma_{xn})\cong\sigma_{fus}$. The experimental data is from Ref. [5].

	Cal.1 (Fixed ΔR)		Cal.2 (Channel cross section Fitted ΔR)					
			CN contribution		nCN contribution			
Decay-channel	$\sigma_{fus}^{Cal.1}$ (mb)	σ_{fus}^{Expt} (mb)	ΔR (fm)	$\sigma_{CN}^{Cal.}$ (mb)	σ_{nCN}^{emp} (mb)	ΔR (fm)	$\sigma_{nCN}^{Cal.}$ (mb)	$\sigma_{fus}^{Cal.2}$ (mb)
$E_{c.m.}$=23.9 MeV; T=1.046 MeV								
	(ΔR = 1.246 fm)							
1n	0.615	-	1.0	1.11×10^{-7}	-	-	-	1.11×10^{-7}
2n	2.23×10^{-2}	-	1.0	8.91×10^{-7}	-	-	-	8.91×10^{-7}
3n	2.66×10^{-4}	-	0.2	1.07×10^{-19}	-	-	-	1.07×10^{-19}
4n	2.35×10^{-6}	0.61±0.61	1.839	0.61	0	-	-	0.61
5n	8.32×10^{-9}	-	1.0	1.16×10^{-27}	-	-	-	1.16×10^{-27}
6n	2.25×10^{-11}	-	1.0	7.59×10^{-11}	-	-	-	7.59×10^{-11}
σ_{fus}	0.615	0.61	-	0.61	-	-	-	0.61
$E_{c.m.}$=28.5 MeV; T=1.145 MeV								
	(ΔR = 1.556 fm)							
1n	75.2	-	0.9	3.07×10^{-4}	-	0.1	1.06×10^{-7}	3.07×10^{-4}
2n	2.35	-	0.9	6×10^{-6}	-	0.1	1.18×10^{-8}	6×10^{-6}
3n	3.33×10^{-2}	8.4±1.9	2.02	0.09	8.31	1.1971	8.31	8.4
4n	3.1×10^{-4}	69.3±8.4	2.01	0.74	68.56	1.3475	68.6	69.34
5n	1.35×10^{-6}	-	-0.3	4.18×10^{-22}	-	0.1	1.61×10^{-10}	1.61×10^{-10}
6n	7.83×10^{-9}	-	1.5	2.8×10^{-3}	-	0.1	3.92×10^{-11}	2.8×10^{-3}
σ_{fus}	77.55	77.7±8.6		0.833	76.87		76.91	77.743
$E_{c.m.}$=33.4 MeV; T=1.24 MeV								
	(ΔR = 1.74 fm)							
1n	433	-	1.05	5.02×10^{-3}	-	0.1	1.38×10^{-7}	5.02×10^{-3}
2n	15.4	-	1.0	8.02×10^{-5}	-	0.1	1.69×10^{-8}	8.02×10^{-5}
3n	0.272	-	0.4	6.58×10^{-11}	-	0.1	3.24×10^{-9}	3.24×10^{-9}
4n	2.88×10^{-3}	403±17	2.03	0.819	402.181	1.4949	402	402.819
5n	1.44×10^{-5}	45±7.3	2.0	2.26×10^{-4}	45	1.324	45.2	45.2
6n	1.55×10^{-7}	-	1.7	4.6×10^{-5}	-	0.1	7.33×10^{-11}	4.6×10^{-5}
σ_{fus}	448.6	448±19		0.824	447.181		447.2	448.024
$E_{c.m.}$=38.1 MeV; T=1.327 MeV								
	(ΔR = 1.8121 fm)							
1n	722	-	0.7	8.69×10^{-6}	-	0.1	1.41×10^{-7}	8.69×10^{-6}
2n	29.6	-	1.0	2.47×10^{-5}	-	0.1	1.83×10^{-8}	2.47×10^{-5}
3n	0.643	-	0.0	8.08×10^{-14}	-	0.1	3.63×10^{-9}	3.63×10^{-9}
4n	8.6×10^{-3}	218±22	2.02	1.04	216.96	1.4475	217	218.04
5n	5.34×10^{-5}	534±29	2.0	2.2×10^{-4}	534	1.5369	534	534
6n	6.19×10^{-7}	-	1.7	3.46×10^{-10}	-	0.1	8.75×10^{-11}	3.46×10^{-10}
σ_{fus}	752.243	752±37		1.04	750.96		751	752.04

Table 5.2: Table 5.1 ..... continued

	Cal.1 (Fixed ΔR)		Cal.2 (Channel cross section Fitted ΔR)					
			CN contribution		nCN contribution			
Decay-channel	$\sigma_{fus}^{Cal.1}$ (mb)	σ_{fus}^{Expt} (mb)	ΔR (fm)	$\sigma_{CN}^{Cal.}$ (mb)	σ_{nCN}^{emp} (mb)	ΔR (fm)	$\sigma_{nCN}^{Cal.}$ (mb)	$\sigma_{fus}^{Cal.2}$ (mb)
$E_{c.m.}$=40.6 MeV; T=1.371 MeV								
	(ΔR = 1.8398 fm)							
1n	844	-	0.9	9.92×10^{-5}	-	0.1	1.63×10^{-7}	9.92×10^{-5}
2n	36.9	-	1.0	2.53×10^{-5}	-	0.1	2.14×10^{-8}	2.53×10^{-5}
3n	0.884	-	0.0	9.33×10^{-14}	-	0.1	4.51×10^{-9}	4.51×10^{-9}
4n	1.18×10^{-2}	133±17	2.02	1.03	131.97	1.4057	132	133.03
5n	7.77×10^{-5}	620±43	2.0	2.1×10^{-4}	620	1.5537	620	620
6n	9.56×10^{-7}	129±56	2.0	2.93×10^{-5}	129	1.4188	129	129
σ_{fus}	881.784	882±73		1.03	880.97		881	882.03
$E_{c.m.}$=43 MeV; T=1.411 MeV								
	(ΔR = 1.8507 fm)							
1n	881	-	1.0	3.36×10^{-4}	-	0.1	1.47×10^{-7}	3.36×10^{-4}
2n	41.6	-	1.0	2.86×10^{-5}	-	0.1	1.95×10^{-8}	2.86×10^{-5}
3n	1.12	-	0.0	1.17×10^{-13}	-	0.1	4.03×10^{-9}	4.03×10^{-9}
4n	1.74×10^{-2}	72±8.4	2.03	1.07	70.93	1.3634	70.9	71.97
5n	1.29×10^{-4}	669±23	2.0	2.17×10^{-4}	669	1.5708	669	669
6n	1.58×10^{-6}	182±29	2.01	4×10^{-5}	182	1.4545	182	182
σ_{fus}	923.7374	923±39		1.07	921.93		921.9	922.97

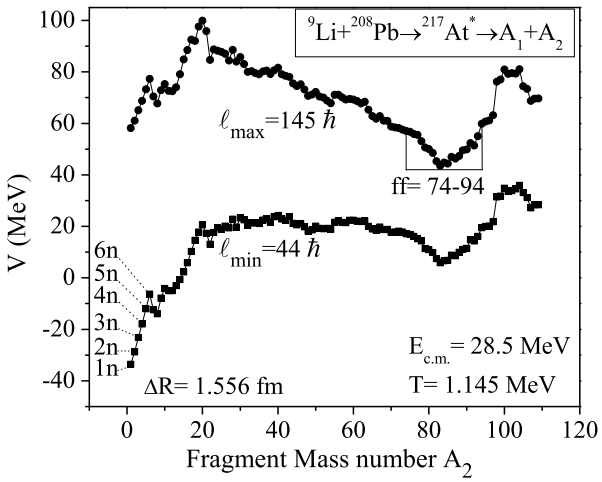

Figure 5.1: Mass fragmentation potential $V(A_2)$, minimized in charge fragmentation coordinate η_Z, for the decay of ^{217}At* formed in ^{9}Li+^{208}Pb reaction at $E_{c.m.}$=28.5 MeV (T=1.145 MeV), and at ℓ_{min} and ℓ_{max} values, for a fixed ΔR=1.556 fm. The most favored fragments for A_2=1-6 are replaced by fragments of topical interest (here 1n-6n).

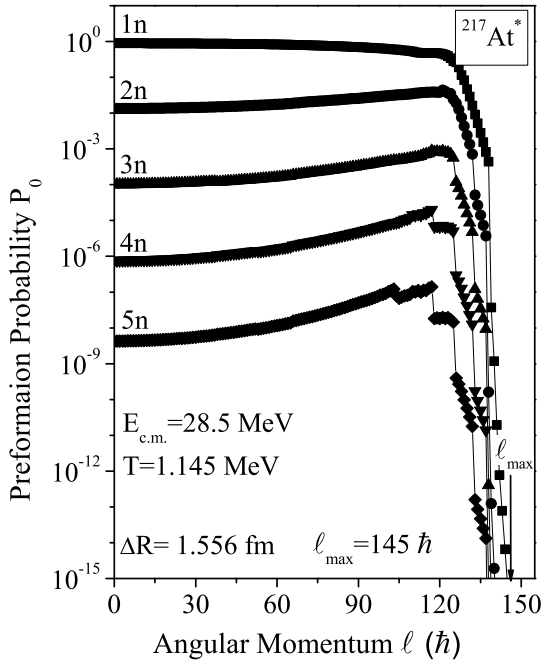

Figure 5.2: Preformation probability P_0 as a function of angular momentum ℓ for 1n-5n decays of ^{217}At* formed in ^{9}Li+^{208}Pb reaction at $E_{c.m.}$=28.5 MeV, as per fragmentation potential in Fig. 5.1.

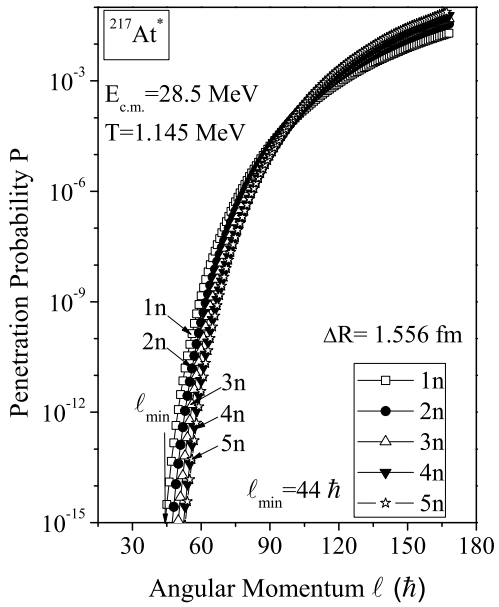

Figure 5.3: Same as for Fig. 3, but for penetration probability P.

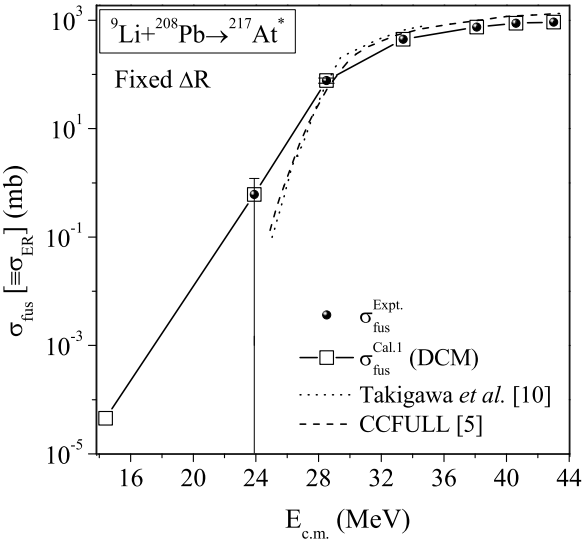

Figure 5.4: The DCM calculated σ_{fus} (=σ_{ER} = $\sum_{x=1}^{6}\sigma_{xn}$) for ^{217}At* formed in ^{9}Li+^{208}Pb at various $E_{c.m.}$ for a fixed ΔR=1.556 fm, referring to Cal.1 in Tables 5.1 and 5.2, compared with experimental data [5] and other earlier calculations [5, 10].

illustrated in Fig. 5.2 and 5.3, respectively, give ℓ_{max} and ℓ_{min} values for σ_{xn} →0. We notice in Fig. 5.2 that all n-clusters are favorably preformed for ℓ values from 0 to 130 $\hbar$, and then drop suddenly to zero, setting the limiting value of P_0 <10^{-15} for ℓ_{max}=145 $\hbar$. Similarly, P in Fig. 5.3 fixes ℓ_{min}=44 $\hbar$ for P <10^{-15} not contributing to decay channel cross section. The decay channel cross section [or the production cross-section for each fragmentation (A_1, A_2)] $\sigma_{(A_1,A_2)}$ is then calculated for A_2=1-6, whose sum gives σ_{fus}, presented as Cal.1 in Tables 5.1 and 5.2, compared with $\sigma_{fus}^{Expt.}$ for the chosen six $E_{c.m.}$'s. Apparently, the DCM calculated $\sigma_{fus}^{Cal.1}$ fits the measured $\sigma_{fus}^{Expt.}$ data very nicely, as is further depicted in Fig. 5.4, where other available coupled channels calculations (CCFULL code) [5] and of Takigawa *et al.* [10] for Wong formula are also shown for comparisons. Note that the DCM calculations are a considerable improvement over the other available theoretical calculations, and also the extrapolation to a lower $E_{c.m.}$=14.4 MeV works good by presenting a systematic behavior (further discussed below in Table 5.5).

Extending the above work of ^{9}Li projectile on ^{208}Pb target, or that of Gupta and collaborators [2] on weakly bound projectiles, we fix the value of ΔR=1.556 fm

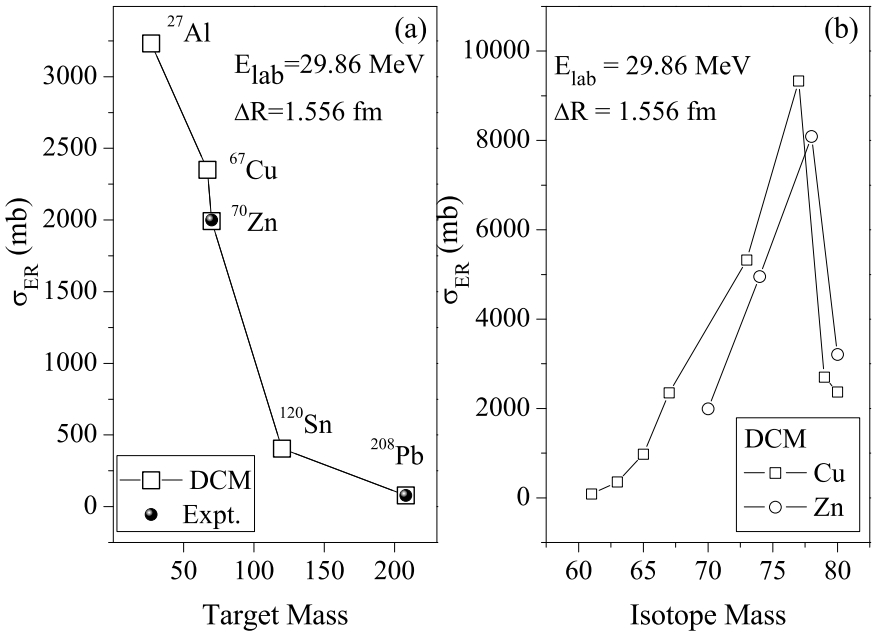

Figure 5.5: The dependence of DCM calculated σ_{ER} ($\equiv \sigma_{fus}$) at E_{Lab}=29.86 MeV and ΔR=1.556 fm, for loosely bound ^{9}Li projectile on (a) different targets, compared with experimental data, and (b) different isotopes of Cu and Zn targets (see Tables 5.3 and 5.4).

Table 5.3: The DCM calculated σ_{fus} ($\equiv \sigma_{ER}$) for ^{9}Li induced reactions at incident energy E_{Lab}=29.86 MeV and for ΔR=1.556 fm, compared with experimental data. † represents extrapolated value.

Reaction	$E_{c.m.}$ (MeV)	E^*_{CN} (MeV)	T (MeV)	σ_{fus} (mb) DCM	Expt.
^{9}Li+^{27}Al→^{36}S*	22.395	60.816	4.25	3232	-
^{9}Li+^{67}Cu→^{76}Ge*	26.324	34.935	2.21	2349.82	-
^{9}Li+^{70}Zn→^{79}As*	26.458	55.483	2.714	1992	2000 [4]†
^{9}Li+^{120}Sn→^{129}I*	27.776	50.128	2.01	404.25	-
^{9}Li+^{208}Pb→^{217}At*	28.5	27.309	1.145	77.55	77.7±8.6 [5]

Table 5.4: Same as for Table 5.3, but for different isotopes of Cu and Zn targets.

Reaction	$E_{c.m.}$ (MeV)	E^*_{CN} (MeV)	T (MeV)	σ^{fus}_{DCM} (mb)
^{9}Li+^{61}Cu→^{70}Ge*	26.021	59.553	2.989	87.27
^{9}Li+^{63}Cu→^{72}Ge*	26.1275	58.0885	2.91	352.367
^{9}Li+^{65}Cu→^{74}Ge*	23.593	54.706	2.787	974.3
^{9}Li+^{67}Cu→^{76}Ge*	26.324	34.935	2.21	2349.82
^{9}Li+^{73}Cu→^{82}Ge*	26.582	57.964	2.72	5326
^{9}Li+^{77}Cu→^{86}Ge*	26.735	53.189	2.5457	9333
^{9}Li+^{79}Cu→^{88}Ge*	26.806	50.06	2.44	2701
^{9}Li+^{80}Cu→^{89}Ge*	26.84	49.194	2.408	2367
^{9}Li+^{70}Zn→^{79}As*	26.458	55.483	2.714	1992
^{9}Li+^{74}Zn→^{83}As*	26.62	55.485	2.646	4955
^{9}Li+^{78}Zn→^{87}As*	26.77	38.441	2.16	8090
^{9}Li+^{80}Zn→^{89}As*	26.84	47.046	2.356	3212

Table 5.5: Same as for Table 5.3, but for E_{Lab}=15 MeV and ΔR=1.1777 fm.

Reaction	$E_{c.m.}$ (MeV)	E^*_{CN} (MeV)	T (MeV)	σ_{fus} (mb) DCM	Expt.
^{9}Li+^{70}Zn→^{79}As*	13.3	42.31	2.38	341	341±36.3
^{9}Li+^{208}Pb→^{217}At*	14.4	13.19	0.8	4.54×10^{-5}	-

empirically for ^{9}Li+^{208}Pb reaction forming ^{217}At* at, say, E_{Lab}=29.86 MeV (equivalent of $E_{c.m.}$=28.5 MeV for ^{9}Li+^{208}Pb, refer to Tables 5.1 and 5.2, Cal.1) and choose other stable isotope of targets like ^{27}Al, ^{67}Cu, ^{70}ZN and ^{120}Sn, that were used in earlier studies of the use of ^{9}Li projectile at intermediate energies [7], and calculate σ_{fus} ($\equiv \sigma_{ER} = \sum_{x=1}^{6} \sigma_{xn}$) for all of these ^{9}Li induced reactions at the above noted fixed neck-length parameter ΔR and fixed incident laboratory energy E_{Lab}. Results of this calculation are presented in Table 5.3, and the variation of σ_{fus} with target mass shown in Fig. 5.5(a), compared with experimental data. If the data at the chosen incident energy were not available, we have extrapolated or interpolated it. Interestingly, in agreement with earlier study on weakly bound projectiles [2], the (total) fusion cross section decreases as the mass of target nucleus increases. Apparently, this procedure could be used to predict the fusion cross-section of reactions for which the experimental data are not available. Note, however, that the calculated σ_{fus} depends strongly on the target mass and its (magic) shell structure. This is depicted in Fig. 5.5(b) and Table 5.4 for Cu and Zn isotopes. We notice that σ_{fus} increases as the isotopic mass increases, but drops down suddenly at the neutron magic number N=50. This means to suggest that the decreasing trend of σ_{fus} with target mass is true only for target nuclei near the β-stability line.

We have also checked the above results of ^{9}Li induced reactions on different target nuclei, for another fixed value of ΔR=1.1777 fm and fixed beam energy E_{Lab}=15 MeV, which is the highest measured energy for ^{9}Li+^{70}Zn reaction [4] and the lowest extrapolated value for ^{9}Li+^{208}Pb reaction [5]. The calculated results are shown in Table 5.5 (and Fig. 5.4), compared with experimental data, supporting the above results in Table 5.3 and Fig. 5.5(a). Note that the extrapolated data support the DCM calculations and fit in with the systematics.

Another quantity of interest in reactions induced by neutron-rich projectile is the near constancy of "barrier lowering" parameter ΔV_B at ℓ_{min} (or ℓ_{max}) values, listed in Table 5.6 for 1n and 2n decays of the CN formed in five chosen reactions

Table 5.6: The barrier modification factor $\Delta V_B(\ell)$ $[=V(R_a,\ell)-V_B(\ell)]$ at different ℓ_{min} values for the interaction potentials calculated for 1n and 2n decay channels of ^{9}Li induced reactions at E_{Lab}=29.86 MeV and ΔR=1.556 fm.

Reaction	ℓ_{min} ($\hbar$)	ΔV_B (MeV)	
		x=1	x=2
^{9}Li+^{27}Al$\rightarrow^{36}$S$^{*}\rightarrow$xn+$^{36-x}$S	12	-5.23	-5.863
^{9}Li+^{67}Cu$\rightarrow^{76}$Ge$^{*}\rightarrow$xn+$^{76-x}$Ge	14	-5.208	-5.756
^{9}Li+^{70}Zn$\rightarrow^{79}$As$^{*}\rightarrow$xn+$^{79-x}$As	15	-5.603	-5.8
^{9}Li+^{120}Sn$\rightarrow^{129}$I$^{*}\rightarrow$xn+$^{129-x}$I	21	-5.568	-5.908
^{9}Li+^{208}Pb$\rightarrow^{217}$At$^{*}\rightarrow$xn+$^{217-x}$At	33	-5.107	-5.535

of ^{9}Li with different targets at fixed ΔR=1.556 fm and fixed $E_{Lab.}$=29.86 MeV. We observe in Table 5.6 that the barrier modification or lowering in barrier height is almost of the same amount for 1n and 2n decays of all the ^{9}Li induced reactions. Note that, by definition, the effective "barrier lowering" parameter ΔV_B, is defined by the choice of ΔR, which is kept fixed here. Therefore, for the reactions having same value of ΔR (like in Tables 5.1-5.5), ΔV_B is of the similar order at the ℓ_{min} values. This means to say that almost same amount of modification in the barrier takes place in reactions induced by the same projectile having the same incident energy.

Fig. 5.6 shows the variation of ΔV_B with $E_{c.m.}$ at some arbitrary ℓ=50 $\hbar$ for 1n to 6n decay of ^{217}At* formed in ^{9}Li+^{208}Pb at fixed ΔR value for each $E_{c.m.}$ (Cal.1 in Tables 5.1 and 5.2). We notice that magnitude of ΔV_B decreases as $E_{c.m.}$ increases, being large $\sim$8-10 MeV for below barrier energies and is nearly constant $\sim$4 MeV at higher energies which is rather large (compared to expected zero value). It is relevant to remind here that the only acceptable explanation to hindrance phenomenon in coupled-channels calculation at sub-barrier energies is the requirement of "barrier lowering", which is an in-built property of the DCM through ΔR.

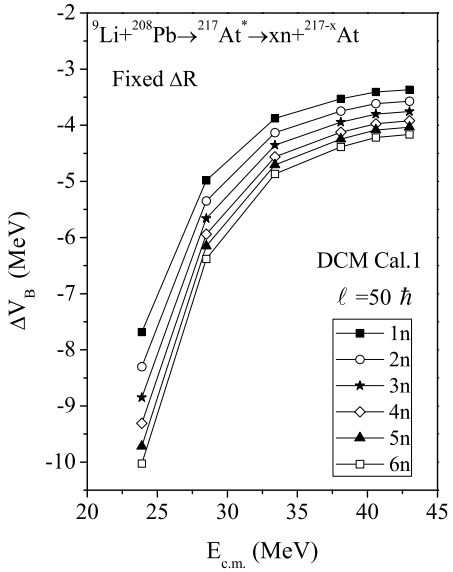

Figure 5.6: Variation of barrier modification parameter $\Delta V_B(\ell)$ with $E_{c.m.}$ at an arbitrary ℓ=50 $\hbar$ at fixed ΔR value at each $E_{c.m.}$ (Cal.1 in Tables 5.1 and 5.2) for ^{9}Li+^{208}Pb→^{217}At*→xn+$^{217-X}$At reaction with x=1-6.

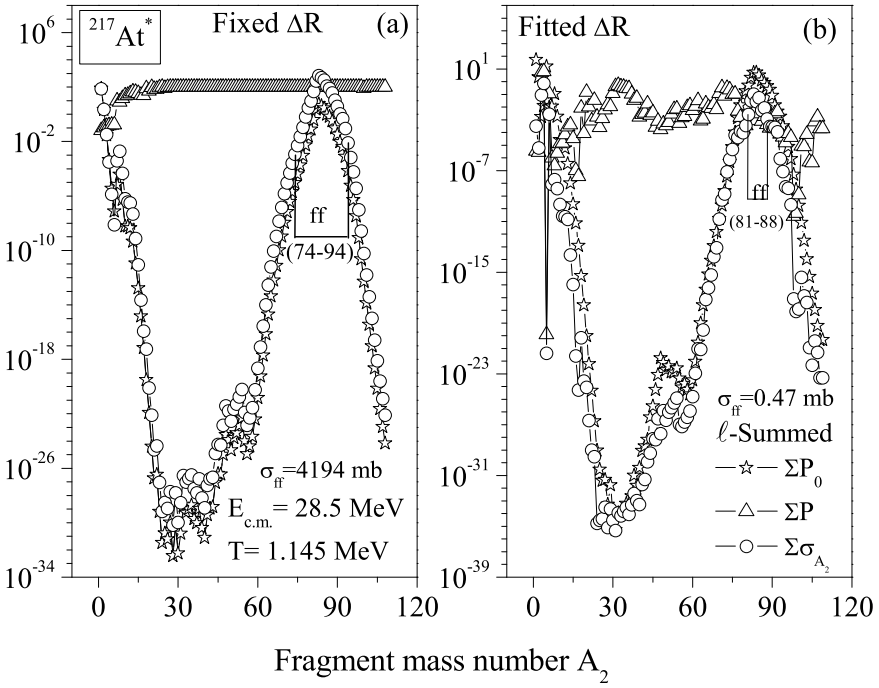

Figure 5.7: The ℓ-summed fragment preformation probability P_0, the penetrability P and the decay channel cross section σ_{A_2} as a function of the light fragment mass number A_2 for compound system ^{217}At* formed in ^{9}Li+^{208}Pb reaction at $E_{c.m.}$=28.5 MeV, for (a) fixed ΔR, and (b) fitted ΔR values.

5.2.2 Decay of ^{217}At* formed in ^{9}Li+^{208}Pb reaction using ΔR fitted for each decay channel individually

The so far presented calculation in sub-section 5.2.1 is for a fixed value of ΔR for all decay channels, i.e., same reaction time for all decay channels (xn, x=1-6 and ff channel) (refer to Cal.1 in Tables 5.1 and 5.2 and Fig. 5.1) and the details illustrated are for $E_{c.m.}$=28.5 MeV ($E_{Lab.}$=29.86 MeV) at fixed ΔR=1.556 fm, where calculated (total) fusion cross section $\sigma_{fus}^{Cal.1}$ as a pure CN decay process is compared with $\sigma_{fus}^{Expt.}$. The comparisons are very nice (refer to Fig. 5.4 and Tables 5.3 and 5.5), but *only when no care is taken for the fits obtained for individual channels.* A quick comparison of the calculated $\sigma_{xn}^{Cal.1}$ for individual decay channels (xn, x=1-6) with measured ones show that most of the contribution to $\sigma_{fus}^{Cal.1}$ comes from the un-observed 1n channel, and the calculated $\sigma_{xn}^{Cal.1}$'s for the observed decay channels (3n and 4n in case of $E_{c.m.}$=28.5 MeV) is very small compared to experimental numbers. In this context, we know from our earlier study [18] that $1n$ contribution could be reduced to almost zero if the data for other, not yet observed or used, channels were also included in the fitting procedure. Furthermore, in Fig. 5.7(a) is plotted the ℓ-summed P_0, P and channel cross section σ_{A_2} as a function of A_2 for CN ^{217}At* at $E_{c.m.}$=28.5 MeV and fixed ΔR=1.556 fm, giving fusion-fission cross section σ_{ff}=4194 mb for the ff mass region A_2=74-94 marked in Fig. 5.1 (plus the complementary heavy fragments), which is much larger than σ_{ER} ($=\sum_{x=1}^{6}\sigma_{xn}$=77.55 mb) and very large as compared to the experimentally expected negligibly small cross section for this decay channel, i.e., compared to assumed $\sigma_{ff}^{Expt.}$=0. Apparently, these results call for a different reaction time for each decay channel xn, x=1-6, and ff, i.e., instead of fixed, the fitted ΔR for each decay channel, which is done here in the following.

Fig. 5.8 shows the fragmentation potential for decay of ^{217}At* formed in the

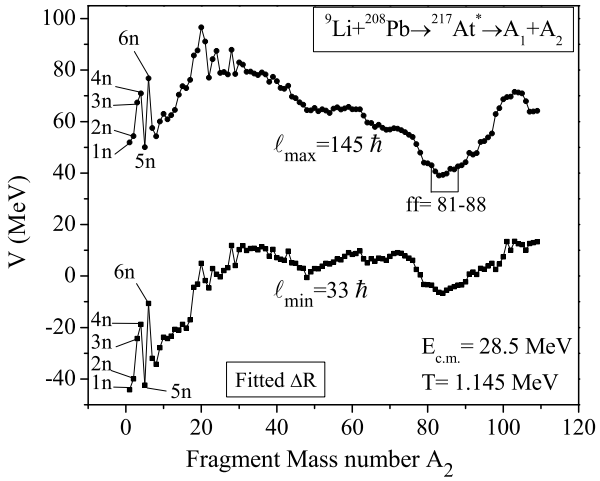

Figure 5.8: Mass fragmentation potential $V(A_2)$, minimized in charge fragmentation coordinate η_Z, for the decay of ^{217}At* formed in ^{9}Li+^{208}Pb reaction at $E_{c.m.}$=28.5 MeV and at ℓ_{min} and ℓ_{max} values. Some of the most favored fragments are replaced by fragments of interest from experiments point of view (see text). The best fitted ΔR values for A_2=1-6 are 0.9, 0.9, 2.02, 2.0, -0.3 and 1.5, respectively, and 0.4 for A_2=7-109.

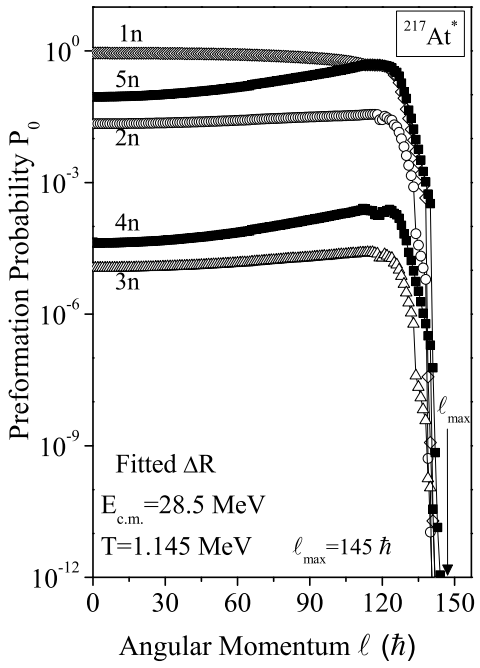

Figure 5.9: Preformation probability P_0 as a function of angular momentum ℓ for xn, x=1-6, decays of ^{217}At* formed in ^{9}Li+^{208}Pb reaction at $E_{c.m.}$=28.5 MeV, using mass fragmentation potential $V(A_2)$ in Fig. 5.8.

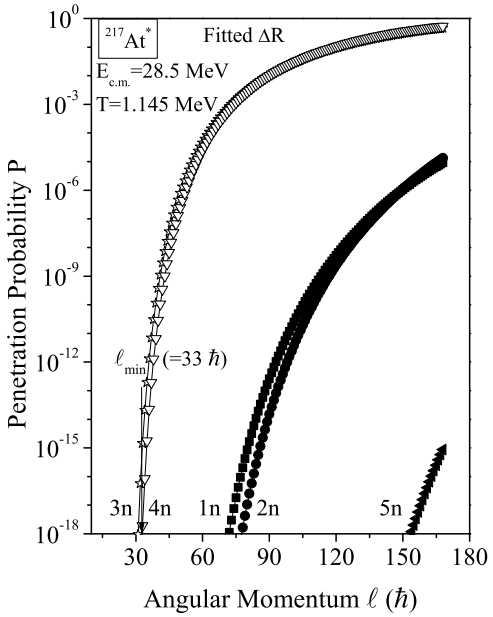

Figure 5.10: Same as for Fig. 5.9, but for penetration factor P.

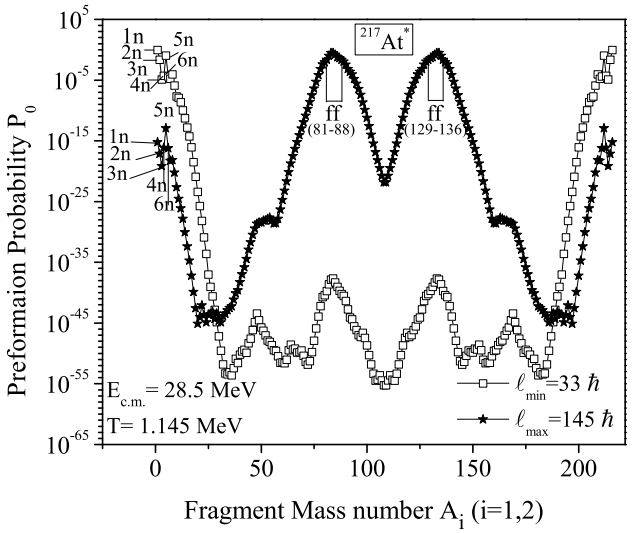

Figure 5.11: Preformation probability P_0 as a function of fragment mass number A_i (i=1, 2) for mass fragmentation potential $V(A_2)$ of ^{217}At* in Fig. 5.8.

^{9}Li+^{208}Pb reaction at $E_{c.m.}$=28.5 MeV (T=1.145 MeV) and at ℓ_{min} and ℓ_{max} values determined, just as in Figs. 5.2 and 5.3, for $P_0(\ell)$ and $P(\ell)$ becoming negligibly small for their contributions to cross-section (see Fig. 5.9 and Fig. 5.10). Since the measured cross sections are of different $^{211-214}$At isotopes only [5], i.e., x-neutrons, x=3-6, emission, here in Fig. 5.8 again we have replaced the binding energy of energetically most favored fragment with the binding energy of respective 1n to 6n neutron cluster. The best fitted values of ΔR obtained for xn and ff region are given in the figure caption of Fig. 5.8. We notice in Fig. 5.8 that there is a strong minimum at 5n cluster, and, hence for cross sections of similar orders, the ff region for σ_{ff} $\rightarrow$0 also changes from A_2=74-94 to 81-88. A similar result is presented in Fig. 5.11 for the calculated preformation probability $P_0(A_2)$, which gives the fragment-formation dynamical yield for use of the fragmentation potential in Fig. 5.8. It is clear from Fig. 5.11 that at lower ℓ values, i.e., at ℓ_{min} the LPs are favored (higher P_0 or energetically lower in fragmentation potential) and at higher ℓ values, i.e., at ℓ_{max} the near-symmetric and symmetric fission fragments are more preferred. At ℓ_{min} value, the yields P_0 for 1n and 5n are even larger than the ff yields at ℓ_{max} value. The same result for best fitted ΔR is better illustrated in Fig. 5.7(b) for the ℓ-summed P_0, P and σ_{A_2}, showing, in agreement with experiments, very small σ_{5n} though P_0 is large for 5n, but the ℓ-summed P is very small $\sim 10^{-20}$. The interesting result is that now σ_{ff} $\sim$0.47 mb, i.e., negligibly small compared to σ_{ER}=77.743 mb (refer to Tables 5.1 and 5.2, Cal.2), which fits with the experimental expectations.

Fig. 5.12 gives the ℓ-dependent scattering potential $V(R)$ for ^{213}At+4n in the decay of ^{217}At* formed in ^{9}Li+^{208}Pb reaction at $E_{c.m.}$=28.5 MeV. The first and second turning points R_a and R_b are labelled, and the barrier lowering parameter $\Delta V_B = V(R_a) - V_B$ shown for both the ℓ_{max} and ℓ_{min} values. Note, ΔV_B for each ℓ is defined as a negative quantity since the actually used barrier is effectively lowered. Thus, the fitting parameter ΔR controls the "barrier lowering" ΔV_B.

The DCM result of calculation for the best possible fit to observed decay channels

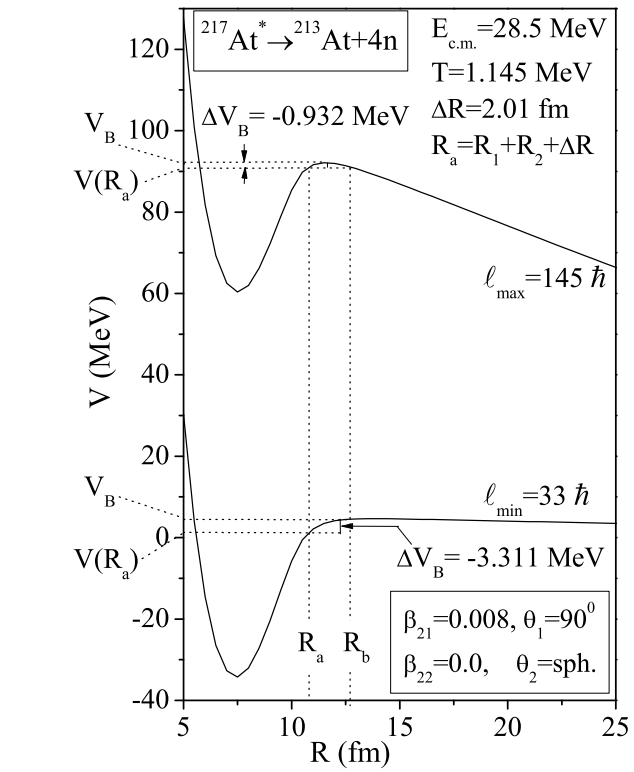

Figure 5.12: The ℓ-dependent scattering potential $V(R)$ for ^{213}At+4n in the decay of ^{217}At* formed in ^{9}Li+^{208}Pb reaction at $E_{c.m.}$=28.5 MeV and optimum orientations θ_1^{opt}=90^0 and θ_2^{opt}=spherical for β_{21}=0.008 and β_{21}=0.0. The first and second turning points R_a and R_b are labelled, and the barrier lowering parameter $\Delta V_B = V(R_a) - V_B$ shown for both the ℓ_{max}=145 $\hbar$ and ℓ_{min}=33 $\hbar$ values.

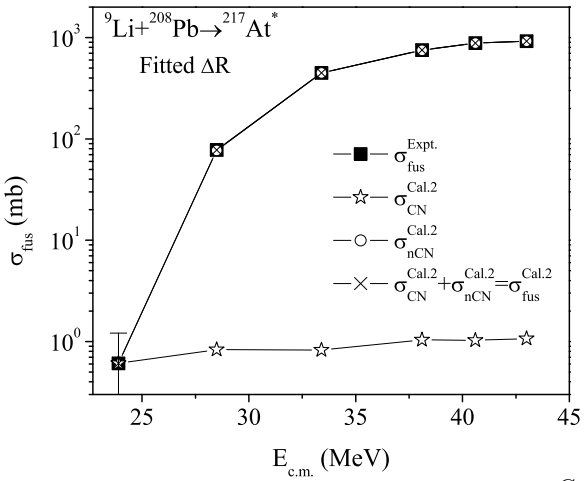

Figure 5.13: The DCM calculated fusion cross section $\sigma_{fus}^{Cal.2}$, the sum of (pure) CN contribution $\sigma_{CN}^{Cal.2}$ and the nCN contribution $\sigma_{nCN}^{Cal.2}$ fitted to empirically estimated σ_{nCN}^{emp} as a quasi-fission-like process, compared with $\sigma_{fus}^{Expt.}$ for ^{217}At* formed in ^{9}Li+^{208}Pb reaction at various center-of-mass energies $E_{c.m.}$'s. The error bars are shown only if larger than the size of symbol used for data.

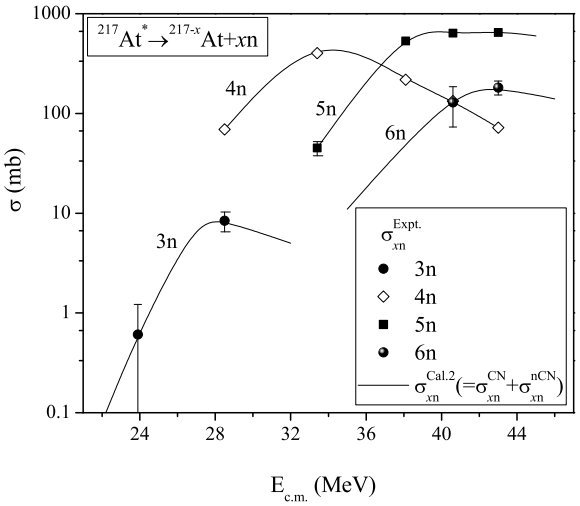

Figure 5.14: The DCM calculated excitation functions of individual evaporation channels in ^{217}At$^{*}\rightarrow^{217-x}$At+xn where x=3, 4, 5 and 6, compared with the experimental data. The error bars are shown only if larger than the size of symbol used for data, and lines or curves are for the guide of eyes.

is presented in Tables 5.1 and 5.2, Cal.2 for (pure) CN contribution, $\sigma_{CN}^{Cal.2}$, which gives a very poor (under-estimated) comparison with the observed channel data, though the contribution of un-observed xn-decays and ff channels is reduced considerably. The only case of exact fitting is that of $E_{c.m.}$=23.9 MeV where only the $4n$ decay channel is observed. Also, as already observed from Fig. 5.7(b), the ff channel cross section is now very small, σ_{ff}=0.47 mb. The strong disagreement between $\sigma_{CN}^{Cal.2}$ and $\sigma_{fus}^{Expt.}$ calls for the empirical nCN contributions, σ_{nCN} $(= \sigma_{fus}^{Expt.} - \sigma_{CN}^{Cal.2})$. The empirically obtained σ_{nCN}^{emp} were then fitted as the qf-like process, i.e., the DCM with P_0=1. In Tables 5.1 and 5.2, we find that $\sigma_{nCN}^{Cal.2}$ added to $\sigma_{CN}^{Cal.2}$, giving $\sigma_{fus}^{Cal.2}$, compare almost exactly with σ_{fus}^{Expt}, with $\sigma_{nCN}^{Cal.2}$ constituting most of the fusion cross section for all the incident energies. This is further illustrated in Fig. 5.13, where we find that, instead of CN, the nCN component contributes most towards the total fusion cross section. The nature of fits obtained between the DCM Cal.2 and experimental data for the excitation functions of observed individual evaporation channels, i.e., 3n, 4n, 5n and 6n decay channels, are also shown in Fig. 5.14. Both individual xn decay channel cross sections σ_{xn} in Fig. 5.14 and their sum σ_{fus} in

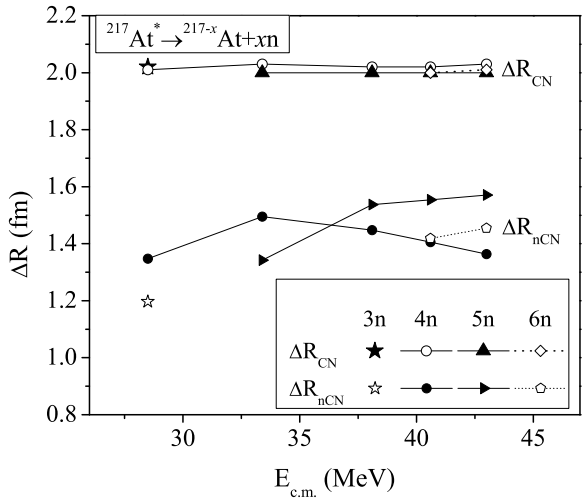

Figure 5.15: The best fitted neck-length parameters ΔR's for CN and nCN processes in cases of observed $3n$ to $6n$ evaporation channels in ^{217}At$^{*}\rightarrow^{217-x}$At+xn, where x=3, 4, 5 and 6, plotted as a function of $E_{c.m.}$.

Fig. 5.13 compare nicely with data. The error bars in both the Figs. 5.13 and 5.14 are shown only for the cases where they are larger than the size of symbols. Solid lines in Fig. 5.14 represent the DCM calculations for the best fitted ΔR's, giving σ_{xn} ($=\sigma_{CN}^{Cal.2}+\sigma_{nCN}^{Cal.2}$) and the lines or curves are shown as the guide for eyes.

Furthermore, it is of interest to compare the best fitted neck-length parameters ΔR's for CN and nCN processes, and study their variations with $E_{c.m.}$. This is depicted in Fig. 5.15. Interestingly, $\Delta R_{CN} > \Delta R_{nCN}$ which means that CN neutrons emission occurs earlier than the nCN qf-like decay, supported by our earlier studies [19]. Also, both ΔR_{CN} and ΔR_{nCN} are nearly independent of $E_{c.m.}$, where ΔR_{CN} $\sim$2.02$\pm$0.01 fm and ΔR_{nCN} $\sim$1.45$\pm$0.10 fm. This result is useful for further experimental and theoretical studies.

Finally, we analyze our DCM calculations in Tables 5.1 and 5.2 in terms of the CN formation probability P_{CN} [16] and its survival probability P_{surv} [17]. For Cal.1 (fixed ΔR), the CN fusion cross sections σ_{fus} ($=\sigma_{ER} = \sum_{x=1}^{6}\sigma_{xn}$) at each $E_{c.m.}$ fit the experimental data nearly exactly, and hence σ_{nCN}=0. On the other hand, compared to σ_{ER}, σ_{ff} is very large (e.g., see in Fig. 5.7(a) and Table 5.1 and Table 5.2 for $E_{c.m.}$=28.5 MeV, σ_{ff}=4194 mb and σ_{ER}=77.55 mb). This means that, for

Table 5.7: The DCM calculated ER, the nCN contribution, and ff cross sections for the best fitted ΔR case (Cal.2) in decay of ^{217}At* formed in ^{9}Li+^{208}Pb reaction at various center of mass energies. The CN formation probability P_{CN} is calculated for the measured data (=σ_{ER}), where as the CN survival probability P_{surv} ≈1 since σ_{ff} is relatively very small, except for $E_{c.m.}$=23.9 MeV (see text).

$E_{c.m.}$ (MeV)	σ_{ER} (mb)	σ_{nCN} (mb)	σ_{ff} (mb)	P_{CN}
23.9	0.61	0	0.33	1.0
28.5	77.743	76.91	0.47	0.0107
33.4	448.024	447.2	1.42	0.0017
38.1	752.04	751	1.75	0.0014
40.6	882.03	881	2.79	0.0012
43.0	922.97	921.9	2.84	0.0011

Cal.1, P_{CN}=1 and P_{surv}=0 at all $E_{c.m.}$'s. Similarly, for Cal.2 (fitted ΔR), we present our results (from Tables 5.1 and 5.2 and Fig. 5.7(b)) for σ_{ER}, the nCN contribution σ_{nCN} and σ_{ff} in Table 5.7. We notice that in this case σ_{ff} is negligibly small, compared to σ_{ER}, and that σ_{nCN} is the main content in σ_{ER}. This leads to P_{surv} ≈1 and P_{CN} <<1, except for $E_{c.m.}$=23.9 MeV, where, like for Cal.1, σ_{nCN}=0 and hence P_{CN}=1. Apparently, Cal.2 presents the realistic experimental situation, with ^{9}Li induced reaction cross section being a more quasi-fission-like non-compound nucleus decay process.

5.2.3 Synthesis of ^{217}At*: the "cold" (t,p) combinations for fixed neck-length ΔR

In this subsection, we look for "cold" target-projectile (t,p) combinations (referring to potential energy minima) for the formation of CN ^{217}At*. Figure 5.16 shows the mass fragmentation potential $V(A_i)$ for the formation of CN ^{217}At* at ℓ_{max}=145 $\hbar$ for the optimum "hot" fusion configurations at $E_{c.m.}$=28.5 MeV (equivalently, T= 1.145

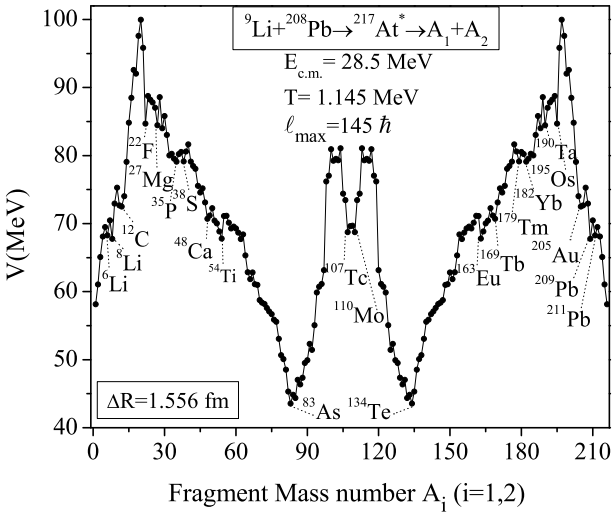

Figure 5.16: Mass fragmentation potential $V(A_i)$, minimized in charge fragmentation coordinate η_Z, at ℓ_{max}=145 $\hbar$, for the formation of CN ^{217}At* corresponding to $E_{c.m.}$=28.5 MeV and T=1.145 MeV showing the possible (t,p) combinations referring to minima.

MeV) for a constant ΔR value. The minima in $V(A_i)$ refer to possible (t,p) combinations, which are known to be nearly independent of ΔR value [14]. The "hot" fusion configurations are used here because we know from the earlier Sub-sections that the observed decay of ^{217}At* emit more than one or two neutrons. The resulting projectile + target combinations include ^{6,8}Li+^{211,209}Pb, ^{12}C+^{205}Au, ^{22}F+^{195}Os, ^{27}Mg+^{190}Ta, ^{35}P+^{182}Yb, ^{38}S+^{179}Tm, ^{48}Ca+^{169}Tb, ^{54}Ti+^{163}Eu, ^{83}As+^{134}Te and ^{107}Tc+^{110}Mo. Interestingly, we propose here ^{8}Li+^{209}Pb as one of the reaction, whereas we find that ^{8}He+^{209}Bi reaction is proposed to be studied at ISOLDE facility [20]. Since we know from our calculations of Fig. 5.16 that ^{8}Li lies lower in energy than ^{8}He, the fusion cross section for ^{8}Li+^{209}Pb reaction is expected to be higher than for ^{8}He+^{209}Bi. Note that ^{8}Li+^{209}Pb and other proposed (t,p) combinations are based on a theory (QMFT), whereas the reactions like ^{8}He+^{209}Bi are proposed simply on the basis of availability.

As a next step, in order to optimise our choice of a (t,p) combination for the production of largest cross section, we have plotted in Fig. 5.17 the interaction potentials $V(R)$ for all (t,p) combinations referring to minima in Fig. 5.16, i.e.,

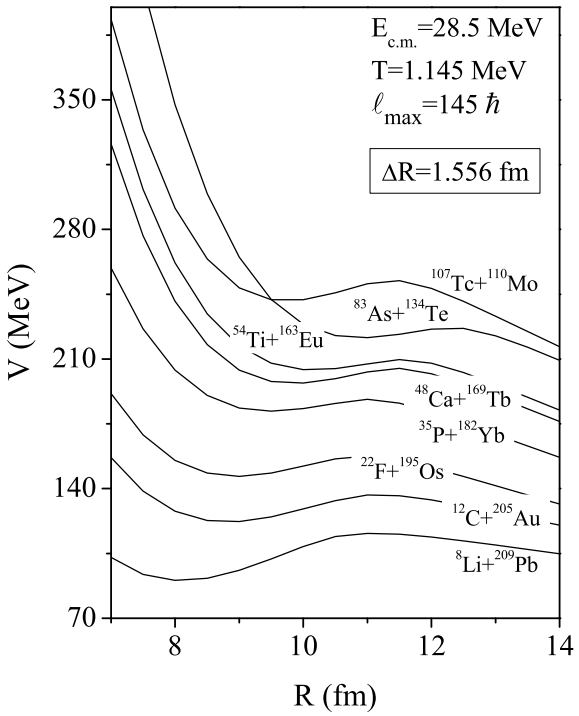

Figure 5.17: Scattering potential V(R) for "cold fusion" reactions mentioned in Fig. 16 with "hot compact" configurations at $E_{c.m.}$=28.5MeV (T=1.145 MeV) and ℓ_{max}=145 $\hbar$.

to "cold fusion" reactions with "hot compact" configurations. This implies that the optimum (t,p) combination is one with lowest interaction barrier and smallest (most compact) interaction radius. We notice from Fig. 5.17 that the lowest barrier and smallest radius occur for the most asymmetric ^{8}Li+^{209}Pb combination and highest barrier and largest interaction radius occur for near symmetric ^{110}Mo+^{107}Tc combination. However, it may be noted from our earlier study [14] that ^{48}Ca based reaction ^{48}Ca+^{169}Tb should produce the largest fusion cross section due to its double magic character.

5.3 Summary

In this paper, we have studied the decay mechanism of CN ^{217}At* formed in a reaction induced by neutron-rich ^{9}Li on doubly magic shell nucleus ^{208}Pb at various center-of-mass energies $E_{c.m.}$, using the dynamical cluster-decay model (DCM). We

aim at investigating the role of neutron-rich light projectile on (total) fusion cross section σ_{fus}, knowing well that σ_{fus} is largest for a reaction with doubly magic reaction partner. In ^{9}Li+^{208}Pb reaction, for the LPs evaporation residues, only 3n-6n emissions are observed (i.e., 1n and 2n are not observed) whose sum of the cross sections $\sum_{x=1}^{6} \sigma_{xn} \equiv \sigma_{fus}$ (including the unobserved 1n and 2n cross sections), can be fitted very nicely within the DCM as a pure CN decay process for a fixed value of the only parameter of this model, the neck-length parameter ΔR. Similar calculations of ^{9}Li induced reactions on ^{70}Zn and various isotopes of other targets used in earlier experimental studies at intermediate energies, show a strong dependence of σ_{fus} on mass and shell structure of the target nucleus, supporting the above stated effect of closed magic shells. However, in this case of fixed ΔR, the unobserved decay channels (1n, 2n) are strongly over-estimated, and hence the observed ones (3n-6n) strongly under-estimated, with the ff cross section σ_{ff} also being very large compared to nearly zero, expected in experiments.

To improve upon the above result, we have fitted the individual decay channels (both unobserved and observed ones), together with the ff channel, with different ΔR values, i.e., different reaction times for different decay channels. Interestingly, now the fits for the pure CN decay cross section are very poor for LPs residue channels ($\sigma_{CN} < 1\%$ of total $\sigma_{fus}^{Expt.}$) with σ_{ff} reduced nearly to zero. This calls for the empirical nCN contribution, which is treated as the quasi-fission-like process (channel preformation probability P_0=1). Excellent fits are once again obtained for $\Delta R_{nCN} < \Delta R_{CN}$, with σ_{nCN} constituting most (99%) of the σ_{fus} at all the incident energies. In terms of CN formation and CN survival probabilities, the above result means $P_{CN} << 1$ and $P_{surv} \approx 1$. Thus, our DCM analysis shows that ^{9}Li induced reaction is more of a quasi-fission-like non-compound nucleus decay.

Furthermore, the synthesis of ^{217}At* via various "cold" (t,p) combinations, refereeing to potential energy minima, for "hot" compact configurations, is carried out and ^{8}Li+^{209}Pb as the optimum combination with lowest interaction barrier and

smallest (most compact) interaction radius identified. In view of the role of double magic shell, however, ^{48}Ca+^{169}Tb would result in largest fusion cross section.

Bibliography

[1] R. K. Gupta, Lecture Notes in Physics 818 *Clusters in Nuclei*, ed C. Beck, Vol.I, (Springer Verlag), p. 223 (2010); and earlier references there in it.

[2] M. Kaur, B. Singh, M. K. Sharma, and R. K. Gupta, Phys. Rev. C **92**, 024623 (2015).

[3] A. V. Dobrovolsky *et al.*, Nucl. Phys. **A766**,1 (2004).

[4] W. Loveland *et al.*, Phys. Rev. C **74**, 064609 (2006).

[5] A. M. Vinodkumar *et al.*, Phys. Rev. C **80**, 054609 (2009).

[6] D. Peterson, J. J. Kolata, P. Santi, J. von Schwarzenberg, D. Bazin, and B. M. Sherrill, Phys. Rev. C **67**, 014601 (2003).

[7] B. Blank *et al.*, Nucl. Phys. **A555**, 408 (1993).

[8] M. Petrascu et al., Phys. Lett. **B405**, 224 (1997).

[9] A. Yoshida *et al.*, in *Heavy Ion Fusion: Exploring the Variety of Nuclear Properties*, ed A. M. Stefanini, G. Nebbia, S. Lunardi, and G. Montagnoli (World Scientific, Singapore, 1994), pp. 311.

[10] N. Takigawa, M. Kuratani, and H. Sagawa, Phys. Rev. C **47**, R2470 (1993).

[11] W. Reisdorf, Z. Phys. A **300**, 227 (1981).

[12] C. Y. Wong, Phys. Rev. Lett. **31**, 766 (1973).

[13] M. Dasgupta *et al.*, Phys. Rev. C **70**, 024606 (2004).

[14] Niyti and R. K. Gupta, Phys. Rev. C **89**, 014603 (2014).

[15] A. Kaur, B. R. Behera, and R. K. Gupta, Proceedings the DAE-BRNS Symp. on Nucl. Phys. **60**, 480 (2015); available at http://www.sympnp.org/proceedings/60/B77.pdf

[16] A. Kaur, S. Chopra, and R. K. Gupta, Phys. Rev. C **90**, 024619 (2014).

[17] S. Chopra, A. Kaur, and R. K. Gupta, Phys. Rev. C **91**, 034613 (2015).

[18] S. Chopra, M. Bansal, M. K. Sharma, and R. K. Gupta, Phys. Rev. C **88**, 014615 (2013).

[19] Niyti, R. K. Gupta, and W. Greiner, J. Phys. G: Nucl. Part. Phys. **37**, 115103 (2010).

[20] S. M. Lukyanov *et al.*, CERN-INTC-2013-005/ INTC-P-371.

Chapter 6

Compound nucleus formation probability P_{CN} determined within the dynamical cluster-decay model for various "hot" fusion reactions

6.1 Introduction

In nuclear reactions, the concept of compound nucleus fusion/ formation probability P_{CN} [1] arises from the compound nucleus (CN) model of N. Bohr [2] wherein for the complete fusion in entrance channel he assumed P_{CN}=1, and treated the CN decay statistically. However, in the decay channel, non-compound nucleus (nCN) decays such as the quasi-fission (qf), deep-inelastic collisions/ orbiting (DIC), incomplete fusion (ICF) or pre-equilibrium decay also contribute to the overall (fusion) cross section, which means P_{CN} <1 for the CN content, and hence Bohr's CN-model needs an extention/ re-examination.

The P_{CN} is the least understood quantity, but quite important for the study of heavy ion reactions. For quite some time, attempts are being made to use P_{CN} in determining the evaporation residue cross section σ_{ER} (see, e.g., [3–5]), given as

the product of the capture cross section $\sigma_{capture}$, the CN formation probability P_{CN} and the survival probability P_{surv}, each term treated and calculated separately [3]. Note that, in the language of coupled channel calculations, $\sigma_{capture}$ includes the nCN cross section σ_{nCN}, and hence is equivalent of (total) fusion cross sections σ_{fusion}, if calculated as "barrier crossing" [5]. P_{surv} is the probability that the fused system will de-excite by emission of neutrons or light particles (equivalently, evaporation residue) rather than fission. This is another quantity, not fully understood [6, 7]. In our published work [1] and in a conference report [8], we defined P_{CN} for the first time on the basis of the dynamical cluster-decay model (DCM) of Gupta and collaborators [9–30], which we extend here in this paper to a larger number of reactions (about a dozen) having non-zero σ_{nCN} component, to more than one nuclear interaction potential, and to a larger number of variables on which the P_{CN} depends. It is relevant to remind here that in DCM, the CN fusion cross section σ_{CN} depends not only on "barrier penetrability" P, but also on fragment preformation factor P_0.

Heavy-ion fusion reactions have received great attention in recent years, and this is an important and exciting research area of nuclear physics. This study has facilitated to investigate the production and reaction mechanism of new heavy and superheavy nuclei via fusion reactions. Heavy-ion reactions at below barrier energies give rise to highly excited compound nuclear systems that carry large angular momentum, and hence decay by emitting neutrons or multiple light particles (LPs: A$\leq$4, Z$\leq$2, like n, p, α), and their heavier counterparts and γ-rays, termed the evaporation residue ER, and fusion-fission (ff) consisting of near-symmetric and symmetric fission fragments (nSF and SF), including also the intermediate mass fragments (IMFs) of masses 5$\leq$A$\leq$20 and 2$<$Z$<$10. In addition, many a times a non-compound nucleus (nCN) decay process also contributes to the (total) fusion cross section, and here in the following, we are interested in such reactions where the nCN cross section σ_{nCN} is non-zero.

Fig. 1.4 in Chapter 1 illustrates schematically the various components of com-

pound nucleus (CN) decay/ fusion cross section, also called the CN production cross section, or simply the (total) fusion cross section σ_{fusion}, given as

$$\begin{aligned} \sigma_{fusion} &= \sigma_{CN} + \sigma_{nCN} \\ &= \sigma_{ER} + \sigma_{ff} + \sigma_{nCN} \end{aligned} \tag{6.1}$$

In a fission-less decay, the contribution of σ_{IMFs}, that forms a part of σ_{ff}, is in general small, of the order of 5 to 10% of σ_{ER}, i.e., $\sigma_{IMFs} \approx (5-10\%)\sigma_{ER}$. Note that all these components of fusion cross section σ_{fusion} are individually measurable quantities. In case, the nCN component σ_{nCN} were not measured, it can be estimated empirically from the calculated and measured quantities, as

$$\sigma_{nCN} = \sigma_{fusion}^{Expt.} - \sigma_{fusion}^{Cal.}. \tag{6.2}$$

It may be pointed out that different mass regions of compound nuclei constitute different combinations of these processes (ER, IMFs, ff and nCN) or a single one of them as the dominant mode.

Knowing the cross sections for CN and nCN processes, i.e., σ_{CN} $(=\sigma_{ER}+\sigma_{ff})$ and σ_{nCN}, of the (total) fusion cross section σ_{fusion}, the CN formation probability P_{CN} is defined [8,24] as the ratio of CN formation cross section σ_{CN} and the (total) fusion cross section σ_{fusion} which includes the non-compound nucleus component σ_{nCN},

$$P_{CN} = \frac{\sigma_{CN}}{\sigma_{fusion}} = 1 - \frac{\sigma_{nCN}}{\sigma_{fusion}}. \tag{6.3}$$

Clearly, P_{CN} gives the content of CN formation in the total fusion cross section, or its deviation from unity by the nCN content. In other words, if σ_{nCN}=0, P_{CN}=1 and the reaction is a pure CN reaction. Thus, the determination of P_{CN} gives a possibility to understand the role of σ_{nCN} component in σ_{fusion}.

In the following, we consider an application of Eq. (6.3) to a set of some

reactions with different entrance channels leading to different compound nuclei. The calculations are made for various center-of-mass energies, and are based on the systematic analysis of measured data using the dynamical cluster-decay model (DCM) [15–24, 26–30]. The possible role of different nuclear proximity interactions, and deformed, oriented configurations is also analyzed in these works. The DCM calculations include deformation effects up to hexadecapole deformations (β_2, β_3, β_4), with compact orientations θ_{ci}, i=1, 2 [31], or up to only quadrupole deformation (β_{2i}) with optimum orientations $\theta_i^{opt.}$ [32], of "hot" fusion process, for both the cases of co-planar (azimuthal angle Φ=0^0) and non-coplanar nuclei ($\Phi \neq 0^0$).

6.2 Calculations and discussion of the result

In this section, we present the results of our calculations for the compound nucleus formation probability P_{CN}, based on calculations made by using the DCM. The chosen reactions, giving different compound nuclei, studied on the DCM for all possible decay processes at different center-of-mass energies $E_{c.m.}$, are:
^{12}C+^{93}Nb$\rightarrow^{105}$Ag* including both co-planar(azimuthal angle, Φ = 0) [23] and non co-planar ($\Phi\neq$0) [26] configurations, ^{32}S+^{92}Mo$\rightarrow^{124}$Ce* [24], ^{11}B+^{238}U$\rightarrow^{246}$Bk* and ^{14}N+^{232}Th$\rightarrow^{246}$Bk* [15], ^{19}F+^{198}Pt$\rightarrow^{217}$Fr* [27, 28], ^{19}F+^{1984}Pt$\rightarrow^{213}$Fr* [27, 28], ^{11}B+^{204}Pb$\rightarrow^{215}$Fr* [29], ^{18}O+^{197}Au$\rightarrow^{215}$Fr* [29], ^{9}Li+^{208}Pb$\rightarrow^{217}$At* [30], the ^{64}Ni-based reactions ^{64}Ni+^{100}Mo$\rightarrow^{164}$Yb* [16, 21], ^{112,118,124}Sn+^{64}Ni$\rightarrow^{176,182,188}$Pt* and ^{64}Ni+^{132}Sn$\rightarrow^{196}$Pt* [20, 22], and the ^{48}Ca-based reactions ^{48}Ca+^{154}Sm$\rightarrow^{202}$Pb* [17], ^{48}Ca+^{238}U$\rightarrow^{286}$Cn* [19], and ^{48}Ca+^{244}Pu$\rightarrow^{292}$Fl* [18]. It may be reminded that these are all "hot" fusion reactions, and the nCN-component is calculated as the quasi-fission (qf) process, i.e., $\sigma_{nCN} \equiv \sigma_{qf}$. Best fit to data were made for σ_{ER}, σ_{ff} (or σ_{IMFs}), and the measured or empirically obtained σ_{qf}. The possible role of use of different nuclear proximity potentials (pocket formula or Skyrme forces in SEDF) and different azimuthal angle Φ (=0^0 or $\neq 0^0$) are also investigated. Deformed, ori-

Table 6.1: Characteristic properties of chosen reactions investigated on the DCM, using pocket formula of Blocki *et al.* [45] and Skyrme energy density formalism (SEDF) [21, 22], for the c.m. energy range $E_{c.m.}$=41.1-201.3 MeV, arranged as per two groups in Fig. 6.5 and the two nuclear interactions used.

Reactions	Φ (deg.)	Z_{CN}	A_{CN}	$E_{c.m.}$ (MeV)	E^* (MeV)	Z_1Z_2	χ	P_{CN}	Ref.
Blocki *et al.* formula									
^{64}Ni+^{100}Mo→^{164}Yb*	0	70	164	122.9-158.8	30.6-66.5	1176	0.622	0.62-0.94	[16]
^{64}Ni+^{100}Mo→^{164}Yb*	≠0	70	164	122.9-158.8	30.6-66.5	1176	0.622	0.784-1	[21]
^{48}Ca+^{154}Sm→^{202}Pb*	0	82	202	135.5-156.8	44.5-65.3	1240	0.693	0.77-0.89	[17]
^{12}C+^{93}Nb→^{105}Ag*	0	47	105	41.09-54.21	40.95-54.06	246	0.438	0.13-0.25	[23]
^{12}C+^{93}Nb→^{105}Ag*	≠0	47	105	41.09-54.21	40.95-54.06	246	0.438	0.296-0.091	[26]
^{32}S+^{92}Mo→^{124}Ce*	0	58	124	111.3	46.5	672	0.565	0.88	[24]
^{48}Ca+^{238}U→^{286}Cn*	0	112	286	187.1-201.3	26.5-40.6	1840	0.91	0.005-0.2	[18]
^{244}Pu+^{48}Ca→^{292}Fl*	0	114	292	190.8-200.2	27.4-36.9	1880	0.93	0.113-0.14	[19]
^{14}N+^{232}U→^{246}Bk*	0	97	246	68.5-86.4	43-60.9	630	0.796	0.978-1	[15]
^{11}B+^{235}U→^{246}Bk*	0	97	246	49-70.6	34.3-55.9	460	0.796	1-0.78	[15]
^{64}Ni+^{112}Sn→^{176}Pt*	0	78	176	149.75-188.25	22.92-61.42	1400	0.72	1-0.927	[20]
^{64}Ni+^{118}Sn→^{182}Pt*	0	78	182	155.8-193.05	33.215-70.465	1400	0.696	1-0.91	[20]
^{64}Ni+^{124}Sn→^{188}Pt*	0	78	188	161.85-195.84	44.337-77.487	1400	0.674	1-0.543	[20]
^{132}Sn+^{64}Ni→^{196}Pt*	0	78	196	165.5-195.2	54.498-84.2	1400	0.646	1-0.696	[20]
^{19}F+^{194}Pt→^{213}Fr*	0	87	213	80.093-93.755	47.397-61.059	702	0.740	1	[27]
^{19}F+^{198}Pt→^{217}Fr*	0	87	217	79.184-105.355	47.479-69.650	702	0.727	1	[28]
^{11}B+^{204}Pb→^{215}Fr*	0	87	215	47.97-60.24	31.21-43.48	410	0.733	1	[29]
^{18}O+^{197}Au→^{215}Fr*	0	87	215	71.34-88.81	39.10-56.57	632	0.733	1	[29]
^{9}Li+^{208}Pb→^{217}At*	0	85	217	23.9-43.0	22.709-41.809	246	0.694	1-0.0011	[30]
SEDF(SIII/ GSkI)									
^{132}Sn+^{64}Ni→^{196}Pt*	0	78	196	165.5-195.2	56.2-84.2	1400	0.646	1-0.41	[22]
^{64}Ni+^{100}Mo→^{164}Yb*	0	70	164	122.9-158.8	30.6-66.5	1176	0.622	0.94-1	[21]

ented configurations are allowed in all above stated works on the DCM, except in ^{48}Ca + ^{154}Sm reaction where only spherical nuclei are considered.

Table 6.1 lists the characteristic properties of all the chosen reactions. The limiting values of the calculated P_{CN} are also given in this table. Since the dependence of P_{CN} on incident channel reaction characteristics is not yet investigated in detail, it is of interest to see its variation with center-of-mass energy $E_{c.m.}$, CN charge Z_{CN} (or mass A_{CN}) number, its excitation energy E^*, the fissility parameter χ (=$(Z^2/A)/48$), the reaction entrance channels in terms of quantities such as the

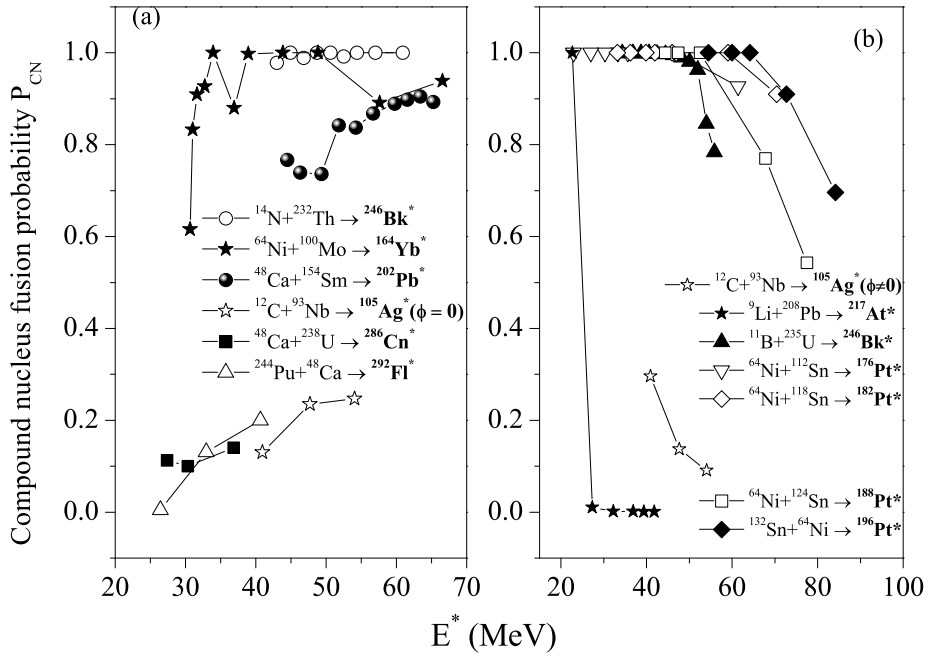

Figure 6.1: The DCM calculated P_{CN} as a function of compound nucleus excitation energy E^*, using Blocki *et al.* [45] pocket formula for nuclear proximity potential. The reactions are given in the body of figure.

Coulomb interaction parameter Z_1Z_2, etc. We present some of these results in the following for the DCM calculated P_{CN}.

Fig. 6.1 presents the variation of P_{CN} with CN excitation energy E^* for the chosen "hot fusion" reactions whose DCM calculations are based on pocket formula for the nuclear proximity potential of Blocki *et al.* [45]. The not-included ^{124}Ce* is studied at one E^* only. The same results for P_{CN} are presented in Fig. 6.2 as a function of center-of-mass energy $E_{c.m.}$. A few interesting results follow from these figures: (i) The compound systems form two groups, one consisting of reactions presented explicitly in Fig. 6.1(a), showing an increasing behavior of P_{CN} with increase of E^* (or $E_{c.m.}$), approaching unity at higher excitation energies (or c.m. energies) meaning thereby complete fusion at high E^* (or $E_{c.m.}$). (ii) The second group presented explicitly in Fig. 6.1(b), consisting of the reactions, which show a reverse behavior of P_{CN}=1 for lower excitation or c.m. energies, which decreases continuously as the excitation energy E^* (or c.m. energy $E_{c.m.}$) increases. This means that the content of CN decreases, or equivalently, the nCN content increases

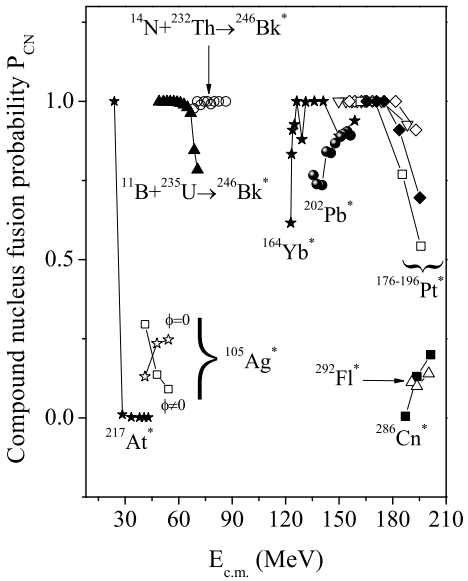

Figure 6.2: Same as for Fig. 6.1, but for its variation with center-of-mass energy $E_{c.m.}$.

with increase of E^* or $E_{c.m.}$. Interestingly, for ^{105}Ag* in going from Φ=0^0 to Φ not equal to 0^0, i.e., with the Φ degree of freedom included, the trend of variation of P_{CN} with E* for ^{105}Ag* becomes decreasing instead of increasing. Note that, in the Φ=0^0 case for P_{CN}, ^{105}Ag* belongs to a group of nuclei which includes strongly fissioning superheavy nuclei Z=112, ^{286}Cn* and Z=114, ^{292}Fl* all having P_{CN} <<1, but for $\Phi\neq0^0$ it belongs to the other group of weakly fissioning nuclei such as ^{164}Yb*, ^{202}Pb*, $^{176-196}$Pt*, and ^{13,217}Fr* which is actually the case, i.e., ^{105}Ag* is a weakly fissioning nucleus. P_{CN} for ^{217}At* (formed by projecting neutron-rich ^{9}Li on ^{208}Pb) is also found to be far less than unity at higher energies as it is found to decay mainly via nCN. Apparently, it will be interesting to extend the cases of P_{CN} <<1 to higher excitation or c.m. energies and those of P_{CN}=1 to both lower and higher excitation or c.m. energies.

Fig. 6.3 shows the role of using different nuclear interaction potentials on P_{CN}, and co-planar versus non-coplanar nuclei, where its variation with E^* is presented for Skyrme energy density formalism (SEDF) dependent potentials (using Skyrme forces SIII and GSkI) in comparison with pocket formula of Blocki *et al.* for both

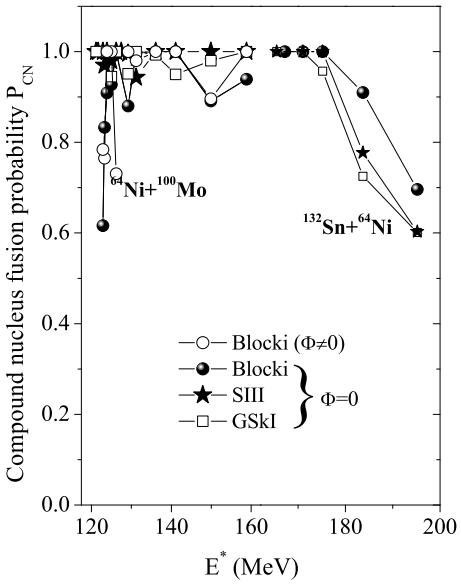

Figure 6.3: Variation of P_{CN} with E^*, showing comparison for use of different nuclear interaction potentials (pocket formula of Blocki *et al.* versus potentials based on SEDF using SIII and GSkI forces) for Φ=0, and for two ^{64}Ni-based compound systems ^{164}Yb* and ^{186}Pt*. The case of $\Phi \neq 0$ is also added for ^{164}Yb*.

Φ=0 and $\Phi \neq 0$ cases, and for two systems ^{164}Yb* and ^{196}Pt*, both using ^{64}Ni, one with a deformed ^{100}Mo and other with doubly-magic spherical ^{132}Sn nucleus. The interesting result is that, independent of azimuthal angle Φ, different nuclear potentials have almost no effect on P_{CN}, for both the spherical and deformed systems belonging to two different groups of one with $P_{CN} << 1$ and another with P_{CN}=1 at lower excitation energies (refer to Fig. 6.4). In other words, the compound nucleus fusion probability P_{CN} is nearly independent of co-planarity/ non-coplanarity of nuclei, and of different nuclear interaction potentials. The small miss-match in cases of ^{164}Yb* and ^{202}Pb* is possibly due to the difference in fittings of the data, which could happen because of large error-bars in these data at very low energies [16,17,21].

Fig. 6.4 shows the variation of P_{CN} with the fissility parameter χ (=$(Z^2/A)/48$) for CN ^{105}Ag* (both co-planar and non-co-planar configurations), ^{124}Ce*, ^{164}Yb*, $^{176-196}$Pt*, ^{202}Pb*, ^{213,215,217}Fr*, ^{217}At*, ^{246}Bk*, ^{286}Cn* and ^{292}Fl*, marked in the body of the figure, studied at various excitation energies E^*, forming two energy groups of ranges E^*=22-55 and 56-88 MeV. We have also added in this figure, the

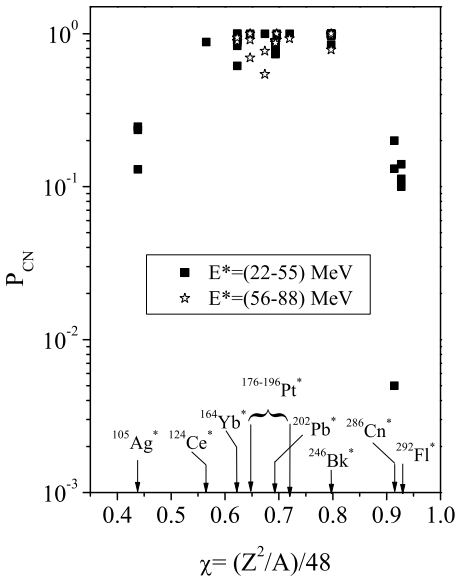

Figure 6.4: Variation of P_{CN} with the fissility parameter χ for all the reactions under consideration.

reaction ^{32}S+^{92}Mo$\rightarrow^{124}$Ce*, studied very recently [24] on the DCM at one excitation energy E^*=46.5 MeV only. We notice in Fig. 6.4 that for the high energy range (E^*=56-88 MeV; open star), P_{CN} $\approx$1 for all the systems with χ lying between 0.62 and 0.8. On the other hand, for the low energy range (E^*=22-55 MeV, filled squares), P_{CN} varies from $\sim$0.13 to almost zero (0.005), going through nearly unity, as χ increases from 0.45-0.9. Thus, for CN having χ=0.62-0.8, the P_{CN}=1 but for the superheavy systems, like ^{286}Cn and ^{292}Fl with higher χ (=0.914 and 0.927), the P_{CN} $<<$1, indicating the presence of large nCN effects. Similar to the cases of superheavy systems, P_{CN} $<<$1 for a very low-χ (almost half; =0.44) case of CN ^{105}Ag*. Interestingly, a similar behavior is observed by Yanez *et al.* [5], except for the case of low χ compound system where P_{CN} $<<$1.

Next, Fig. 6.5 shows the variation of P_{CN} with compound nucleus mass number A_{CN}. Interestingly, like for Fig. 6.1, the chosen reactions fall in two groups, one with P_{CN} $\rightarrow$1 as the excitation energy E^* increases (open circles) and another with P_{CN} $\rightarrow$1 as the excitation energy E^* decreases (filled circles). This is shown explicitly in Fig. 6.5(a) and 6.5(b), respectively. In other words, for one group

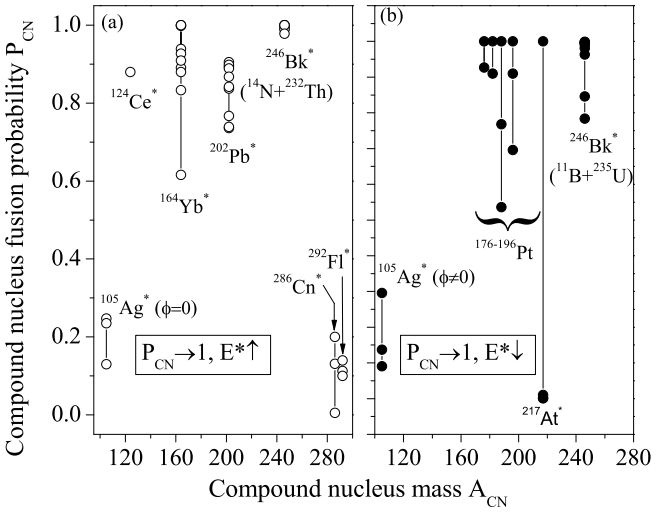

Figure 6.5: Variation of P_{CN} with compound nucleus mass number A_{CN}.

(Fig. 6.5(a)) P_{CN}=1 at the highest E^*, whereas for the second group (Fig. 6.5(b)), the same happens at the lowest E^*. The same result is obtained for P_{CN} as a function of compound nucleus charge Z_{CN}, except that in this case the isotopic or target+projectile dependence could not be studied.

Fig. 6.6 gives a better presentation of the above result where P_{CN} is plotted as a function of target-projectile charge numbers product Z_1Z_2, the Coulomb interaction parameter. We notice that $P_{CN} \rightarrow$1 for 400$< Z_1Z_2 <$1400, and that in the two limiting Z_1Z_2 values, P_{CN}=1 at the lowest E^*. Two groups are again evident, one of $P_{CN} \rightarrow$1 as E^* increases (open circles) and other of $P_{CN} \rightarrow$1 as E^* decreases (filled circles). Knowing that the fusion probability P_{CN} depends strongly on Coulomb repulsion, we notice in Fig. 6.6 that, as expected, P_{CN} decreases rapidly for $Z_1Z_2 >$1400 and, although completely unexpected, also for $Z_1Z_2 <$460, possibly due to large empirical nCN component in this case.

6.3 Summary

Concluding, the compound nucleus (CN) fusion/ formation probability P_{CN} is defined and detailed analysis carried out for the first time on the basis of the dynamical cluster-decay model (DCM) where the fusion cross section σ_{fusion} is calculated as

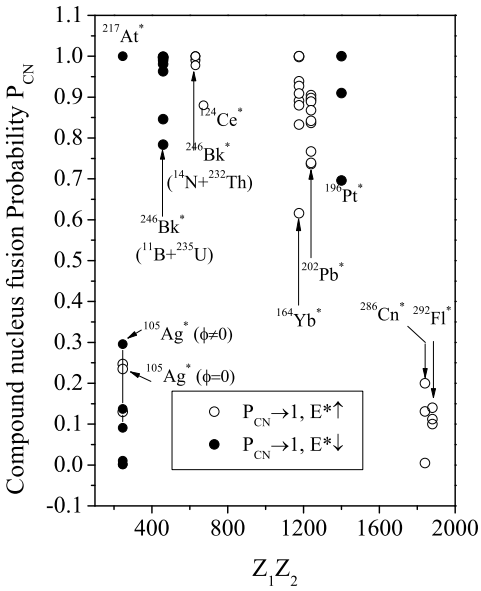

Figure 6.6: Variation of P_{CN} with target-projectile charge numbers product Z_1Z_2.

the dynamical fragmentation process. The fusion cross section σ_{fusion} is taken as the sum of CN formation cross section σ_{CN} and the possible non-compound nucleus (nCN) contribution σ_{nCN}, calculated for each contributing fragmentation (A_1, A_2) in terms of its formation and barrier penetration probabilities P_0 and P. The compound nucleus decay cross section σ_{CN} is the sum of cross sections due to the evaporation residues (ER) and fusion-fission (ff) processes, where ER is made up of light particles $A_2 \leq 4$ or neutrons (plus the complementary heavy fragments) and the ff are the near-symmetric and symmetric ($A_1 = A_2 = A/2$) fragments (nSF and SF), including the IMFs ($5 \leq A_2 \leq 20$, $2 < Z_2 < 10$). The non-compound nucleus decay cross section σ_{nCN}, on the other hand, is determined as the quasi-fission (qf) process where the incoming nuclei do not loose their identity, and hence P_0=1 with P calculated for incoming channel.

The DCM is applied to some "hot" fusion reactions at various incident energies, covering the mass region from A$\sim$100 to superheavy nuclei. The P_{CN} is calculated for various nuclear interaction potentials (Blocki *et al.* pocket formula and SEDF based potentials due to Skyrme SIII and GSkI forces), and its variation with CN excitation energy E^*, c.m. energy $E_{c.m.}$, fissility parameter χ, CN mass number

A_{CN} and target-projectile charge numbers product Z_1Z_2 are studied. The interesting result is that, independent of the nuclear interaction potential used, for some compound systems P_{CN}=1 at lower E^* (or $E_{c.m.}$) values but decreases (equivalently, nCN component increases) as E^* (or $E_{c.m.}$) increases, whereas for other compound systems the variation of P_{CN} with E^* (or $E_{c.m.}$) is reversed, i.e., P_{CN} <<1 at lower E^* (or $E_{c.m.}$) values but it increases as E^* (or $E_{c.m.}$) increases. Variation of P_{CN} with χ is also interesting in that it is almost unity for systems with χ=0.62-0.8, but is <<1 for systems with very high or very low χ values. The same two group behavior is also evident in its variation with CN mass number A_{CN} or product Z_1Z_2, with P_{CN}=1 at the lowest E^* for one group and at the highest E^* for another. The role of Coulomb interaction is also seen in decreasing P_{CN} strongly for Z_1Z_2 >1400 and Z_1Z_2 <460, but P_{CN} →1 for 400< Z_1Z_2 <1400, although the lower limit here needs further investigation.

This study is further extended by our group to the calculations of P_{surv} [7], and the reduced ERs via the product of P_{CN} and P_{surv} [62]. It will be interesting to extend these calculations to more and more reactions, and see if the above noted trends are kept the same or some new trends get added. Based on only a few "cold" fusion reactions, some authors [4] have even given a mathematical formulation of such trends, hoping for the universality of their results. On the DCM, further studies are needed for such formulations.

Bibliography

[1] A. Kaur, S. Chopra, and R. K. Gupta, Phys. Rev. C **90**, 024619 (2014).

[2] N. Bohr, Nature (London) **137**, 344 (1936).

[3] V. I. Zagrebaev, Y. Aritomo, M. G. Itkis, Yu. Ts. Oganessian, and M. Ohta, Phys. Rev. C **65**, 014607 (2001).

[4] V. I. Zagrebaev and W. Greiner, Phys. Rev. C **78**, 034610 (2008).

[5] R. Yanez, W. Loveland, J. S. Barrett, L. Yao, B. B. Back, S. Zhu, and T. L. Khoo, Phys. Rev. C **88**, 014606 (2013).

[6] A. Kaur, S. Chopra, and R. K. Gupta, Contribution 75-years of Nuclear Fission: Present status and Future Perspectives, May 8-10, 2014 at BARC, Mumbai.

[7] S. Chopra, A. Kaur, and R. K. Gupta, Phys. Rev. C **91**, 034613 (2015).

[8] S. Chopra, A. Kaur, and R. K. Gupta, Contribution FUSION14, IVth international conference, IUAC, New Delhi, February 24-28, 2014.

[9] R. K. Gupta, Lecture Notes in Physics 818 *Clusters in Nuclei*, ed C. Beck, Vol.I, (Springer Verlag, Berlin, Heidelberg 2010), p. 223; and earlier references there in it.

[10] R. K. Gupta, M. Balasubramaniam, C. Mazzocchi, M. La Commara, and W. Scheid, Phys. Rev. C **65**, 024601 (2002).

[11] R. K. Gupta, R. Kumar, N. K. Dhiman, M. Balasubramaniam, W. Scheid and C. Beck, Phys. Rev. C **68**, 014610 (2003).

[12] M. Balasubramaniam, R. Kumar, R. K. Gupta, C. Beck and W. Scheid, J. Phys. G: Nucl. Part. Phys. **29**, 2703 (2003).

[13] M. Bansal and R. K. Gupta, Romanian J. Phys. **57**, 18 (2012).

[14] B. B. Singh, M. K. Sharma, R. K. Gupta, and W. Greiner, Int. J. Mod. Phys. E **15**, 699 (2006).

[15] B. B. Singh, M. K. Sharma, and R. K. Gupta, Phys. Rev. C **77**, 054613 (2008).

[16] S. K. Arun, R. Kumar, and R. K. Gupta, J. Phys. G: Nucl. Part. Phys. **36**, 085105 (2009).

[17] S. Kanwar, M. K. Sharma, B. B. Singh, R. K. Gupta, and W. Greiner, Int. J. Mod. Phys. E **18**, 1453 (2009).

[18] R. K. Gupta, Niyti, M. Manhas, S. Hofmann, and W. Greiner, Int. J. Mod. Phys. E **18**, 601 (2009).

[19] Niyti, R. K. Gupta, and W. Griner, J. Phys. G: Nucl. Part. Phys. **37**, 115103 (2010).

[20] M. K. Sharma, S. Kanwar, G. Sawhney, R. K. Gupta, and W. Greiner, J. Phys. G: Nucl. Part. Phys. **38**, 055104 (2011).

[21] M. Bansal, S. Chopra, R. K. Gupta, R. Kumar, and M. K. Sharma, Phys. Rev. C **86**, 034604 (2012).

[22] D. Jain, R. Kumar, M. K. Sharma, and R. K. Gupta, Phys. Rev. C **85**, 024615 (2012).

[23] S. Chopra, M. Bansal, M. K. Sharma, and R. K. Gupta, Phys. Rev. C **88**, 014615 (2013).

[24] A. Kaur, S. Chopra, and R. K. Gupta, Phys. Rev. C **89**, 034602 (2014).

[25] Niyti and R. K. Gupta, Phys. Rev. C **89**, 014603 (2014).

[26] S. Chopra, Hemdeep, A. Kaur, and R. K. Gupta, Phys. Rev. C **93**, 024603 (2016).

[27] M. K. Sharma, Gudveen Sawhney, R. K. Gupta and W. Griener, J. Phys. G: Nucl. Phys. **38**, 105101 (2011).

[28] M. K. Sharma, S. Kanwar, G. Sawhney, and R. K. Gupta, Phys. Rev. C **85**, 064602 (2012).

[29] G. Sawhney, G. Kaur, M. K. Sharma, and R. K. Gupta, Phys. Rev. C **88**, 034603 (2013).

[30] Decay analysis of compound nucleus ^{217}At* formed via neutron-rich exotic ^{9}Li on ^{208}Pb and its synthesis within the dynamical cluster-decay model. A. Kaur, B. R. Behera, and R. K. Gupta, Chandigarh Preprint 2016.

[31] R. K. Gupta, M. Manhas, and W. Greiner, Phys. Rev. C **73**, 054307 (2006).

[32] R. K. Gupta, M. Balasubramaniam, R. Kumar, N. Singh, M. Manhas, and W. Greiner, J. Phys. G: Nucl. Part. Phys. **31**, 631 (2005).

[33] R. Kumar, M. Bansal, S. K. Arun, and R. K. Gupta, Phys. Rev. C **80**, 034618 (2009).

[34] J. Maruhn and W. Greiner, Phys. Rev. Lett. **32**, 548 (1974).

[35] R. K. Gupta, W. Scheid, and W. Greiner, Phys. Rev. Lett. **35**, 353 (1975).

[36] D. R. Saroha and R. K. Gupta, J. Phys. G: Nucl. Phys. **12**, 1265 (1986).

[37] S.S. Malik, N. Malhotra, D.R. Saroha, and R.K. Gupta, ICTP, Trieste, Italy, Report No. IC/86/120, 1986.

[38] H. Kröger and W. Scheid, J. Phys. G **6**, L85 (1980).

[39] D.R. Inglis, Phys. Rev. **96** (1954) 1059.

[40] S.T. Balyaev, K. Dan. Vidensk. Selsk. Mat.-Fys. Medd. **31** (1959) No. 11.

[41] W. Myers and W. J. Swiatecki, Nucl. Phys. **81**, 1 (1966).

[42] A. S. Jensen and J. Damgaard, Nucl. Phys. **A203**, 578 (1973).

[43] N. J. Davidson, S. S. Hsiao, J. Markram, H. G. Miller, and Y. Tzeng, Nucl. Phys. **A570**, 61c (1994).

[44] G. Audi, A.H. Wapstra, and C. Thiboult, Nucl. Phys. **A729**, 337 (2003).

[45] J. Blocki, J. Randrup, W. J. Swiatecki, and C.F. Tsang, Ann. Phys. (N.Y.) **105**, 427 (1977).

[46] M. Brack, C. Guet, and H. -B. Hakansson, Phys. Rep. **123**, 275 (1985).

[47] J. Friedrich and P.-G. Reinhardt, Phys. Rev. C **33**, 335 (1986).

[48] B. K. Agrawal, S. K. Dhiman, and R. Kumar, Phys. Rev. C **73**, 034319 (2006).

[49] K. Hagino, N. Rowley, and A.T. Kruppa, Computer Physics Communications **123**, 143 (1999).

[50] R. K. Gupta, in *Proceedings of the 5th International Conference n Nuclear Reaction Mechanisms*, Varenna, Italy, edited by Gadioli E (Ricerca Scintifica Educazione Permanente, Italy) (1988), p. 416.

[51] S. S. Malik and R. K. Gupta, Phys. Rev. C **39**, 1992 (1989).

[52] R. K. Gupta and W. Greiner, Int. J Mod. Phys. E **3**, 335 (1994, Supp.).

[53] W. Pauli, *Handbuck der Physik*, Vol. **24**, Part I, p.120, ed. H. Geiger and K. Sheel, (Springer, Berlin 1933); B. Padolsky, Phys. Rev. **32** (1928) 812; J. Eisenberg and W. Greiner, *Nuclear Models*, North Holland Pub., Amsterdam 1971, p.136.

[54] G. Royer and J. Mignen, J. Phys. G: Nucl. Part. Phys. **18**, 1781 (1992).

[55] H. S. Khosla, S. S. Malik and R. K. Gupta, Nucl. Phys. A **513**, 115 (1990).

[56] S. Kumar, and R. K. Gupta, Phys. Rev. **55**, 218 (1997).

[57] R. K. Gupta, S. Kumar and W. Scheid, Int. J Mod. Phys. E **6**, 259 (1997).

[58] T. Matsuse, C. Beck, R. Nouicer and D. Mahboub, Phys. Rev. C **55**, 1380 (1997).

[59] S. J. Sanders, Phys. Rev. C **44**, 2676 (1991).

[60] S. J. Sanders, D. G. Kovar, B. B. Back, C. Beck, D. J. Henderson, R. V. F. Janssens, T. F. Wang and B. D. Wilkins, Phys. Rev. C **40**, 2091 (1989).

[61] C. H. Dasso, S. Landowne, and A. Winther, Nucl. Phys. **A405**, 381 (1983).

[62] Sahila Chopra, Arshdeep Kaur, Hemdeep, and Raj K. Gupta, Phys. Rev. **93**, 044604 (2016).

Chapter 7

Summary

The Dynamical Cluster-decay Model (DCM) has been used successfully to address the formation and decay process of heavy ion collisions at low energy region. The DCM is based on well known Quantum Mechanical Fragmentation Theory (QMFT) and has been developed to study the effects of nuclear structure, deformation and orientation degrees of freedom of outgoing fragments/ nuclei in the decay of hot and rotating compound nuclei (CN). Within the DCM, fragments are preformed with certain preformation probabilityP_0 before penetrating the interaction barrier. P_0 contains the structure effects of CN providing the possibility of studying fine or sub-structure in fission products. Nuclear shapes, i.e., the deformations and the orientations of nuclei, during fusion reactions change the interaction barrier (i.e., height as well as position) thereby affecting the dynamics of reaction process The only parameter of DCM is the neck-length parameter ΔR representing the reaction time scale and also referring to the actual used barrier height which consequently introduces the concept of barrier lowering $\Delta\ V_B$, explaining the fusion hindrance/ enhancement phenomena.

An overview of relevant status of research and related aspects of nuclear physics are discussed in Chapter 1. A broad classification of heavy ion reactions and various approaches to handle the nuclear interactions are described, in addition to the outline

of thesis in this chapter. The details of the methodology used, i.e., the dynamical cluster-decay model and ℓ-summed Wong model are discussed in Chapter 2 with nuclear interaction potential obtained from various proximity potentials as well as from Skyrme energy density formalism. The methodology has been employed to address the fusion-fission dynamics governed via heavy ion collisions at low energy region. Different components of σ_{fusion}, i.e., CN decay processes and non-compound (nCN) decay processes are also explained. The concept of CN fusion/ formation probability P_{CN} and CN survival probability P_{surv} are also introduced for the first time within the DCM.

An application of the DCM is first made to a proton-rich CN ^{124}Ce* formed in ^{32}S+^{92}Mo reaction at two different incident energies of $E_{c.m.}$=111.29 MeV ($\equiv$150 MeV beam energy) and 103.87 MeV ($\equiv$140 MeV beam energy), though the data are available only at the first above barrier energy. In other words, experimentally, this system is studied at an incident center-of-mass energy $E_{c.m.}$=111.29 MeV (equivalently, the laboratory energy 150 MeV), and heavy mass decay products observed, whose complementary light decay products are the multiple proton clusters (2p, 3p, 4p) and intermediate mass fragments like ^{5}Li, ^{6}Be, ^{7}B, and ^{10}C, plus their isobars like ^{3,4}He, ^{5}Be, ^{6}Li, ^{7}Be, etc. The measured cross-sections are given relative to ^{4}Li decay, and we compare the measured relative cross-sections of ^{6}Be and ^{10}C with ^{8}Be and ^{12}C, respectively, though both ^{8}Be and ^{12}C decays are not observed in this experiment (even the upper limits are not given). For the best fitted neck-length parameters of two LPs (2p and 3p) and two IMFs (^{5}Li and ^{6}Be), the relative populations of ^{6}Be and ^{8}Be, and that of ^{10}C and ^{12}C are analyzed, showing thereby that the compound nucleus ^{124}Ce* decays preferentially via A=4n, α-nucleus clusters as compared to A$\neq$4n, non-α nucleus clusters, similar to what was predicted for ground-state (T=0) decays, and also earlier for decay of ^{116}Ba* formed in ^{58}Ni+^{58}Ni reaction at various $E_{c.m.}$. This confirms the excitation energy independence of α-nucleus structure effects in ^{124}Ce*, similar to what was shown earlier for a lighter

system ^{56}Ni* In the above barrier energy data, the possible non-compound nucleus effects are shown to be small and the CN formation probability calculated to be close to unity. However, the charge distribution due to observed isobars is not yet investigated. This study was made by using the pocket formula of Blocki *et al.* for the nuclear proximity potential.

The above study is then extended to the use of various other nuclear interaction potentials derived from the ETF-based semiclassical SEDF method. Both the old and new Skyrme forces are considered. It is interesting to find that the only parameter of the model, neck-length ΔR, remains within $\sim$2 fm, the range of validity of proximity potential used here. Again, for the best fitted ΔR of two LPs (2p and 3p) and two IMFs (^{5}Li and ^{6}Be), similar to what was obtained earlier for use of pocket formula of Blocki *et al.*, the relative populations of ^{6}Be *vs.* ^{8}Be, and that of ^{10}C *vs.* ^{12}C show that the CN ^{124}Ce* decays preferentially via A=4n, α-nucleus clusters, as compared to A$\neq$4n, non-α nucleus clusters, for *only* SIII and KDE0(v1) Skyrme forces. Considering the cross sections of orders similar to observed ones for ER and IMFs, the IMF-window is shown extended to A_2=16, and a new decay region of HMFs A_2=27-48 or 28-48 and a near-symmetric and symmetric fission fragments A_2=49-62 or 51-62 are predicted, which on combining with the complementary heavy fragments result in the ff region of $(A/2)\pm12$. Using the predicted (total) fusion cross-section, the CN survival probability P_{surv} comes out to be very small for all the considered nuclear interactions, due to large predicted fusion-fission contribution. However, the CN fusion probability P_{CN} is nearly unity for all nuclear interactions, due to very small empirically estimated non-compound nucleus content, establishing that ^{124}Ce* decay is nearly a pure CN decay. We have also applied the (ℓ-summed) extended-Wong model of Gupta and collaborators to this reaction, but the calculated total fusion cross sections could not be compared with the measured data since only relative cross sections are given in the experiment. However, the ℓ_{max} values and the order of predicted fusion cross sections for the two

models (DCM and extended-Wong model) are similar, and thus could be useful in planning further experiments in this mass region.

The next application of the DCM is to the study of the decay mechanism of CN ^{217}At* formed in a reaction induced by neutron-rich ^{9}Li on a doubly magic shell nucleus ^{208}Pb at various center-of-mass energies $E_{c.m.}$. The aim here is to investigate the role of neutron-rich light projectile on (total) fusion cross section σ_{fus}, knowing well that σ_{fus} is largest for a reaction with doubly magic reaction partner. In ^{9}Li+^{208}Pb reaction, for the LPs evaporation residues, only 3n-6n emissions are observed (i.e., 1n and 2n are not observed) whose sum of the cross sections $\sum_{x=1}^{6} \sigma_{xn} \equiv \sigma_{fus}$ (including the unobserved 1n and 2n cross sections), can be fitted very nicely within the DCM as a pure CN decay process for a fixed value of the only parameter of this model, the neck-length parameter ΔR. Similar calculations of ^{9}Li induced reactions on ^{70}Zn and various isotopes of other targets used in earlier experimental studies at intermediate energies, show a strong dependence of σ_{fus} on mass and shell structure of the target nucleus, supporting the above stated effect of closed magic shells. However, in this case of fixed ΔR, the unobserved decay channels (1n, 2n) are strongly over-estimated, and hence the observed ones (3n-6n) strongly under-estimated, with the ff cross section σ_{ff} also being very large compared to nearly zero, expected in experiments.

To improve upon the above result, we have fitted the individual decay channels (both unobserved and observed ones), together with the ff channel, with different ΔR values, i.e., different reaction times for different decay channels. Interestingly, now the fits for the pure CN decay cross section are very poor for LPs residue channels ($\sigma_{CN} < 1\%$ of total $\sigma_{fus}^{Expt.}$) with σ_{ff} reduced nearly to zero. This calls for the empirical nCN contribution, which is treated as the quasi-fission-like process (channel preformation probability P_0=1). Excellent fits are once again obtained for $\Delta R_{nCN} < \Delta R_{CN}$, with σ_{nCN} constituting most (99%) of the σ_{fus} at all the incident energies. In terms of CN formation and CN survival probabilities, the above result

means P_{CN} <<1 and P_{surv} ≈1. Thus, our DCM analysis shows that the neutron-rich ^{9}Li induced reaction is more of a quasi-fission-like non-compound nucleus decay.

Furthermore, the synthesis of ^{217}At* via various "cold" (t,p) combinations, refereeing to potential energy minima, for "hot" compact configurations, is carried out and ^{8}Li+^{209}Pb as the optimum combination with lowest interaction barrier and smallest (most compact) interaction radius identified. In view of the role of double magic shell, however, ^{48}Ca+^{169}Tb would result in the largest fusion cross section.

Within the DCM, various "hot" fusion reactions have been studied till to-date. For analyzing this data in terms of the CN fusion/ formation probability P_{CN}, we have picked up some of these "hot" fusion reaction calculations and carried out the detailed analysis for the very first time using the DCM. In DCM, the fusion cross section σ_{fusion} is calculated as the dynamical fragmentation process. The fusion cross section σ_{fusion} is taken as the sum of CN formation cross section σ_{CN} and the possible non-compound nucleus (nCN) contribution σ_{nCN}, calculated for each contributing fragmentation (A_1, A_2) in terms of its formation and barrier penetration probabilities P_0 and P. The compound nucleus decay cross section σ_{CN} is the sum of cross sections due to the evaporation residues (ER) and fusion-fission (ff) processes, where ER is made up of light particles A_2 ≤4 or neutrons (plus the complementary heavy fragments) and the ff are the near-symmetric and symmetric ($A_1 = A_2 = A/2$) fragments (nSF and SF), including the IMFs (5≤ A_2 ≤20, 2< Z_2 <10). The non-compound nucleus decay cross section σ_{nCN}, on the other hand, is determined as the quasi-fission (qf) process where the incoming nuclei do not loose their identity, and hence P_0=1 with P calculated for the considered exit channel.

The DCM is applied to various fusion reactions at different incident energies, covering the mass region from A∼100 to superheavy nuclei. The P_{CN} is calculated for various nuclear interaction potentials (Blocki *et al.* pocket formula and SEDF based potentials due to Skyrme SIII and GSkI forces), and its variation with CN excitation energy E^{*}, c.m. energy $E_{c.m.}$, fissility parameter χ, CN mass number

A_{CN} and target-projectile charge numbers product Z_1Z_2 are studied. The interesting result is that, independent of the nuclear interaction potential used, for some compound systems P_{CN}=1 at lower E^* (or $E_{c.m.}$) values but decreases (equivalently, nCN component increases) as E^* (or $E_{c.m.}$) increases, whereas for other compound systems the variation of P_{CN} with E^* (or $E_{c.m.}$) is reversed, i.e., P_{CN} <<1 at lower E^* (or $E_{c.m.}$) values but it increases as E^* (or $E_{c.m.}$) increases. Variation of P_{CN} with χ is also interesting in that it is almost unity for systems with χ=0.62-0.8, but is <<1 for systems with very high or very low χ values. The same two group behavior is also evident in its variation with CN mass number A_{CN} or product Z_1Z_2, with P_{CN}=1 at the lowest E^* for one group and at the highest E^* for another. The role of Coulomb interaction is also seen in decreasing P_{CN} strongly for Z_1Z_2 >1400 and Z_1Z_2 <460, but P_{CN} →1 for 400< Z_1Z_2 <1400, although the lower limit here needs further investigation. This study is also extended further by our group to the study of CN survival against fission, i.e., CN survival probability P_{surv}.

The present work has the potential of extending it to other mass regions, for obtaining a good understanding of nuclear structure in general and nuclear reaction dynamics in particular. It may be noticed that all the calculations done in the present work, except the ones included in the analysis of P_{CN}, are for two nuclei taken in the same plane (co-planar nuclei, with azimuthal angle $\Phi=0^0$), with deformation effects, and orientations included. It would certainly be interesting to further extend this study to non-coplanar ($\Phi\neq0^0$) configurations.